Probing the nuclear structure of fermium by laser spectroscopy

Dissertation

zur Erlangung des Grades
"Doktor der Naturwissenschaften"
im Promotionsfach Chemie

am Fachbereich Chemie, Pharmazie, Geographie und Geowissenschaften der Johannes Gutenberg-Universität Mainz

Jessica Warbinek

geboren in Hachenburg

Mainz, 23.10.2023

Dekanin:	Personal data
1. Berichterstatter:	Personal data
2. Berichterstatter:	Personal data
Tag der mündlichen Prüfung:	Donnerstag, 30.11.2023

Declaration

I hereby declare that I have independently authored this dissertation. I have utilized no resources other than those mentioned (literature, equipment, other supplies and help) and I have indicated citations from other published or unpublished works. This dissertation was never submitted in its entity or in part for any other academic or state examination, in particular not as a dissertation to another university, faculty or department. I have not previously pursued or obtained a doctoral degree, successfully or unsuccessfully.

Darmstadt, 23.10.2023

Jessica Warbinek

Jessica Warbinek
GSI Helmholtzzentrum für Schwerionenforschung GmbH
Planckstraße 1
D-64291 Darmstadt
j.warbinek@gsi.de
jwarbine@students.uni-mainz.de

Into the unknown

Abstract

The nuclear structure of heavy nuclei with proton numbers $Z > 100$ has been subject to various experimental and theoretical studies aimed at uncovering their fundamental properties. The mere existence of such heavy elements is based on the nuclear stabilization induced by shell effects, which counteract spontaneous fission due to the strong Coulomb repulsion, and determine the limits of nuclear existence. Moreover, shell effects can influence various nuclear properties, including the shape and size of heavy nuclei. Laser spectroscopy serves as a powerful tool to unveil such phenomena. By probing the atomic structure and the hyperfine sub-structure, various nuclear ground-state properties can be accessed, as the nuclear mean-square charge radius, spin and nuclear moments.

The available insight on nuclear ground-state properties around the $N = 152$ shell gap, in the region of the deformed heavy actinides, remains scarce. However, the limited information on the atomic level structures, which are strongly impacted by relativistic effects, and the low production yields and short half-lives hamper experimental studies with common laser spectroscopy methods. In addition, model predictions of atomic and nuclear properties to guide experimental studies are challenged by the complex many-body problem and the dense level scheme structures.

The RADRIS method, tailored to laser spectroscopy investigations of the heaviest actinide elements, was employed to access the element fermium ($Z = 100$) for the studies presented in this work. With recent developments of indirect production schemes, exotic fermium isotopes were accessed via the decay of directly produced nobelium mother isotopes from fusion-evaporation reactions. The technical advancements made within this work towards the study of longer-lived and shorter-lived isotopes, in combination with an enhancement in the overall efficiency, widened the scope of RADRIS to more previously inaccessible fermium isotopes. With these new developments, on-line laser spectroscopy studies in fermium were performed down to minute production rates for some isotopes. In addition, studies of longer-lived isotopes in up to pg-sample sizes from reactor-breeding were performed via highly sensitive hot-cavity laser spectroscopy at the RISIKO separator.

In summary, a chain of eight isotopes ranging from accelerator-produced ^{245}Fm to the reactor-bred ^{257}Fm was investigated by utilizing various production schemes and applying different on-line and off-line advanced laser spectroscopy techniques. Isotope shifts of an atomic transition were measured to extract changes in the nuclear mean-square charge radius across the $N = 152$ shell gap. The data was compared to predictions of

various nuclear models relying on energy density functionals. A good agreement was found between the smooth trend in the experimental results and the calculations, and between the models themselves. This implies that bulk properties have a prevailing influence, while the impact of shell effects on the nuclear charge radius observable appears to diminish. The findings made in this work will help to refine nuclear models, allowing for more accurate predictions within the range of the heavy and eventually super heavy elements. The achieved methodological improvements opened new avenues for experimental studies of more exotic isotopes in the region of the heaviest actinide elements. This, in turn, may provide initial insights into the atomic structure, particularly where information about atomic levels is currently unavailable, thus allowing for further nuclear structure investigations to enhance our understanding of these exotic nuclei.

Zusammenfassung

Die Struktur schwerer Kerne mit Protonenzahlen $Z > 100$ war und ist Gegenstand verschiedener experimenteller und theoretischer Untersuchungen, um fundamentale Eigenschaften dieser Kerne aufzudecken. Die bloße Existenz der schweren Elemente beruht auf der Stabilisierung durch Schaleneffekte, die der Spontanspaltung aufgrund der starken Coulomb-Abstoßung entgegen wirken, und sie bestimmen die Grenzen der Existentz solcher Kerne. Darüber hinaus können andere Kerneigenschaften wie die Form und Größe schwerer Kerne von Schaleneffekten beeinflusst werden. Laserspektroskopie gilt als ein effektives Werkzeug, um solche Phänomene aufzudecken. Durch die Untersuchung der Atomstruktur und der Hyperfeinstruktur können verschiedene nukleare Grundzustandseigenschaften wie der mittlere quadratische Kernladungsradius, der Spin und die Kernmomente zugänglich gemacht werden.

Die verfügbaren Kenntnisse zu den nuklearen Grundzustandseigenschaften rund um die $N = 152$ Schalenlücke, im Bereich der deformierten, schweren Aktinide, sind derzeit begrenzt. Allerdings stellen die wenigen vorhandenen Informationen über die atomaren Niveaustrukturen, die stark von relativistischen Effekten beeinflusst werden, sowie die geringen Produktionsausbeuten und kurzen Halbwertszeiten Hindernisse für herkömmliche Laserspektroskopie-Experimente dar. Darüber hinaus werden Modellvorhersagen zu atomaren und nuklearen Eigenschaften, die helfen können experimentelle Studien zu leiten, durch das komplexe Vielteilchenproblem und die dichten Niveauschemastrukturen herausgefordert.

Die RADRIS-Methode, entiwckelt für Laserspektroskopie-Untersuchungen der schwersten Aktinide, wurde verwendet, um das Element Fermium ($Z = 100$) für die in dieser Arbeit vorgestellten Experimente zu untersuchen. Durch die kürzlichen Entwicklungen von indirekten Produktionsverfahren wurden exotische Fermium-Isotope durch den Zerfall direkt produzierter Nobelium-Mutterisotope aus Fusions-Verdampfungsreaktionen zugänglich. Die zusätzlichen technischen Fortschritte, die in dieser Arbeit erzielt wurden, erweiterten den Anwendungsbereich von RADRIS auf noch weitere, zuvor unzugängliche Fermium-Isotope. Diese Fortschritte ermöglichten die Durchführung von Online-Laserspektroskopie-Studien in Fermium, trotz sehr geringer Produktionsraten für einige Isotope. Darüber hinaus wurden Untersuchungen an langlebigen Isotopen mit Proben im Pikogramm-Bereich, erzeugt durch Reaktor-Brüten, mithilfe hochsensitiver Offline-Laserspektroskopie am RISIKO-Massenseparator durchgeführt.

Zusammenfassend wurde in dieser Arbeit eine Kette von acht Isotopen untersucht, von beschleunigerproduziertem ^{245}Fm, bis hin zu reaktorgebrütetem ^{257}Fm. Hierzu

wurden verschiedene Herstellungsmethoden und unterschiedliche Online- und Offline-Laserspektroskopie-Techniken verwendet. Die Isotopieverschiebung eines atomaren Übergangs wurde gemessen, und daraus die Entwicklung des mittleren quadratischen Kernladungsradius über die $N = 152$ Schalenlücke hinweg extrahiert. Die Daten wurden mit Vorhersagen verschiedener Kernmodelle, basierend auf Energiedichtefunktionalen, verglichen. Es wurde eine gute Übereinstimmung zwischen dem gleichmäßigen Trend in den experimentellen Daten und den theoretischen Berechnungen, sowie zwischen den Modellen untereinander, festgestellt. Dies legt nahe, dass Einflüsse von Bulk-Eigenschaften dominieren, während der Einfluss von Schaleneffekten auf den Kernladungsradius gering erscheint.

Die in dieser Arbeit gewonnenen Erkenntnisse werden dazu beitragen moderne Kernmodelle zu verfeinern, um genauere Vorhersagen im Bereich der schweren und schließlich superschweren Elemente zu ermöglichen. Die erzielten methodischen Verbesserungen haben neue Möglichkeiten für experimentelle Studien von exotischeren Isotopen, besonders im Bereich der schwersten Aktinide, eröffnet. Dadurch können weitere Einblicke in die Atomstruktur gewonnen werden, insbesondere dort, wo Informationen über Atomniveaus derzeit nicht verfügbar sind, und somit weitere Untersuchungen der Kernstruktur anregen, um unser Verständnis dieser exotischen Kerne zu vertiefen.

Contents

Acronyms

AI Autoionizing

CI Configuration Interaction

CLS Collinear Laser Spectroscopy

CSF Configuration State Functions

cw Continuous Wave

DAQ Data Acquisition

DFT Density Functional Theory

DM Droplet Model

EDF Energy Density Functional

EFT Effective Field Theory

FES First Excitation Step

FPGA Field-Programmable Gate Array

FRDM Finite Range Droplet Model

FWHM Full Width at Half Maximum

GSI GSI Helmholtzzentrum für Schwerionenforschung GmbH

HF Hartree-Fock

HFB Hartree-Fock-Bogoliubov

HFIR High Flux Isotope Reactor

IGRIS Ion Guide-detected Resonance Ionization Spectroscopy

ILL Institute Laue-Langevin

IP Ionization Potential

LDM Liquid Drop Model

MBPT Many-Body Perturbation Theory

MCDHF Multiconfiguration Dirac-Hartree-Fock

MREDF Multi-Reference Energy Density Functional

MRTOF-MS Multi-Reflection Time-Of-Flight Mass Spectrograph

NMS Normal Mass Shift

OES Odd-Even Staggering

ORNL Oak Ridge National Laboratory

PI-LIST Perpendicularly Illuminated Laser Ion Source and Trap

PIPS Passivated Implanted Planar Silicon

QCD Quantum Chromodynamics

QED Quantum Electrodynamics

RADRIS Radiation Detected Resonance Ionization Spectroscopy

RIB Radioactive Ion Beam

RILIS Resonant Ionization Laser Ion Source

RIS Resonance Ionization Spectroscopy

RISIKO Resonanz-Ionisations Spektroskopie In Kolinearer Geometrie

SATLAS Statistical Analysis Toolbox for Laser Spectroscopy

SCMF Self-Consistent Mean-Field

SES Second Excitation Step

SHE Super Heavy Elements

SHG Second Harmonic Generation

SHIP Separator for Heavy Ion reaction Products

SMS Specific Mass Shift

Ti:Sa Titanium:Saphhire

UNILAC Universal Linear Accelerator

UV Ultraviolet

List of Figures

List of Tables

1. Introduction

Questions regarding both, the origin of matter in our universe and its composition have driven countless curious minds and scientists, not only in the most recent chapters of history. The pursuit for answers to these questions has spanned over many centuries. Yet, this endeavor became more and more intense in the 20th century after major breakthroughs in findings on the atomic substructure established foundations for more discoveries. With the identification of the positively charged nucleus in the core of the atom, comprising almost its full mass in a negligibly small part of its volume, the modern field of nuclear physics was born. It was only decades later, that the first insights into the nuclear substructure could be revealed by determining the two types of particles that constitute the atomic nucleus: the positively charged proton and the uncharged neutron.

Early on it was discovered that, while the number of protons in the nucleus uniquely determines the chemical element, the differing number of neutrons leads to nuclear variations for the same chemical element, so-called isotopes. The change in composition and in the respective number of the two nuclear constituents results in thousands of different nuclear formations spanning the nuclear landscape up to the limits of our current knowledge. More than 3000 different isotopes of the known chemical elements were discovered, with the majority of them being unstable against radioactive decay. Only about 250 nuclides are considered stable and abundant in the Earth's crust.

First theoretical models were developed to describe properties such as the binding energy of a nucleus, to predict its stability against spontaneous fission and radioactive decay, as well as the fusion of lighter nuclei. The macroscopic approach of the liquid drop model described the nucleus as an incompressible fluid of nucleons, taking into account different effects that enhance or decrease the binding of these constituents [1]. The Coulomb interaction, resulting in the repulsion of the protons, is predicted to dominate over the attractive nuclear force of the mean field for heavy elements with proton numbers $Z \gtrsim 104$. As a consequence, these elements should not exist regarding expectations from the liquid drop model. However, the periodic table has been continuously expanded, leading to the discovery of new elements up to the heaviest known to date, oganesson, with $Z = 118$ protons [2]. These so-called Super Heavy Elements (SHE) have been demonstrated to form through the synthesis at accelerator facilities. However, some of these heavy and superheavy nuclei are very short-lived and may exist for only a fraction of a second. An analysis of the structure of the heaviest nuclei is thus necessary to provide an explanation for their mere existence.

The development of the nuclear shell model has played a major role in shaping our current understanding of nuclear structure [3]. This model provides a quantum mechanical description of the nucleus and its single-particle structure, in which the nucleons occupy discrete orbitals, similarly to the electrons in the atom. Akin the chemical inertness of the noble gases with filled electron shells, increased stability can be derived for nuclei when their nuclear shells for the protons or nucleons are filled. The fully occupied orbitals exhibit significant energy gaps to the next free orbital, resulting in an increased stability. The nuclear shell model model explained the extraordinary stability and enhanced natural abundance of nuclei composed of a "magic" number of protons with $Z = 2, 8, 20, 28, 50, 82$, and/or of neutrons with $N = 2, 8, 20, 28, 50, 82, 126$. To date, ^{208}Pb is the heaviest known doubly-magic nucleus, composed of 82 protons and 126 neutrons. Theoretical models predicted the next heavier magic numbers at either $Z = 114, 120$, or 126 and $N = 172$ or 184 [4]. In this region of the nuclear landscape, nuclei are expected to exhibit relatively long half-lives with early predictions ranging from minutes to millions of years against spontaneous fission [5], which gives rise to the concept of the so-called island of stability. However, such heavy nuclei are presently out of reach for in-depth experimental studies to pin down the next magic numbers.

Nuclei with known magic numbers of protons and neutrons exhibit the distinct feature of a spherical shape. While these magic nuclei are spherical, it is well-established that the vast majority of the known nuclides are axially deformed, adopting either prolate ("cigar") or oblate ("football") shapes, but also more complex as for instance triaxial shapes can occur. The Nilsson-model [6] introduced the dependence of the nuclear orbitals on the deformation of the nucleus. With the change in orbital energies for deformed nuclei, additional smaller, yet considerable sub-shell gaps occur. Such gaps were identified for instance for neutron numbers of $N = 40$ [7, 8, 9], $N = 98$ [10, 11], for protons around $Z = 60$ [12]. They are pronounced in the actinide elements around $N = 152$ or $N = 162$ in combination with $Z = 100$ and $Z = 110$, respectively [13, 14]. In particular, the shell gap at $N = 152$ was content of various studies in the recent years [15, 13].

A first experimental evidence for a shell gap at $N = 152$ was found in systematics of the alpha-decay energies Q_α of californium (Cf, $Z = 98$) isotopes in 1954 by Ghiorso et al. [16]. Deviations from the smooth trend predicted by the heuristic liquid droplet model were observed, similar to the discontinuities in the Q_α-values previously also found in the polonium isotopic chain around $N = 126$. These discontinuities were in the order of a few percent relative to the effects at the nearby main shell closure at $N = 126$ and $Z = 82$. Recent precision mass measurements in nobelium and lawrencium isotopes at the GSI Helmholtzzentrum für Schwerionenforschung GmbH (GSI) finally confirmed the location and size of the shell gap at $N = 152$ [13]. Further nuclear structure studies revealed a minimum in $E(2^+)$-excitation energies for ^{252}Fm, which is indicative of the shell gap and confirms a maximum quadrupole deformation for this nucleus [15]. While information on the nuclear deformation can be established from in-beam spectroscopy experiments, the results are inherently dependent on nuclear models. Furthermore, the effect of the shell gap on nuclear ground-state properties such as nuclear moments

or the charge radius remains mostly unexplored, as experiments are hindered by low production rates and short half-lives.

Laser spectroscopy is a decisive tool, as it gives access to nuclear ground state and isomeric state properties. For instance, the nuclear size evolution and the influence of nuclear structure effects on this observable can be probed by measurements of isotope shifts in atomic transitions [17, 18]. In this way, changes in the mean-square charge radius can be inferred as successfully demonstrated for chains of exotic and short-lived isotopes ranging from the lightest elements up to the actinide elements [19, 20]. At known spherical shell gaps, a characteristic kink is observed, which reflects the effect of the shell closure [21, 22, 23, 24]. Additional observations on hyperfine splittings in atomic transitions of isotopes with non-zero spin can reveal information on the nuclear moments and allows assigning the nuclear spin [25, 26]. From the electric quadrupole moment, a deeper insight into the deformation can be gained, while the magnetic dipole moment yields information on the single-particle properties and collective motion.

Although laser spectroscopy has proven to be an effective method for unveiling nuclear structure characteristics, the access to the heaviest actinides is limited. Scarce information on the atomic level structures (if available at all) and low yields along with short half-lives of these nuclides challenge experimental investigations using this technique. Until recently, a crossing of the $N = 152$ shell gap and inferring its effect on the nuclear size evolution and the nuclear moments remained an untouched endeavor [20]. With the development of new laser spectroscopy techniques specifically tailored for such studies, first atomic levels were experimentally identified in the heavy actinide element nobelium ($Z = 102$). This allowed the extraction of mean-square charge radii in $^{252-254}$No and nuclear moments in ^{253}No [27, 28]. To evaluate the former in the region of the heaviest actinides, due to missing experimental atomic structure information, experimentalists still rely on additional input from atomic theory. To date, such missing information did not allow to asses the nuclear size evolution for instance from isotope shift measurements in californium crossing $N = 152$ [29].

In this work, laser spectroscopy studies of fermium isotopes are reported, spanning from the neutron-deficient ^{245}Fm to the neutron-rich ^{257}Fm across the $N = 152$ shell gap. With recent efforts from atomic theory, changes in the mean-square charge radius could be extracted from isotope shift measurements. With this new information on both sides of the shell gap, its influence on the nuclear size evolution was investigated. The experimental data was compared to state-of-the-art global nuclear models employing energy density functionals, and a good agreement between the models themselves and the experimental data was found. This suggests a reduced impact of shell effects acting on this observable, contrary to the effects observed at spherical shell gaps in lighter nuclei. These findings benchmark nuclear models and will trigger further developments to improve the model accuracies, eventually leading to better predictions of the stability of the heaviest nuclei.

This thesis is organized as follow: a brief introduction in nuclear models and nuclear ground-state properties is given in Chapter 2, along with an introduction into techniques to unravel nuclear properties from atomic structure information. An overview on available nuclear and atomic structure information in fermium is given in Chapter 3. Basic experimental methods employed for experimental studies of the heaviest actinide elements are explained in Chapter 4. In Chapter 5, a detailed description of recent developments on the Radiation Detected Resonance Ionization Spectroscopy (RADRIS) method applied for studies on fermium are presented. The following Chapter 6 summarizes the experimental information on the measurement campaigns, the subsequent data processing, and the data analysis. The results are presented in Chapter 7. The comparison to nuclear models allowed for an interpretation of the data in Chapter 8. Finally, the results of this work are concluded and future perspectives are presented in Chapter 9.

2. Introduction to concepts of nuclear and atomic physics

The description of the atomic and nuclear structure of chemical elements yields challenges for theoretical models. In particular, predictions regarding heavy elements, as for instance the actinide elements, being complex many-body systems, become increasingly difficult. Here, experimental results can help to refine these models and improve their predictive power. A better understanding of the structural characteristics can facilitate the development of more comprehensive models to describe the heaviest elements known and those beyond, which currently remain out of reach for experimental studies. The following sections discuss concepts of nuclear physics descriptions to solve the nuclear many-body problem and of atomic structure properties revealing nuclear structure information.

2.1. Nuclear structure

2.1.1. Liquid drop model

An initial attempt to describe the atomic nucleus was done in the form of the Liquid Drop Model (LDM) developed by Gamow in 1929 [30]. In this heuristic model, the atomic nucleus consists of α-particles forming a droplet of an incompressible fluid held together by surface tension. Soon after in 1935, von Weizsäcker derived the empirical mass formula to describe the binding energy within the LDM for a nucleus consisting of Z positively charged protons and N neutral particles, the neutrons [1]. The number of nucleons A, the mass number, is the sum of both. The nuclear radius in the spherical LDM can be described by a sphere with radius

$$R = R_0 \cdot A^{1/3}, \tag{2.1}$$

where $R_0 \approx 1.2\,\mathrm{fm}$ is the nuclear radius constant. Although the overall trend in charge radii can be deduced from the LDM, it fails to predict the evolution of nuclear size in isotopic chains especially towards more neutron rich nuclei [31].

With this early model, "bulk" properties such as nuclear masses and binding energies could be inferred from the number of contained nucleons and the overall predictions fit to experimental trends of determined masses. However, it lacks the description of quantum shell stabilization effects and certain nuclear configurations with an increased

stability close to so-called magic numbers. Here, the nuclear-shell model gave rise to an understanding of the increased natural abundance of isotopes with specific numbers of protons and neutrons.

2.1.2. Nuclear shell model

A quantum mechanical description of the nucleus followed in 1949 through the work of Goeppert-Mayer and Jensen on the nuclear shell-model [3, 32], for which they later were awarded the Nobel prize in physics. The shell model finally gave an answer to the extraordinary stability of nuclei with proton numbers at $Z = 2, 8, 20, 28, 50, 82$ and neutron numbers with $N = 2, 8, 20, 28, 50, 82, 126$. In this context, the nuclear stability at magic numbers corresponding to filled nuclear shells in this model, is similar to filled electron shells in the atom and the resulting low reactivity of the noble gases.

In the shell model, every nucleon moves in a potential created by all the other nucleons [33]. A first attempt to describe the nuclear potential included the infinite well and the harmonic oscillator potentials for which the Schrödinger equations in three dimensions can be solved analytically. Separate potentials are considered for the protons and neutrons, respectively, and the solutions are discrete but degenerate energy levels which the nucleons can occupy.

A more realistic potential to describe the nucleus, which is commonly used, is the Woods-Saxon potential [34]. It can be written as

$$V(r) = \frac{-V_0}{1 + e^{(r-R)/a}}, \tag{2.2}$$

where R describes the mean radius for which $V/V_0 = 0.5$, and V_0 is the potential well depth, usually in the order of 50 MeV. The parameter a describes the skin thickness, indicating the outer part of the nucleus over which the potential varies from $0.9 \cdot V_0$ to $0.1 \cdot V_0$ [33]. In this description, the definition of the nuclear radius is somewhat more complex than the simple assumption made by the LDM with a sharp sphere of radius R. In this case, while the density of nucleons remains constant, the charge density is higher near the center and decreases towards the outer part of the nucleus. A more common definition of the nuclear radius can be made using the (root-)mean-square radius, the effective radius, which will be further introduced in Sec. 2.1.5.

The degenerate neutron energy eigenstates resulting from the Woods-Saxon potential are shown in Fig. 2.2 on the left. By including spin-orbit coupling, the degenerate levels experience a splitting into sub-levels as shown on the right in the figure. The resulting levels are described via the principal quantum number $n = 1, 2, 3, ...$, the orbital angular momentum quantum number $l = 0, 1, 2, 3, ...$ or s, p, d, f,..[1], and the total angular momentum $j = l + s$ with the nucleon spin $s = \pm 1/2$. These main energy

[1] Historically, the orbital momentum quantum number is denoted with quantum numbers l =s, p, d, f,... as in the description of atomic orbitals.

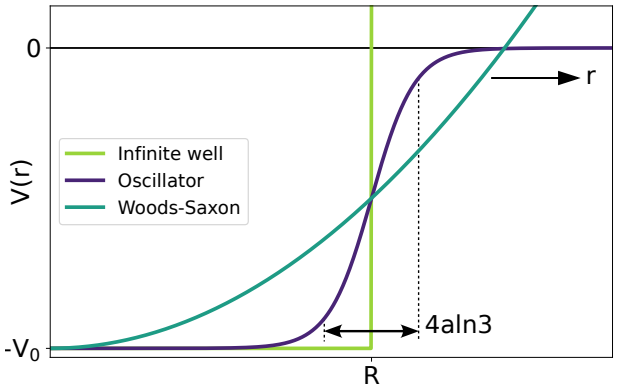

Figure 2.1.: Different potential forms used for the description with the nuclear shell model [35]. A more realistic is given with the Woods-Saxon potential, which includes the parameter a of the skin thickness.

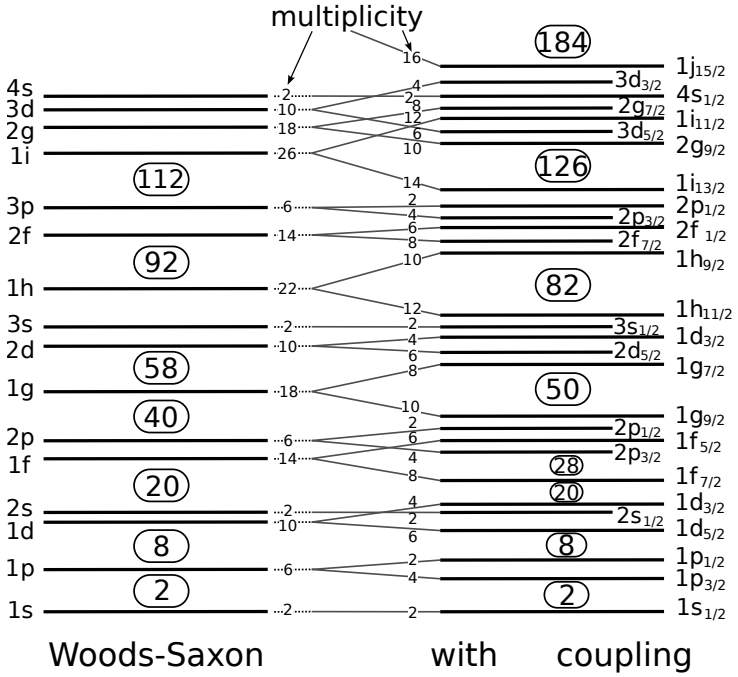

Figure 2.2.: Energy eigenvalues for neutrons predicted with the nuclear shell model. The levels on the left emerge in calculations with a simple Woods-Saxon potential, the levels on the right include the effect of spin-orbit coupling. The terms and multiplicity of the respective energy levels are given. The resulting magic numbers between large shell gaps differ for both cases, they are labeled in both schemes. Figure adapted from [33].

levels feature a degeneracy of $2j + 1$. With these quantum numbers and the magnetic quantum number m_j ranging from $-j$ to $+j$, each energy level can be assigned with its term following nl_j [36]. As both, protons and neutrons with an intrinsic spin of $1/2$ are fermions, they obey the Pauli exclusion principle. Therefore, they cannot feature

the same quantum numbers but be in either a spin up or down configuration. Due to the stabilizing effect of pairing, as already considered early on in the LDM [1], nuclear shells are consecutively filled, leaving a maximum of one unpaired proton and neutron in the nucleus.

The resulting levels differ for neutrons and protons due to the altered potential from the Coulomb repulsion for the latter. Nonetheless, the magic numbers itself remain the same, following currently available experimental insight, until 82. While for the smaller magic numbers up to 20 the principal shells are fully filled, the strong spin-orbit coupling leads to large energy gaps from the last occupied level to the next one of the same principal quantum number, as from the magic number 28 on [37].

The shell model can predict basic nuclear ground-state properties such as the spin of the nucleus and its parity, which is mostly determined by the outermost valence nucleon, and even isomeric states can be described. The assumption of a spherically symmetric potential in this model holds for closed and thus filled shells at magic numbers, however, nuclei outside of closed shells mostly feature an axially-symmetric deformed shape [35]. With the current knowledge on the trend of quadrupolar, meaning axial, deformation (see Sec. 2.1.5) over the nuclear landscape, most nuclei are deformed, and only the minority is spherical. Therefore, an extension of the shell model is often considered instead to improve the description of deformed nuclei.

2.1.3. Nilsson model

The Nilsson model considers the variation of nuclear energy orbitals in dependence of the quadrupole deformation [6]. Based on an axially-symmetric oscillator potential in z-direction, e.g. in an eliptically deformed nucleus along the symmetry axis, the nuclear potential in this model is written as

$$V(\overrightarrow{r}) = \frac{m}{2}[\omega_\perp^2(x^2+y^2)+\omega_z^2 z^2] + C\,\overrightarrow{l}\cdot\overrightarrow{s} + \text{correction term}, \tag{2.3}$$

with the ls-coupling term with constant $C = V_{ls}(\overrightarrow{r})$ [35]. The oscillator frequencies $\omega_\perp, \omega_z$, perpendicular to and along the symmetry axis z, respectively, only differ for a non-vanishing deformation and are given by

$$\omega_z^2 = \omega_0^2 \cdot (1 - \frac{4}{3}\delta), \quad \omega_\perp^2 = \omega_0^2 \cdot (1 + \frac{2}{3}\delta). \tag{2.4}$$

Here, the parameter $\delta \approx \frac{3}{2}\sqrt{5/4\pi}\beta_2 \approx 0.95\beta_2$ [38][2] denotes the dependence on the deformation, β_2 is the quadrupole deformation parameter which will be introduced in more detail in Sec. 2.1.5. The oscillator frequency ω_0 corresponds to the limit of a spherically symmetric nucleus and is assumed constant to fulfill the condition of a

[2] In literature often the parameter $\epsilon_2 = \delta + \frac{1}{6}\delta^2 + \frac{5}{18}\delta^3 + \frac{37}{216}\delta^4 + ...$ defined as an expansion in the deformation parameter δ can be found instead. The quadrupole deformation parameter can therefore be written as $\beta_2 = \sqrt{\pi/5}\cdot(\frac{4}{3}\epsilon_2 + \frac{4}{9}\epsilon_2^2 + \frac{4}{27}\epsilon_2^3 + \frac{4}{81}\epsilon_2^4 + ...)$ [39].

constant nuclear volume. These relations, for example, lead to smaller ω_z and larger $\omega_\perp$ frequencies if a deformation with $\delta > 0$ and therefore prolate deformation is considered.

The resulting single-particle energies as a function of the deformation can be visualized in Nilsson diagrams as shown in Fig. 2.4 for the protons and in Fig. 2.5 for the neutrons. The $2j + 1$-fold degeneracy of resulting levels in the spherical case is lifted in the deformed nucleus which becomes evident in the Nilsson diagrams. This leads to dense level scheme structures particularly in the range of the heavy actinides. Within these levels, smaller but sizable shell gaps can occur, in comparison to those at shell closures with spherical symmetry. Such shell gaps are marked in the shown Nilsson diagrams.

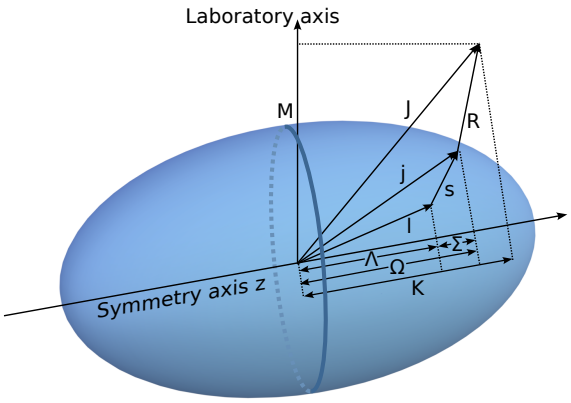

Figure 2.3.: Visualization of the asymptotic quantum numbers defined for an axially symmetric deformed nucleus. These quantum number are used in the Nilsson model to unambiguously assign individual Nilsson levels. Figure adapted from [39].

The Nilsson states can be labeled via asymptotic quantum numbers, as shown in Fig. 2.3. Here, the projection of spin and orbital angular momentum onto the symmetry axis are labeled as Σ and Λ, respectively, the quantum number $\Omega = \Lambda + \Sigma = \Lambda \pm 1/2$ denotes the projection of the total angular momentum $j = l + s$. The total angular momentum projection onto the laboratory axis is identified with M. Finally, K describes the projection of the total angular momentum J on the symmetry axis including the angular momentum R arising from the nuclear collective motion [39]. In particular, the quantum numbers $\Omega^\pi[N, n_z, \Lambda]$ are used to identify individual Nilsson levels which include the principal quantum number N, the number n_z of knots in the wavefunction along the z-axis, the quantum numbers Ω and Λ, and parity π [38].

The $N = 152$ shell gap is found between the orbitals $9/2^-[734]$ and $1/2^+[620]$ [40] which can be seen in a Nilsson diagram for the neutron single-particle orbital energies in Fig. 2.5. To give an example of the Nilsson model for fermium nuclides, the isotope ^{255}Fm features a calculated deformation of $\epsilon = 0.23$ from Finite Range Droplet Model (FRDM) predictions [41]. For the protons, this leads to an occupation of the $7/2^+[633]$ level in the ground state, as indicated in Fig. . Furthermore, a ground-state configuration of $7/2^+[613]$ for the neutron single-particle energy can be predicted from

the Nilsson diagram shown in Fig. 2.5 [42]. The former is in accordance with the experimentally known spin of $I = 7/2^+$ for this isotope [43]. The lighter isotope ^{249}Fm for instance, with the same predicted size for the deformation, features an assigned ground-state configuration of $7/2^+[624]$ [44], for ^{251}Fm a configuration of $9/2^-[734]$ was derived [40] and for ^{253}Fm a configuration of $1/2^+[620]$.

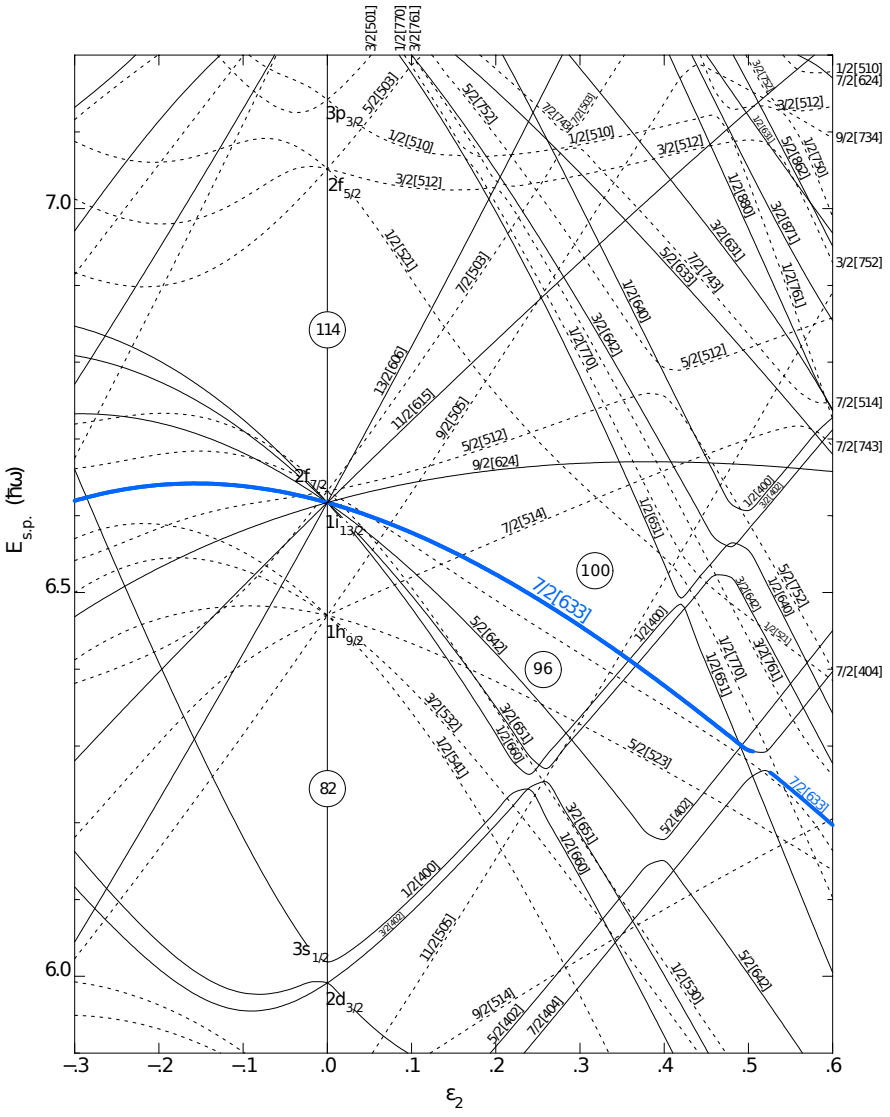

Figure 2.4.: Nilsson diagram of single-particle orbital energies for protons in heavy nuclei. Levels with even parity are shown with solid lines, odd parity states are shown with dashes lines. Sizable sub-shell gaps such as at $Z = 100$ for fermium emerge for a stronger prolate deformation. The $7/2^+[633]$ ground state proton orbital for fermium is marked in blue. Figure adapted from [39].

2.1.4. Concepts from modern nuclear theory

Describing the interactions of the single constituents within exotic nuclei far from stability requires advanced nuclear models to enable predictions on nuclear properties

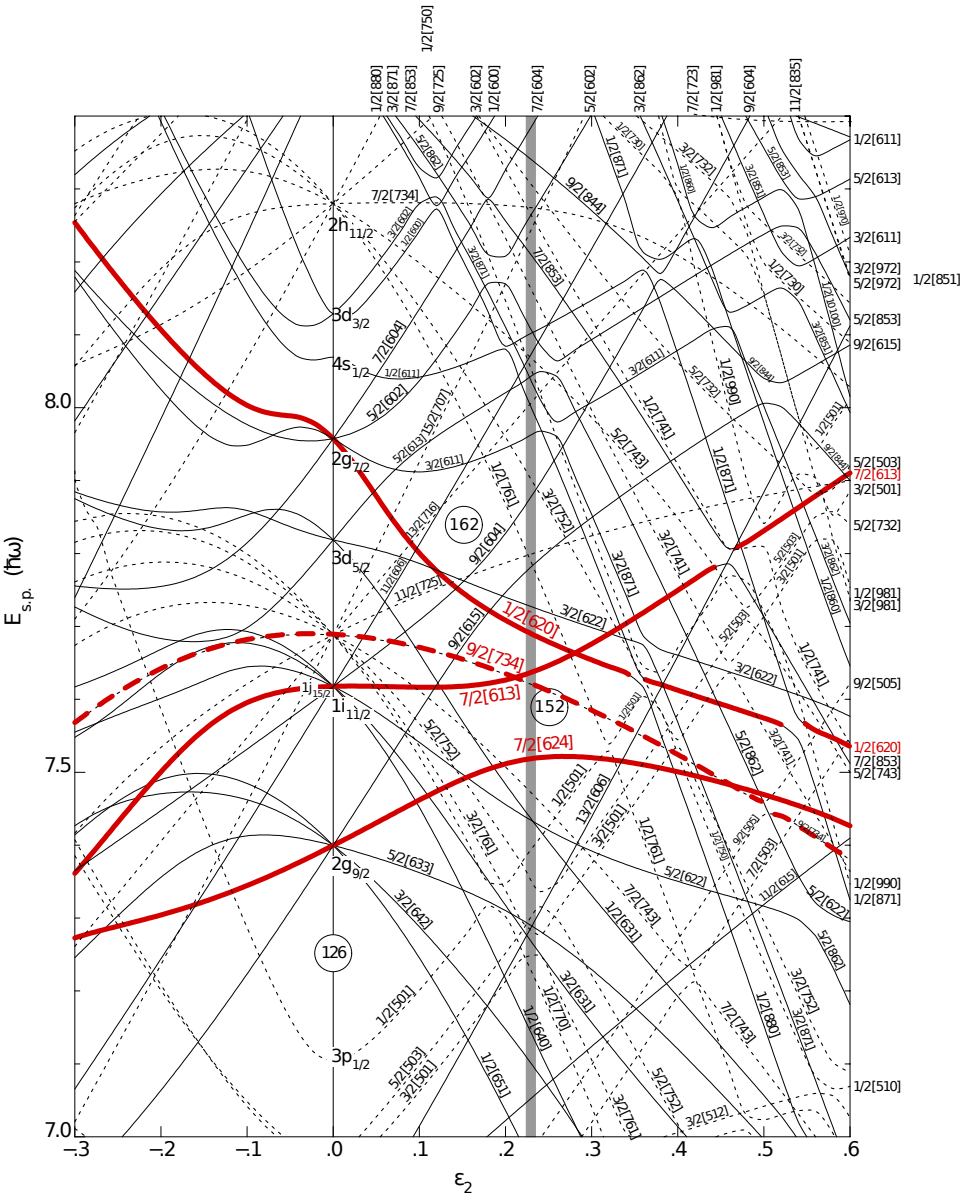

Figure 2.5.: Nilsson diagram of single-particle orbital energies for neutrons in heavy nuclei. Even- and odd-parity levels are shown with solid and dashed lines, respectively. Various sizable sub-shell gaps such as at $N = 152$ and $N = 162$ for a stronger prolate deformation. The ground state neutron orbital are marked for ^{255}Fm ($7/2^+[613]$), ^{249}Fm ($7/2^+[624]$), ^{251}Fm ($9/2^-[734]$), and ^{253}Fm ($1/2^+[620]$) are marked in red. Figure adapted from [39].

and the limits of nuclear existence. Various techniques to solve the nuclear many-body problem were developed in recent decades. These models differ substantially from their approach in the description of the nuclear interaction which affects their predictive power in different regions of the nuclear landscape. Prominent examples of such theoretical frameworks will be introduced here. A more detailed description can for instance be found in [4, 45, 46, 47].

Ab initio methods

Nuclear *ab initio* methods consider the individual protons and neutrons as the fundamental entities, and recognize that these themselves are not fundamental particles. The strong nuclear force, which is responsible for the binding of the nucleons, relies on the interaction on the quark level in the proton and neutron sub-structure. This force is mediated by gluons between these quarks. A direct description of nuclear systems using Quantum Chromodynamics (QCD) as the fundamental theory of the strong nuclear force however is currently not feasible. Instead, effective interactions between the nucleons are utilized to describe the nuclear many-body-system. The non-relativistic Schrödinger equation is then solved (approximately) directly with the developed Hamiltonian.

A powerful approach in this regard is Chiral Effective Field Theory (EFT), which is based on symmetries of QCD. As the interaction at low energies and longer distances dominates, instead of the weaker interaction at short distances, the quarks are confined into the bound form of protons and neutrons. The strong nuclear force in the low-energy regime, as is the focus of nuclear physics studies, can therefore not be analyzed perturbatively. An EFT is applied instead, in which the low- and high-energy scales, together with the active degrees of freedom for the later, are identified. The most general Lagrangian is constructed, with the nucleons and pions as main constituents, and accounting for (broken) symmetries, such as chiral symmetry of QCD (considering the lightest, almost massless quarks, up and down). An expansion of the Lagrangian in orders of two-nucleon and higher order interactions guides the calculation of Feynman diagrams by the expansion orders and their relative importance up to the desired accuracy [48].

Currently, models are limited to incorporate nucleon-nucleon or three-nucleon interactions. Unknown parameters, such as low-energy constants that describe the nucleon interactions as vertices in the Feynman diagrams, can in principle be precisely calculated from lattice QCD to access unresolved underlying physics [46]. Yet, these calculations remain out of reach and as a result, models are tuned by fitting them to experimental data [49]. Optimizing the models on experimental data demonstrated great success and provides results with good accuracy, particularly for lighter systems and moderately heavy nuclei near shell closures. However, as the number of nucleons increases, along with the associated number of degrees of freedom, the computational weight increases exponentially. Directly solving the Schrödinger equation becomes in-

feasible and requires a simplified description of the system to be computationally more efficient.

As an alternative for the description of more complex many-body systems, polynomial scaling methods were introduced. The Renormalization Group approach decouples high- and low-energy momentum degrees of freedom, meaning the separation of resolved and unresolved underlying physics, to simplify the description. The influence of high-momentum degrees of freedom, which are unimportant on the (low-energy) scale of nuclear physics studies, can thus be effectively suppressed. The weight of *ab initio* calculations for complex many-body systems is therefore drastically reduced [45, 46]. Applied methods are for instance the No-Core Shell Model, Coupled Cluster, and the Self-Consistent Green's Function which are described in greater detail in Ref. [46]. Recent remarkable advancements in *ab initio* nuclear theory allowed calculations of relatively heavy nuclei, such as ^{208}Pb, which created new opportunities for predictions using this method [50]. The newly gained access to heavier regions in the nuclear chart however is limited to nuclei close to sphericity along with applicable simplifications in the calculations to reduce the required computing power. Up to now, predictions of the heaviest nuclei far off from stability, including the actinides and SHE, remain inaccessible with this method, and pose significant challenges for this type of nuclear theory due to the complex nuclear structure featuring several valence nucleons requiring immense computational time.

Nuclear mean-field approach

To allow for a description of complex, heavy systems, such as the actinides, the complete consideration of all nucleon-nucleon interactions has to be reduced to the crucial degrees of freedom and the description therefore simplified. In the mean-field approach, the nucleon-nucleon interactions are simplified to a single nucleon moving in an average potential created by the collective presence of all other nucleons. A short introduction to two prominent approaches will be given in the following, extensive reviews and more details can be found for example in Refs. [4, 51, 41].

Microscopic-Macroscopic approach

The macroscopic LDM, as introduced in Sec. 2.1.1, enables the derivation of general trends in the evolution of nuclear parameters, such as the nuclear binding energy. However, it does not account for stabilizing effects arising from the underlying shell structure. In microscopic-macroscopic (mic-mac) methods, based on the general concept of the LDM, an additional shell-correction energy derived from a phenomenological single-particle potential is incorporated. Hence, the microscopic considerations of single-particle effects in the nuclear shell model and the macroscopic approach of the LDM are combined. This approach provides a more accurate modeling in particular of nuclei with strong stabilizing shell effects [4].

In these models, the nuclear potential energy is characterized by a macroscopic component, for instance based on the LDM, and depends on the number of the respective nucleons N, Z and the shape. A microscopic shell correction term is added which decreases as the deformation deviates from sphericity [52]. In this way, the unusual stability of spherical shapes is accounted for. In a subsequent advancement of this approach, a pairing correction term was included in the macroscopic LDM framework, in addition to the shell correction term. This modification furthermore influenced the binding energy as predicted by the model [53, 54].

The development of the semi-empirical Droplet Model (DM) enabled a further refinement of the LDM framework, and commonly serves as the macroscopic component in the mic-mac approach. In this more sophisticated model, trends in the nuclear size evolution can be deduced as the number of nucleons increases, considering effects such as non-spherical nuclear shapes, nucleon redistribution and the presence of a neutron skin. These aspects are in contradiction to the sharp spherical radius as described by the LDM [55, 56, 57]. In comparison to Eq. 2.1, a correction term is included in the radius calculations given with a scale parameter $\bar{\epsilon}$

$$R = R_0 \cdot A^{1/3}(1 + \bar{\epsilon}). \tag{2.5}$$

The model parameters included in $\bar{\epsilon}$ (see for instance in Ref. [31]) are tuned by a fit to experimental data as for instance described in Ref. [58]. A commonly considered parametrization is shown in the appendix in Sec. A.4.

Further advancement of this model led to the development of the Finite Range Droplet Model (FRDM) model, which includes advanced compressibility effects and considers the finite range of the strong nuclear force [59, 60, 61]. This refinement notably improved the description of lighter nuclei with the DM. However, the resulting uncertainties in the predictions, in particular for more exotic heavy nuclei, still prevent a satisfactory treatment. Examples of state-of-the-art nuclear mean-field model approaches, which are powerful methods especially for the description of heavier nuclei, are described as follows.

Density functional theory

To efficiently treat many-body systems of fermions in the mean-field approach, the purely microscopic Hartree-Fock (HF) method serves as a popular tool and was initially developed to treat many-electron systems in atomic physics and chemistry. In general, the stationary Schrödinger equation for the many-body system has to be solved to find the eigenstates of the system. In the independent-particle model, the many-particle fermionic wavefunction is approximated by a single Slater determinant, a product of the single-particle wavefunctions, such that the energy in the system is minimized. The resulting HF equations, which yield the single-particle energy states, are solved iteratively, making it a Self-Consistent Mean-Field (SCMF) model.

The general HF method is not suitable to treat nuclear systems as it normally does not take nucleon-nucleon interactions as pairing correlations into account, yet they strongly affect nuclear properties. Thus, an extension of this method, the Hartree-Fock-Bogoliubov (HFB) method, is often applied in which the mean-field of the nuclear potential is extended by a pairing field [4]. Different methods have been developed in recent years to account for these nucleon-nucleon interactions.

The mean-field consideration is the basis of nuclear Density Functional Theory (DFT), a phenomenological approach which can in principle be applied to nuclei all over the nuclear chart, but is particularly powerful for heavier nuclei [62]. It relies on a two-step variational concept in which the total energy of the system is a function of the expectation value of an observable. In this principle, the total energy is minimized for a fixed value of the observable. Simultaneously, a minimization of the total energy leads to the determination of the ground-state energy and the precise value of the respective observable or set of observables in this ground state [47]. In DFT, the particle density acts as the observable in the variational principle for which the total energy of the system is minimized to describe all ground-state properties of a many-body system. A so-called Energy Density Functional (EDF) can be written as

$$E = \int d^3r \epsilon(r). \tag{2.6}$$

In this way, the $3N$-fold coordinates for a system of a N-particle wavefunction can be reduced to three spatial coordinates of the density function. This significantly saves computing resources especially for calculations of larger multi-body systems.

The HFB energy (taking pairing correlations into account) can be divided for instance into terms of [4, 63]

$$E_{\mathrm{HFB}} = E_{\mathrm{kin}} + E_{\mathrm{Coulomb}} + E_{\mathrm{strong}} + E_{\mathrm{corr}}, \tag{2.7}$$

where E_{kin} is the kinetic energy, E_{Coulomb} the energy due to the Coulomb repulsion, E_{strong} the strong interaction and E_{corr} a correction term. The first three terms, the kinetic and Coulomb energy, and the energy resulting from the strong interaction, can be described using an EDF as in Eq. 2.6. The contribution E_{strong} is divided into terms of an effective and a pairing interaction. The total energy $E = E_{\mathrm{HFB}} + E_{\mathrm{corr}}$ is finally composite of the HFB energy and a perturbative correction term, including effects such as vibrational and rotational corrections [63].

Different models for an effective interaction in the mean-field approach have been developed over the last decades. The phenomenological Skyrme interaction resembles one the standard approaches [64, 4]. The Skyrme force is based on a zero-range interaction, whereas the pairing force is separately described. It can be divided into three parts, a spin-dependent two-body term, a density-dependent central part to account for N-body interactions and a spin-orbit term. By adjusting the model to

a set of nuclear observables such as binding energies or nuclear charge radii, the free parameters included in the terms can be constrained. Different parametrizations were developed in recent years, such as SV-min [65], BSkG2 [66] or SLyMR1 [67].

The Gogny interaction model as alternative is based on a finite-range interaction, which is modeled by Gaussian terms. While the two latter terms of the Skyrme force are similarly used in the Gogny force, the central part is modeled by a repulsive and an attractive Gaussian. This allows to simultaneously treat the general mean-field and long-range interactions as pairing correlations [4, 68]. The parameters contained in the individual terms are tuned via fit to finite nuclei and nuclear matter [69]. Examples of Gogny functionals are for instance D1S [70] and D1M [71].

A third type of interaction can be represented by the Fayans functional [72, 73], which is in contrast to the Gogny and Skyrme functional not based on an effective force. Generally, the kinetic energy term and the Coulomb part are adopted from the Skyrme functional but Fayans EDFs have a more complex dependence on particle densities. The respective EDF can for instance be divided into a surface, volume, and spin orbit term [74]. Specific to the Fayans functional is a density gradient included in the surface term, contrary to the density dependence of the mean-field part in Skyrme functionals. In particular, the introduction of a beyond density-dependent pairing functional incorporating a density-gradient term allows for an improved description of pairing effects such as the even-odd staggering in nuclear charge radii [73]. Examples of Fayans parametrizations are the original form FaNDF^0 [72] and more recently developed forms such as Fy(Δr, HFB) [75].

It has to be noted, that the resulting quasiparticle SCMF wavefunctions cannot preserve all symmetries of the nuclear Hamiltonian for a many-body state. However, symmetry restoration can be achieved by considering a superposition of (symmetry-broken) quasiparticle wavefunctions, as applied in schemes called multi-reference EDF performing beyond mean-field calculations contrary to common single-reference approaches.

Up to this point, only non-relativistic approaches were discussed as such EDF functionals of the Skyrme, Gogny and Fayans type are compared to experimental data in the framework of this thesis. However, also a relativistic treatment of the SCMF approach is possible as described in more detail in [76], in which the Dirac equation is solved instead. A further advancement can be made as mentioned by including beyond mean-field correlations, for example in the ground-state and low-lying excited states [4].

2.1.5. Nuclear ground-state observables

The introduced nuclear theory approaches among many others are important cornerstones, guiding experimental efforts in the investigation of nuclear ground-state properties of exotic nuclei in different regions of the nuclear chart. Conversely, ex-

perimental data on nuclear observables can be compared to theoretical predictions allowing to benchmark these models. The most prominent nuclear quantities of importance in laser spectroscopy studies and particularly in the framework of this work are introduced.

Nuclear spin

In the description of the nuclear shell model in Sec. 2.1.2, the spin-orbit coupling of the nucleon spin s with the orbital angular momentum l to the total angular momentum j was described. The nucleus finally features a total angular momentum composed of the coupling of all angular momenta j as an intrinsic property in its ground state, the so-called nuclear spin I. As the angular momentum can only take integer numbers, the total nuclear spin in the ground state of a nucleus with an odd number of protons or neutrons is strictly limited to half-integer numbers and it yields a direct indication of the nuclear sub-structure of nucleons [26]. Nuclei with both, odd numbers of protons and neutrons, will feature a spin with integer number. Only in the case of even-even nuclei, the nuclear spin is zero as both protons and neutrons are paired, resulting in the most favorable energetic configuration.

For odd-A nuclei with a single valence nucleon, the nuclear spin can be directly inferred. In the case of more than one valence nucleon outside closed nuclear shells, the nuclear spin is constituted through the coupling of the individual nucleons and can typically take values usually between $1/2$ and $9/2$ in the ground-state configuration. Higher spin states are rarely found for nuclear ground states but especially for higher excited states [35]. The nuclear spin can be obtained for instance by analyzing hyperfine structures observed in atomic transitions, see Sec. 2.2.4 for more details.

Nuclear mean-square charge radius

A quantification of the nuclear size is not trivial due to its complex structure and the diffuse boundaries. Although the nuclear radius globally increases proportional to $A^{1/3}$ as described in Eq. 2.1, shell effects, shape effects, and pairing correlations lead to a deviation from the trend given by the simple LDM [18]. Most present experiments aimed at the investigation of the nuclear size probe the electromagnetic interaction and are therefore sensitive to the nuclear charge distribution instead of the mass or nucleon distribution. The charge radius, mainly influenced by the distribution of protons in the nucleus, can in first approximation be described by the root-mean-square charge radius defined as $R_c = \sqrt{\langle r^2 \rangle}$, where [18]

$$\langle r^2 \rangle = \frac{1}{Z} \int r^2 \rho(\vec{r}) d^3 r \tag{2.8}$$

is the mean-square charge radius with the charge density distribution $\rho(\vec{r})$. By probing the charge radius, in comparison to matter radii, characteristic effects in the nucleon

distribution of exotic nuclei can be unveiled, such as halos, observed in light nuclei, or neutron skins in heavier nuclei. Common techniques to investigate nuclear charge radii include the X-ray spectroscopy of muonic atoms, electron scattering experiments and isotope shift measurements in atomic transitions [18]. Both the former techniques have only been applied to stable or long-lived isotopes, as usually large sample sizes for the target material are required. The muX experiment [77] aims at performing muonic X-ray spectroscopy in nuclei with medium to high-Z proton numbers, for instance in radium ($Z = 88$) and curium ($Z = 96$), with µg sample sizes. For the study of more exotic, short-lived nuclei however, laser spectroscopy has been proven to be a powerful tool to investigate isotope shifts. The latter is the main technique employed in this work to study heavy actinide isotopes and is introduced in more detail below.

In the evolution of mean-square charge radii over an isotopic chain, characteristic kinks were observed at spherical shell closures with $N \geq 28$ [21, 22, 23, 24]. The effect causing this observation is still under debate and different mechanisms were investigated by nuclear model calculations. One proposed cause for instance for the kink in doubly-magic ^{208}Pb was a reduced pairing in the vicinity of the shell gap [22].

Other effects reflected in the charge radius evolution are due to pairing correlations: normal Odd-Even Staggering (OES) is commonly observed as a smaller mean-square charge radius of odd-N isotopes in comparison to the mean value of their two next even-N neighbors. In the cases of an outer unpaired neutron, the Pauli-blocking effect leads to a reduction in charge radius and hence the staggering effect [18]. Directly at the spherical shell closures, the respective isotopes with magic nucleon numbers feature the smallest mean-square charge radius with respect to the average value of their direct neighbors. An inversion of the normal OES can be observed in nuclei with a specific deformation which will be introduced in the following.

Nuclear deformation

The heuristic LDM predicts spherical symmetries for nuclei in the ground state due to the minimized surface and thus an increase in binding energy. On the contrary, considering the single-particle states in the Nilsson-model framework in Sec. 2.1.3, these energy levels depend on the deformation and can therefore feature a maximum binding energy for deformed nuclear shapes. A parametrization of nuclear shapes via the nuclear radius R is often done as [78]

$$R = R(\phi, \theta) = R_0 \cdot (1 + \alpha_{00} + \sum_{\lambda\mu} \alpha_{\lambda\mu} \cdot Y_{\lambda\mu}(\phi, \theta)), \tag{2.9}$$

where the nuclear volume is conserved by the constant $\alpha_{00} = -\frac{1}{4\pi} \sum_{\lambda\mu} |\alpha_{\lambda\mu}|^2$, and given here up to second order [69]. The sum over the spherical harmonics $Y_{\lambda\mu}$, with deformation parameters $\alpha_{\lambda\mu}$, runs over all possible combinations of the orientation μ and nuclear deformation order denoted with λ [78]. For the dominant class of axially

symmetric nuclei with $\mu = 0$[3], the deformation parameter is simplified and commonly written as $\beta_i = \alpha_{i0}$, where for instance β_2 is the quadrupole deformation parameter and β_4 is the hexadecapole deformation parameter.

In general for $\lambda = 2$, therefore a quadrupolar deformation, five combinations of the parameters λ, μ are allowed giving rise to five parameters $\alpha_{2\mu}$. These can be reduced to three real parameters by rotation of the coordinate system such that the three parameters giving the orientation, the so called Euler angles, match with the main axis of the mass distribution [69]. This leaves the parameters $\alpha_{22} = \alpha_{2-2}$ and α_{20}, whereas $\alpha_{21} = \alpha_{2-1} = 0$. These can be written as

$$\alpha_{20} = \beta \cdot \cos(\gamma), \tag{2.10}$$

$$\alpha_{22} = \alpha_{2-2} = \frac{1}{\sqrt{2}} \beta \cdot \sin(\gamma), \tag{2.11}$$

with the Hill-Wheeler coordinates, namely the quadrupole deformation parameter with $\beta > 0$ and the triaxiality parameter γ [69]. All possible nuclear shapes for $\lambda = 2$ can be described in the plane with polar coordinates β and γ as shown in Fig. 2.6. As the projections on the three shown axes lead to the same shapes, they are interchangeable and all shapes can be described solely by the interval $0° < \gamma < 60°$. Here, $\gamma = 0°$ corresponds to an axially symmetric prolate deformation and $\gamma = 60°$ to a fully oblate deformation. Triaxiality is observed for all values γ between the two deformation types.

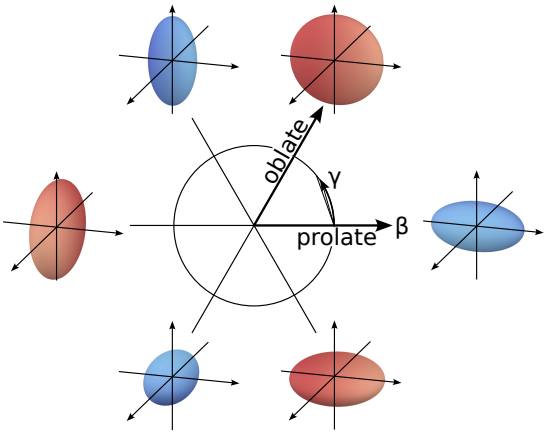

Figure 2.6.: Evolution of nuclear deformation shown in the $\beta - \gamma$-plane. Shown are purely oblate shapes in red, prolate shapes in blue. Triaxial shapes are expected between these two deformation types. Figure adapted from [69].

For the description of the size of axially-symmetric deformed nuclei, the mean-square charge radius can be deduced from an expansion of the spherical case of same volume via [18]

[3] Usually the z-axis is chosen as symmetry axis.

$$\langle r^2 \rangle = \langle r^2_{\mathrm{sph}} \rangle \cdot \big(1 + \frac{5}{4\pi} \langle \beta_2^2 \rangle\big). \tag{2.12}$$

In retrospect, an increase in deformation, accounted for by the quadrupole deformation parameter β_2, results in an increase in the charge radius. Shape effects are therefore reflected in measurements of the nuclear size evolution.

Examples of such observations can for instance be found in changes in mean-square charge radii in the yttrium ($Z = 39$) isotopic chain around $N = 60$, where a discontinuity in the size evolution revealed a sudden shape transition [79]. Another prominent feature was recently unveiled in the mercury isotopic chain [80], where a dramatic OES was observed along with a strong shape staggering as a very localized effect for these mercury nuclei.

Experiments that investigate nuclear shape effects primarily focus on probing the charge distribution shape rather than the mass distribution shape similarly as for the nuclear radius. One of the quantities which allows insight into the charge distribution shape is the electric quadrupole moment [78].

Electric quadrupole moment

With the nuclear electric quadrupole moment, deviations in the nuclear charge distribution and hence a deviation from a spherical symmetry can be quantified. The operator for the electric quadrupole moment can be written as [25]

$$\hat{Q} = e \sum_{k=1}^{A} (3z_i^2 - r_i^2), \tag{2.13}$$

with $r_i^2 = x_i^2 + y_i^2 + z_i^2$ and z_i being the coordinates of nucleon i. For nuclei with spherical symmetry, where $x = y = z$ and thus $r^2 = 3z^2$, the quadrupole moment vanishes [33].

The expectation value of this operator yields the spectroscopic quadrupole moment [25]

$$Q_{\mathrm{s}} = \langle I, m = I | \hat{Q}_z | I, m = I \rangle = \sqrt{\frac{I(2(I-1)}{(2I+1)(2I+3)(I+1)}} \langle I \| \hat{Q}_z \| I \rangle, \tag{2.14}$$

where $|I, m\rangle$ denotes the nuclear state given by the valence nucleons which now alone contribute to the quadrupole moment. This expression shows the vanishing spectroscopic quadrupole moments for $I \leq 1/2$. For well-deformed axially symmetric nuclei, thus a clear prolate or oblate deformation, in the strong-coupling limit, the spectro-

scopic quadrupole moment can be related to the intrinsic quadrupole moment Q_0 [78]

$$Q_\mathrm{s} = \frac{3K^2 - I(I+1)}{(I+1)(2I+3)} \cdot Q_0. \tag{2.15}$$

Here, K is the spin I projection onto the symmetry axis of the deformed nucleus. The intrinsic quadrupole moment dependent on the nuclear deformation denoted with β_2 can be extracted from considerations of the LDM [25] with the surface thickness a and R as in Eq. 2.1 to

$$Q_0 = \frac{3}{\sqrt{5\pi}} eZR^2\beta_2\left(1 + \pi^2\frac{a^2}{R^2} + \frac{2}{7}\sqrt{\frac{5}{\pi}}\beta_2^2\right). \tag{2.16}$$

Magnetic dipole moment

Experiments have shown that nuclei with non-zero nuclear spin can have a magnetic dipole moment which is due to single nucleons orbiting inside the nucleus. The nuclear dipole moment μ is composed of the contributions from their individual orbital angular momentum l^i and the intrinsic spin s^i with [25, 26]

$$\mu = \mu_l + \mu_s = \sum_{i=1}^{A} \frac{\mu_\mathrm{N} g_l^i}{\hbar} l^i + \sum_{i=1}^{A} \frac{\mu_\mathrm{N} g_s^i}{\hbar} s^i. \tag{2.17}$$

Here, $\mu_\mathrm{N} = \frac{e\hbar}{2m_\mathrm{p}}$ is the nuclear magneton with the proton mass m_p. The g-factors g_l, g_s for the orbital motion and the intrinsic spin component differ for neutrons and protons, where $g_l^\mathrm{p} = 1$ and $g_s^\mathrm{p} = +5.585694702(17)$, for the neutrons it is $g_l^\mathrm{n} = 0$ and $g_s^\mathrm{n} = -3.82608545(90)$ as there is no net charge. From there, the single-particle magnetic moment for a single valence nucleon in the orbital (j, l) can be derived to [26]

$$\mu_{s.p.}(j,l) = \left(g_l \cdot j - \frac{1}{2}\frac{(g_s - g_l)j}{j+1}\right) \cdot \mu_N, \quad \text{for } j = l - 1/2, \tag{2.18}$$

$$\mu_{s.p.}(j,l) = \left(g_l \cdot j + \frac{1}{2} \cdot (g_s - g_l)\right) \cdot \mu_N, \quad \text{for } j = l + 1/2. \tag{2.19}$$

These single-particle moments determined using the moments of a free proton and neutron are the so-called Schmidt moments. In this simplified picture following a single-particle shell model, the nuclear spin is solely determined by the single unpaired valence nucleon, which alone contributes to the total magnetic moment [26]. As experimentally measured magnetic moments most often differ from the Schmidt moments, effective spin-gyromagnetic factors are used for the evaluation of the measured mo-

ments instead of the g-factors of a free nucleon, for instance by using a quenching factor x such that $g_{s,\mathrm{eff}} = x \cdot g_s$. This correction which is often derived empirically from experimental data should compensate for meson exchange currents and core polarization effects which are not considered in the simple shell-model assumptions [25]. For heavy nuclei, $g_{s,\mathrm{eff}}$ is reduced to about 60 %-70 % of the free respective g-factor [78].

Furthermore, for heavier nuclei, the magnetic moment is sensitive to M1-type single particle-hole excitations, which lead to configuration mixing. The wave function therefore is not correctly described by a single particle coupling to a core with spin zero, which would not influence the magnetic moment [26]. Thus, the measured g-factors of heavy elements often deviate strongly from the single-particle g-factors used to calculate the Schmidt moments [25]. When investigating odd-odd nuclei, the coupling of both unpaired valence nuclei can lead to an even more complicated description of the system.

In odd-mass nuclei with a single unpaired valence nucleon, its single-particle characteristics can be investigated by determining the actual magnetic moment. A more pronounced collective behavior can especially be found in nuclei featuring deformed shapes, as is the case in the heaviest actinide isotopes. The magnetic dipole moment of such odd-mass nuclei can be written as [78]

$$\mu = \mu_\mathrm{N} \cdot \left[g_\mathrm{R} \cdot I + (g_\mathrm{K} - g_\mathrm{R}) \frac{K^2}{I+1} \cdot (1 + \delta_{K,1/2}(2I+1)(-1)^{I+1/2} b_0) \right], \tag{2.20}$$

where g_K is the single-particle g-factor, g_R described the rotational g-factor, K denotes the spin projection on the symmetry axis, and b_0 is the magnetic decoupling constant which only needs to be considered in the case of $K = 1/2$.

2.2. Probing atomic properties for nuclear structure studies

Atomic structure investigations yield opportunities for a deeper insight into nuclear properties of the heaviest actinides by using laser spectroscopy. A brief introduction into concepts of atomic structure studies to access nuclear structure information will be given in the following section. Therefore, the interplay of the nuclear and atomic structure will be discussed, which will motivate the laser spectroscopic investigations in this work. This method is particularly powerful to observe characteristics of both, the atom and its nucleus, despite atom-at-a-time production yields of the heavy actinide elements. For a more in-depth introduction to the atomic level structure, the reader is referred to Refs. [81, 82].

2.2.1. Electronic transitions

In the field of optical spectroscopy in general, atomic structures and hence electronic energy levels are probed by driving electronic transitions between two of such levels. Considering a two-level system with the higher level E_k and the lower level E_m, three basic processes enable a transition between these two states [82]:

1. Absorption: a transition between the two states is possible by absorption of photons from an external light field fulfilling the relation $E_k = E_m + h\nu$. The probability for absorption of a photon is given by the Einstein coefficient B_{mk} as $P_{mk}^{\text{absorb}} = B_{mk} \cdot \rho(\nu)$ and depends on the spectral energy density $\rho(\nu)$ of the external light field.

2. Spontaneous emission: a transition from the higher lying excited level E_k to E_m occurs via spontaneous relaxation by emission of a photon of energy $h\nu = E_k - E_m$ with random direction and polarization. The probability for this process can be quantified with the Einstein coefficient $P_{km}^{\text{spont}} = A_{km}$, which is connected to the lifetime of the state as $\tau_k = 1/A_{km}$.

3. Stimulated emission: a photon with energy $h\nu$ interacting with an atom in the excited state E_k promotes the transition into the lower-energetic level $E_m = E_k - h\nu$ with the emission of a photon "clone", which features identical polarization, direction and energy. Analogously to the (spontaneous) absorption, the probability can be written as $P_{km}^{\text{stim}} = B_{km} \cdot \rho(\nu)$.

Between the Einstein coefficients for the different transition processes, the following relations can be derived [82]

$$A_{km} = \frac{8\pi h\nu^3}{c^3} \cdot B_{km}, \tag{2.21}$$

$$B_{mk} = \frac{g_k}{g_m} \cdot B_{km}, \tag{2.22}$$

where $g_{k,m}$ are the statistical occupation weights for the respective states of energy $E_{k,m}$. From this relation, it becomes evident that the maximum occupation of the higher excited level E_k is limited to 50 % in the case of $g_k = g_m$. This is due to the competing spontaneous absorption and stimulated emission.

2.2.2. Spectral lineshape broadening mechanisms

Electronic transitions observed as resonances in laser spectroscopy experiments can alter in their shape and width depending on different mechanisms affecting the lineshape. Lorentzian and Gaussian contributions of different origin can alter the shape and lead to a Voigt-profile lineshape if considerable contributions of both are present. The limited resolution resulting from these broadening effects ultimately affects the accuracy with which nuclear observables can be extracted. These arising limitations need to

be considered in the choice of experimental setup and technique used to study certain nuclear properties. The different broadening mechanisms that mainly influenced the lineshape in experiments presented in this work are discussed.

Natural linewidth

The natural linewidth of a transition resonance is the minimum width observed and depends on the transition strength and the probability given by the Einstein coefficient for spontaneous emission A_{km}. Due to the Heisenberg uncertainty principle and the limited lifetime of the excited level E_k given by $\tau_k = 1/A_{km}$, the accuracy of the measured transition energy is limited to $\Delta E_{km} = \hbar/\tau_k$. Here, the Full Width at Half Maximum (FWHM) of the spectral line with Lorentzian lineshape is determined by the uncertainty in the resonance frequency [82]

$$\delta\nu_{\mathrm{nat}} = \frac{\Delta E_{km}}{h} = \frac{1}{2\pi\tau_k} = \frac{A_k}{2\pi}. \tag{2.23}$$

If the investigated transition is not involving the ground state but occurs between two excited states, both natural linewidths contribute equally and sum up to the full natural linewidth of the observed spectral line.

As an example, in the ground-state transition $^1S_0 \rightarrow ^1P_1$ first observed in the nobelium isotope ^{254}No, an Einstein coefficient of $A_{km} = 4.2^{+2.6}_{-2.8} \times 10^8\,\mathrm{s}^{-1}$ was extracted from saturation scans [27]. This transition strength yields a natural linewidth of 66.8 MHz.

Power broadening

A typical linewidth broadening effect contributing to a Lorantzian lineshape is caused by saturation of the targeted transition. In an ideal, isolated two-level system, a maximum occupation of 50 % in the excited level can be reached for high intensities of the pump-wave driving the transition, thus saturating the photon absorption. The saturation parameter can be defined as the relative pump rate $P(\nu)$ compared to the rate of relaxation as [82]

$$S = \frac{2P(\nu)}{A_{km}} = \frac{I(\nu)}{I_{\mathrm{sat}}}. \tag{2.24}$$

Saturation is reached for $I(\nu) = I_{\mathrm{sat}}$ with the intensity of the pump wave $I(\nu)$. The absorption coefficient of a saturated transition can be derived to follow a Lorentzian profile as [82]

$$a_{\mathrm{sat}} = a_0 \frac{(\gamma/2)^2}{(\nu-\nu_0)^2 + (\gamma_{\mathrm{sat}}/2)^2}. \tag{2.25}$$

A homogeneous linewidth profile with a natural linewidth of $\Delta\nu_0$ is additionally broadened to a linewidth of $\gamma = \Delta\nu_0\sqrt{1+S(\nu_0)}$ and depends on the saturation $S(\nu_0)$ for the central transition frequency ν_0. For an enhanced intensity of the incoming pump-wave, the observed lineshape is therefore broadened, often referred to as power broadening.

In Resonance Ionization Spectroscopy (RIS) experiments, other factors such as contributions from non-resonant ionization and background signal need to be additionally considered, as they affect the observed lineshape in the experiment [83]. In laser spectroscopy studies, the laser power is usually kept around saturation or just below to reduce this broadening effect while maintaining the highest efficiency to drive the respective transition.

Pressure broadening and shift

Pressure broadening of the observed spectral line and a pressure shift arise due to collisions between investigated atoms and the atoms in a buffer gas environment. This effect is particularly observed in in-gas cell laser spectroscopy experiments conducted under considerably high pressure conditions instead of a vacuum environment. An extensive review is given in [84].

The reciprocal interaction of atoms and the buffer gas leads to perturbations in the electronic energy levels. The absolute pressure or collisional broadening and shift depend on the respective observed energy level itself, the atom and buffer-gas species, and the gas density, hence the pressure and temperature [82]. During the interaction, a shift, either positive or negative, of the respective energy level can occur. The amplitude of the shift depends on the distance of both interacting collision partners, thus the buffer gas pressure. The shift in electronic levels can only be observed during the interaction time, and the initial energy values are restored after the collision interaction. This effect can be related to elastic collisions with the buffer gas finally leading to a broadening of the observed spectral line and a shift in the observed transition frequency.

Through inelastic collisions with the buffer gas, an additional broadening can be induced. The excitation energy of an atom in level E_k may be transferred to the collision partner followed by de-excitation and population transfer to a state E_m ("quenching collisions") with the probability following [82]

$$A_{km}^{\text{collision}} = N_{\text{Buffer}} \sigma_{km} \sqrt{\frac{8kT}{\pi\mu}}. \tag{2.26}$$

Parameters affecting the de-excitation probability are the reduced mass $\mu = \frac{M_{\text{Atom}} \cdot M_{\text{Buffer}}}{M_{\text{Atom}} + M_{\text{Buffer}}}$, the buffer gas density N_{Buffer}, and the collision cross section σ_{km}. Effectively, the Einstein coefficient for the respective transition can be written as $A_{km}^{\text{eff}} = \sum_m A_{km}^{\text{nat}} + \sum_m A_{km}^{\text{collision}}$. The increased transition probability consequently decreases the lifetime of the excited electronic state to $\tau_{\text{eff}} = 1/A_{km}^{\text{eff}}$. The shorter lifetime leads to a broadening mechanism in the observed transition frequency following Heisenbergs uncertainty principle.

Ultimately, the pressure broadening and shift can be described by a shifted Lorentzian-profile [85]

$$L(\Delta\nu) = \frac{1}{2\pi}\frac{\delta\nu}{(\nu - \nu_{km} + \delta\nu_{\text{shift}})^2 + (\delta\nu/2)^2}, \tag{2.27}$$

where $\delta\nu = \delta\nu_{\text{nat}} + \delta\nu_{\text{collision}}$ is the total Lorentzian FWHM considering both, natural and collisional line broadening and $\delta\nu_{\text{shift}}$ is the pressure shift. Pressure broadening and shift are proportional to the buffer-gas density ρ,

$$\delta\nu_{\text{collision}} = \gamma_{\text{collision}} \cdot \rho, \quad \delta\nu_{\text{shift}} = \gamma_{\text{shift}} \cdot \rho, \tag{2.28}$$

considering the collisional broadening and shift rate coefficients $\gamma_{\text{collision}}, \gamma_{\text{shift}}$ in units of $10^{-20}\text{cm}^{-1}/\text{cm}^{-3}$ [85]. In recent experiments on actinium in argon-buffer gas, a broadening of 11.5(10) MHz/mbar was observed for an atomic transition, while the pressure shift was in the order of -3.7(9) MHz/mbar [86]. In systematic studies of in-gas cell laser spectroscopy of erbium ($Z = 68$), the homologue of fermium, a pressure broadening of 11(1) MHz/mbar and a shift of -4(1) MHz/mbar was derived [87]. The γ_{shift} is usually positive for helium and negative for argon buffer gas.

Doppler broadening and shift

In experiments where the species under investigation, e.g., a neutral atom in laser spectroscopy experiments, is moving with a velocity v in the laboratory frame with respect to the laser, the resonance frequency as seen from the laboratory frame (ν_L) will be shifted from the resonance frequency in the rest frame of the atom (ν_0). The Doppler shift for atoms moving along the laser beam axis follows

$$\nu_L = \nu_0 \cdot \left(1 \pm \frac{v}{c}\right), \tag{2.29}$$

where the seen resonance frequency in the laboratory frame will be larger for atoms moving towards the laser source and smaller in case of the opposite direction.

The velocities of the atoms usually follow a Maxwell velocity distribution which strongly depends on the absolute temperature T [82]. The intensity profile of a Doppler-broadened spectral line in such a situation can be described as

$$I(\nu) = I(\nu_0) \cdot e^{-\left(\frac{\nu-\nu_0}{\nu_0 v_w/c}\right)^2}, \tag{2.30}$$

where $v_w = \sqrt{\frac{2kT}{m}}$ is the most likely velocity depending on the temperature T and the mass m of the investigated atoms. The broadened line is thus described by a Gaussian function. The FWHM of this Gaussian broadening contribution can be extracted as

$$\delta\nu_{\mathrm{D}} = \frac{\nu_0}{c}\sqrt{\frac{8kT\ln 2}{m}} = \frac{2\nu_0}{c}\sqrt{\frac{2RT\ln 2}{M}} \approx 7.16\cdot 10^{-7}\nu_0\cdot\sqrt{\frac{T}{M}}, \tag{2.31}$$

with the molar gas constant $R = N_A \cdot k$, N_A the Avogadro constant and $M = N_A \cdot m$ the molar mass of the studied species [82].

For in-source laser spectroscopy experiments performed in a hot cavity as the measurements at RISIKO described in 6.2.1, the resolution is mainly limited by to Doppler broadening in the range of 1-2 GHz.

2.2.3. Laser resonance ionization spectroscopy

In optical spectroscopy experiments investigating atomic level structures, laser light is frequency-tuned to drive a transition between the atomic ground state or a low-lying metastable state and the targeted energetically higher excited level. Over the past few decades, various techniques have been developed and optimized to achieve higher sensitivities for laser spectroscopy of exotic and radioactive isotopes. The different applied techniques are specifically tailored to the experimental conditions and requirements encountered at different Radioactive Ion Beam (RIB) facilities. The two main approaches can be summarized in Collinear Laser Spectroscopy (CLS) and Resonance Ionization Spectroscopy (RIS).

In CLS, fluorescence photons resulting from relaxation of the excited level are detected in dependence of the frequency of the laser driving the initial transition. Due to acceleration of the atom or ion beam up to typical beam energies in the order of tens of keV and the collinear arrangement with a narrow-bandwidth Continuous Wave (cw) laser beam, the velocity spread and thus Doppler broadening of the spectral linewidth is reduced. This allows for high-resolution laser spectroscopy with linewidths of only tens of MHz, yet with low efficiencies related to the photon detection and limitations by laser-induced background. Using bunched beams can increase the sensitivity of the technique by gating the detected photon signals on the expected arrival time of the bunch in the light-collection region. A more detailed description of CLS can be found in [17].

A complementary method for optical spectroscopy of atoms and ions and also one of the most commonly applied techniques is RIS. This method is especially applied for experiments with low production yields and for selective laser-ion sources [19, 20]. With the high sensitivity featured by this technique, especially in combination with mass spectromertry, RIS is an established method for ultra-trace analysis, for instance of various radio-isotopes in environmental samples [88]. The experiments described in this work are based on the RIS technique tailored to the isotope production via fusion-evaporation reaction.

In the simplest RIS application, as for the first time demonstrated in 1972 [89], atoms are ionized via a two-step excitation scheme as schematically shown in Fig. 2.7: excita-

tion of a valence electron to the excited level of interest is achieved by a First Excitation Step (FES) laser driving the transition. A Second Excitation Step (SES) laser, yielding the ionization step, is frequency tuned to supply enough energy to overcome the Ionization Potential (IP) for the release of the electron in the targeted excited state into the continuum. The resonant excitation process is efficient with cross sections for the FES transition in the order of $\sigma \sim 10^{-10}\text{cm}^2$ [20]. For a successful resonant laser ionization, the lifetime of the excited state has to be sufficiently long to be addressed by the next laser in the scheme. In addition, the photon flux provided by the SES or ionization step laser has to overrule the rate of spontaneous de-excitation to an eventual dark state, otherwise the atoms cannot be addressed again by the FES laser.

The final ionization step, as the SES in this two-step scheme example, can be accomplished in various manners which ultimately impose the main limitation on the efficiency of the respective RIS scheme. In general, resonant processes for ionization feature an enhanced cross section and thus a higher overall efficiency. The SES laser can either be tuned to match an Autoionizing (AI) state in the continuum or alternatively be set for excitation to a high-lying Rydberg state, followed by field or collisional ionization. The cross sections for these processes, ionization either via an AI state or Rydberg level, can be expected to be in the order of $\sigma \sim 10^{-15}\,\text{cm}^2$ and $\sigma \sim 10^{-12}\,\text{cm}^2$, respectively. A non-resonant ionization process that energetically lifts the electron in the excited state above the IP is the least efficient, exhibiting a cross section of typically only $\sigma \sim 10^{-17}\,\text{cm}^2$ [20]. This method, nonetheless, might be the only viable option for certain schemes, particularly when there is a lack of information on high-lying atomic levels or AI states.

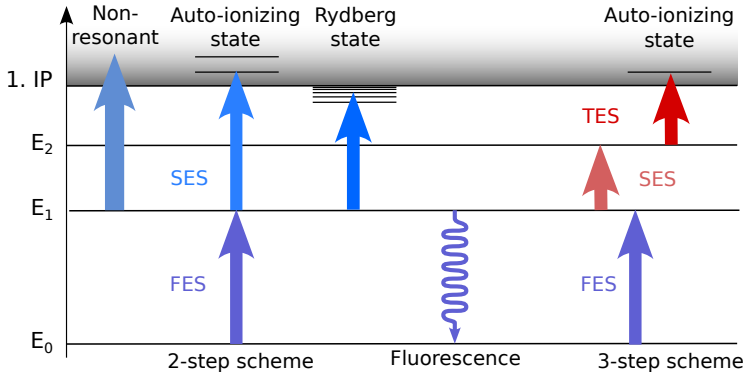

Figure 2.7.: Schematic representation of resonant laser ionization schemes for step-wise ionization of an atom. A simple two-step scheme is shown on the left with the different options for ionization using the SES laser. In comparison, a three-step scheme using two intermediate excited states and employing an AI state for ionization is shown on the right. An example of a fluorescence photon resulting from the relaxation of the targeted excited state, as detected in CLS experiments, is shown in the center.

To maximize the efficiency of resonant laser ionization, it is crucial to ensure saturation of the FES and optimization of the SES. The latter can be achieved by either utilizing a suitable AI state or by maximizing the photon flux for non-resonant ionization to

increase the ionization probability. The efficiency of the RIS scheme inherently depends on the excitation probability $dW(t)$ defined as [88]

$$dW(t) = \sigma \cdot J(t) \cdot dt, \tag{2.32}$$

with the cross section σ for the photon absorption to drive the transition and the photon flux $J(t)$. For the FES, a flux of about $J(t) \approx 10^{18}\,\text{photons/cm}^2\text{s}$ is sufficient to saturate the transition [88]. For an efficient SES, the relaxation rate of the excited state A_{km} has be considered such that $\sigma_{\text{SES}} \cdot J(t) \gg A_{km}$. For a non-resonant ionization starting from an excited state with a decay rate of $A_{km} \sim 10^7\,\text{s}$, the photon flux must be $J(t) \gg 10^{24}\,\text{photons/cm}^2\text{s}$. To fulfill this requirement, for instance considering a laser spot size of $1\,\text{mm}^2$, the flux therefore has to be greater than $\sim 10^{22}\,\text{photons/s}$, which can usually only be provided by pulsed-laser systems [17]. To enhance the duty cycle of these laser systems, which achieve the required pulse peak intensities for this technique, repetition rates of typically tens of kHz are applied. Specifically in the case of laser spectroscopy in the gas cell with atoms at thermal energies, lower repetition rate lasers in the order of hundreds of Hz can also be employed as a sufficient laser-atom interaction time is ensured.

RIS schemes, in principle, exist for every element and enable selective probing of the unique finger-print-like atomic structure. One fundamental advantage of this technique thus is the element selectivity arising from the step-wise resonant excitation and ionization. Significant development work has been carried out in recent decades to establish RIS schemes that can be applied, for instance, in hot-cavity laser ion sources for selective ion creation with isobaric suppression [90] and for ultra-trace analysis [91]. Typically, for elements with rich information on atomic structure levels, multi-step RIS schemes are applied, as for instance a three-step scheme as schematically shown in Fig. 2.7, enabling an even greater selectivity of the method.

The available information on the heaviest actinide elements remains very limited if experimental information on the atomic structure is available at all. Therefore, to date only two-step schemes with a non-resonant ionization step in most cases are available for atomic structure studies and further developments are necessary [20].

2.2.4. Hyperfine structure

Laser spectroscopy studies give access to nuclear ground-state observables by observing the hyperfine sub-structure of atomic energy levels. In nuclei with a non-zero nuclear spin I, an interaction of the nuclear moments with the total angular momentum of the atom J leads to a hyperfine splitting of atomic fine structure levels[4]. The nuclear magnetic dipole moment interacts with the magnetic field induced by the atomic electrons with strength $B_e(0)$ at the nuclear center [92]. The atomic total angular momentum and nuclear spin couple together to the total angular momentum $F = I + J$, which

[4] For a introduction to the fine structure splitting of atomic energy levels, see for example Ref. [81].

can take integer values between $F = |I - J|, ..., I + J$.

The degeneracy of the fine structure levels is partly lifted and respective sub-levels resulting from the hyperfine splitting differ by

$$\Delta E_{\mathrm{hfs}} = \frac{A_{\mathrm{hfs}}}{2} C = \frac{A_{\mathrm{hfs}}}{2} [F(F+1) - J(J+1) - I(I+1)]. \tag{2.33}$$

The hyperfine parameter A_{hfs} is sensitive to the nuclear magnetic dipole moment and the magnetic field created by the electrons as described via the relation [92]

$$A_{\mathrm{hfs}} = \frac{\mu_I B_e(0)}{hIJ}. \tag{2.34}$$

In laser spectroscopy studies on hyperfine structures involving atomic levels with a total angular momentum of $J = 0$ or $I = 0$, thus even-even nuclei, the nuclear magnetic dipole moment cannot be deduced directly but alternative techniques are required for its determination.

For deformed nuclei with a non-zero nuclear electric quadrupole moment, the hyperfine interaction with the electric field gradient created by the electrons induces a change of the hyperfine levels according to

$$\Delta E_{\mathrm{hfs}} = \frac{B_{\mathrm{hfs}}}{2} \frac{\frac{3}{4} C(C+1) - I(I+1)J(J+1)}{I(I+1)J(J+1)}. \tag{2.35}$$

This energy shift is dependent on the hyperfine parameter B_{hfs}, which can be defined with its dependence on the spectroscopic quadrupole moment Q_{s} and the electric field gradient $\frac{\partial^2 V}{\partial z^2}$ in the center of the nucleus as [92]

$$B_{\mathrm{hfs}} = \frac{eQ_{\mathrm{s}}}{h} \frac{\partial^2 V(r=0)}{\partial z^2}. \tag{2.36}$$

The electric contribution to the hyperfine interaction vanishes for nuclei with either $J \leq 1/2$ or $I \leq 1/2$. Both the electric and magnetic hyperfine interactions contribute to the total hyperfine splitting of atomic fine structure levels as the sum of these two components.

The resolution of hyperfine components in atomic transition resonances allows extracting the hyperfine parameters $A_{\mathrm{hfs}}, B_{\mathrm{hfs}}$. Information on nuclear moments can be retrieved if the atomic contributions are known and the spin can be assigned. Alternatively, a comparison to a reference isotope with known nuclear moment can enable the extraction of the same observable in the investigated exotic isotope. For the heaviest actinide elements, where stable reference isotopes are typically unavailable, the

extraction of nuclear moment information relies on model calculations for the atomic contributions $\frac{\partial^2 V}{\partial z^2}$ and $B_e(0)$ [78].

2.2.5. Isotope shift

The effect of an isotope shift can be observed when studying the same atomic transition in different isotopes of the same element. Due to the interplay of the nucleus with the atomic shell, and the changing charge distribution and mass of the nucleus, the observed atomic fine structure levels are shifted in energy relative to a reference isotope. This observable can be measured by employing laser spectroscopy over a chain of isotopes, where the reference isotope with mass number A is typically chosen as the most stable or most accessible isotope. From the measurement of the isotope shift $\delta\nu^{A,A'}$, changes in the mean-square charge radius $\delta\langle r^2\rangle^{A,A'}$ can be extracted via the relation [18]

$$\delta\nu^{A,A'} = \nu^{A'} - \nu^{A} = \underbrace{\frac{m^{A'} - m^{A}}{(m^{A'} + m_e)(m_e + m^{A})} K_{\mathrm{MS}}}_{\text{Mass shift } \delta\nu_{\mathrm{MS}}^{A,A'}} + \underbrace{F_{\mathrm{FS}}\delta\langle r^2\rangle^{A,A'}}_{\text{Field shift } \delta\nu_{\mathrm{FS}}^{A,A'}} . \tag{2.37}$$

The isotope shift can be divided into two contributions, the mass shift and field shift. Changes in the atomic levels for different isotopes arise from the change in nuclear mass and thus the change in center-of-mass motion. The electron mass m_e can be neglected when applying this relation in heavier systems. The total mass shift constant $K_{\mathrm{MS}} = K_{\mathrm{NMS}} + K_{\mathrm{SMS}}$ is composite of the Specific Mass Shift (SMS) and the Normal Mass Shift (NMS). The latter responds to the mass shift constant of a one-electron system and can in lowest order be deduced to $K_{\mathrm{NMS}} = m_e \cdot \nu$ and analytically calculated. For heavy isotopes, the NMS gives a positive contribution. The SMS on the other hand, which is due to electron correlation effects, cannot be evaluated directly and needs to be deduced from atomic model calculations [92]. In transitions of levels s→p, the NMS dominates, for transitions between higher angular momentum levels involving d or f electrons, the opposite is the case [18], and the SMS can be enhanced by an order of magnitude or more relative to the NMS.

The field shift on the other hand accounts for the finite size and shape of the nucleus and its influence on the electron energy. Electrons with a non-vanishing probability density distribution within the nucleus experience a variation in the $1/r$-potential. The field shift can be related to the changing probability density between the initial and final state involved, which can be written as $\Delta|\Psi(0)|^2_{i\to f} = |\Psi(0)|^2_f - |\Psi(0)|^2_i$, and the change in the mean-square charge radius as [92]

$$\delta\nu_{\mathrm{FS}}^{A,A'} = -\frac{Ze^2}{6\epsilon_0}\Delta|\Psi(0)|^2_{i\to f} \cdot \delta\langle r^2\rangle^{A,A'} = F_{\mathrm{FS},i\to f} \cdot \delta\langle r^2\rangle^{A,A'}. \tag{2.38}$$

This non-relativistic picture assumes a constant electron probability density inside the nucleus. In first approximation, the field shift scales with the atomic number following $\delta\nu_{\mathrm{FS}}^{A,A'} \propto \frac{Z^2}{A^{1/3}}$. In isotope shifts in transitions of heavier elements, where relativistic effects are pronounced, higher order radial moments need to be considered, as their contribution is more significant than in lighter isotopes where they are typically neglected. In this case, the field shift contribution to the isotope shift is determined from the mean-square charge radius and higher order radial moments as [18]

$$\delta\nu_{\mathrm{FS}}^{A,A'} = F_{\mathrm{FS}} \cdot (\delta\langle r^2\rangle^{A,A'} + \frac{C_2}{C_1}\delta\langle r^4\rangle^{A,A'} + \frac{C_3}{C_1}\delta\langle r^6\rangle^{A,A'} + ...). \tag{2.39}$$

The coefficients multiplied with the radial moments, the so-called Seltzer coefficients, are tabulated and can be found in [93]. In the heavy actinide region, the second order contribution to this field shift is about one order of magnitude smaller than the leading term [94]. For fermium isotopes, as shown in this work, the isotope shift is in the order of few GHz between two neighboring isotopes. With new high-resolution techniques, access to higher-order radial moments may be provided [19]. However, to investigate the difference in higher-order moments, several transitions have to be available with the respective field shift factor, which is usually not the case [95].

The isotope shift in heavy isotopes is dominated by the field shift and the the mass shift becomes negligible, whereas it dominates for lighter isotopes. Around $Z \approx 38$, both contributions to the isotope shift are of the same order, thus resulting in small isotope shifts which challenge experimental studies [92]. Therefore, for the heaviest actinide elements as for fermium, the mass shift can be omitted to a sufficient precision level when changes in mean-square charge radius are investigated.

In chains of exotic isotopes where information on mass and field shift is available for at least three reference isotopes, such as for stable isotopes previously studied via elastic-electron scattering or muonic x-ray spectroscopy, the evolution in mean-square charge radii can be extracted in a nuclear-model independent manner. This is possible as F_{FS} and K_{MS} are assumed to be constant across an isotopic chain [96].

Conversely, mass and field shift parameters of individual transitions with missing information can be extracted via the King-plot technique using measured isotope shifts of a reference transition [97]. If isotope shifts and the respective parameters in one transition i are known, they can be extracted for another transition j for which no such data exists. Here, the modification with a mass scaling factor (omitting the electron mass m_e) of Eq. 2.37 and the combination of this relation for two transitions is used for cancellation of $\delta\langle r^2\rangle^{A,A'}$. This results in [96]

$$\frac{(M_A \cdot M_{A'})}{(M_{A'} - M_A)} \cdot \delta\nu^{A,A'} = \frac{F_{\mathrm{FS},j}}{F_{\mathrm{FS},i}} \cdot \frac{(M_A \cdot M_{A'})}{(M_{A'} - M_A)} \cdot \delta\nu_{A,A'} + K_{\mathrm{MS},j} - K_{\mathrm{MS},i}\frac{F_{\mathrm{FS},j}}{F_{\mathrm{FS},i}}, \tag{2.40}$$

where $\frac{F_{\mathrm{FS},j}}{F_{\mathrm{FS},i}}$ is the slope and $K_{\mathrm{MS},j} - K_{\mathrm{MS},i}\frac{F_{\mathrm{FS},j}}{F_{\mathrm{FS},i}}$ the intercept in a King plot. Recently, new interest started arising in the search of nonlinearities in King plots [19, 98], reflecting the need to extend Eq. 2.40 by additional terms. Such contributions may be attributed to a new force mediated by a hypothetical boson between electrons and neutrons, thus giving a hint on a dark matter candidate and physics beyond the Standard Model. In addition, the observation of such effects could yield new experimental access on nuclear observables such as on higher-order radial moments [19]. In studies of the heaviest actinides, sparse experimental information on atomic parameters, if available at all, does usually not allow for a King-plot analysis, but requires predictions from atomic theory on respective parameters.

2.2.6. Calculating atomic factors in heavy multi-electron systems

The accuracy on changes in mean-square charge radii extracted from experimental data on isotope shifts is limited by the experimental factors such as the achieved spectral resolution and limitations on the accessible sample size. As discussed in Sec. 2.2.5, access to the charge radius information requires information on mass and field shift parameters, which need to be accessible from (stable) reference isotopes and a respective King-Plot analysis. However, for the heaviest actinide elements such experimental information is almost entirely missing, leaving experimentalists in need of input from atomic model calculations. The accuracy of such predictions therefore poses further limitations for the precision of the extracted mean-square charge radius.

Calculations of mass and field shift factors were initially focused on alkali-like atoms to estimate the change in the (non-relativistic) electron-density distribution $\Delta|\psi_{e^-}(0)|^2$ for a s-p transition in the isotopes A and $A+1$ [17]. For these systems, simple approximations were derived which were previously reliably used, however not accounting for effects such as screening of the s-electron and electron correlations. For the description of more complex transitions, possibly not including the ground state, and for the consideration of electron-electron correlations, *ab initio* calculations can be employed. The mass shift, separated in NMS and SMS as described in Sec. 2.2.5, can partly be calculated exactly, yet the SMS needs to be derived from atomic models. Relativistic effects in the model calculation of the mass shift complicate the treatment of complex shell structures such as in the heavy actinides. An insufficient treatment of electron-electron correlations and relativistic effects often leads to large uncertainties in the prediction of the mass shift [96]. Nonetheless, for heavy systems the mass shift contribution is negligible and hence often omitted in atomic model calculations for the extraction of changes in mean-square charge radius [99].

A powerful approach to treat complex atomic systems systems with open shells are multi-configuration methods. These are based on the Dirac-Hartree-Fock approach, which combines the Hartree-Fock idea as described in Sec. 2.1.4 with the consideration of relativistic effects described by the Dirac equation. Electron-correlations are in principle neglected when using the HF approach, as only a single electron configuration

is considered. For heavier elements, this assumption is increasingly inaccurate and correlations have to be included in the description. Instead, multiple configurations with different sets of orbitals can be considered: the state function of an atomic state is represented through a linear combination of single Slater determinants, here called Configuration State Functions (CSF), which are built as a product of sets of active orthonormal orbitals. This yields atomic state functions here denoted with $\psi(PJM)_\alpha$, with quantum number for parity P, total angular momentum J, and M the projection [100]. By increasing the configuration space with more and more active orbitals, the full space is systematically approached towards the limit of an exact description of the atomic state [101]. Two of the main techniques utilized to solve the atomic-many-body problem for complex open-shell systems are the Configuration Interaction (CI) and the Multiconfiguration Dirac-Hartree-Fock (MCDHF) approach.

In the latter approach, the Dirac-Coulomb Hamiltonian

$$H_{\mathrm{DC}} = \sum_i h_{\mathrm{Dirac}} + \sum_{i<j} \frac{1}{r_{\mathrm{ij}}} \tag{2.41}$$

is applied to solve the eigenvalue problem $H_{\mathrm{DC}}\psi(PJM)_\alpha = E_{PJM}\psi(PJM)_\alpha$ which is derived from a variational problem to minimize the total energy. The one-electron Dirac-operator h_{Dirac} accounts for the interaction of the single electron with the potential given by the nucleus, while the second term considers the interaction through Coulomb repulsion with the other (N-1) electrons. To acknowledge enhanced relativistic effects in the heavy elements, this term is extended to $\sum_{i<j}(\frac{1}{r_{\mathrm{ij}}} + b_{\mathrm{ij}})$ by adding the transverse Breit interaction. In addition, a local single-electron Hamiltonian $H_{\mathrm{QED}} = H_{\mathrm{SE}} + H_{\mathrm{VP}}$ with effective self-energy and vacuum polarization terms can be included for Quantum Electrodynamics (QED) corrections [100]. However, these effects are rather small compared to electron-correlation effects.

In the CI approach, "frozen" inner-shell orbitals may be assumed with fully occupied CSF as starting point for the calculations. An effective Hamiltonian is constructed for the number of valence electrons M as [102]

$$H_{\mathrm{eff}} = \sum_{i=1}^{M} h_1(r_i) + \sum_{i<j} h_2(r_i, r_j), \tag{2.42}$$

where the first term describes the single-electron contribution including the correlation with the frozen electron-core. The latter term gives the Coulomb interaction of the valence electrons corrected by a correlation operator. The Breit interaction can additionally be included. The single-determinant wavefunctions are formed for the single-valence electron basis states in the frozen core Dirac-Fock potential V^{N-M}, with N being the total number of electrons in the system [102]. Similarly as before, the many-electron energies and respective weights are extracted by solving the eigenvalue problem. As here usually core-excitations are neglected, the simple CI method looses

in accuracy especially for heavier systems, such that a combination with Many-Body Perturbation Theory (MBPT) to CI+MBPT is often used. With this approach, core excitations are included via perturbation-theorems on the effective Hamiltonian [103].

In order to assess the accuracy of these models especially for complex modeling of many-body systems, a comparison to simpler, lighter systems with similar electronic configuration can be made [78]. By increasing the set of active orbitals in MCDHF, the convergence of the calculations can systematically be investigated allowing to revise the model accuracy [101]. Similarly, treating the extended configuration space for atoms with a large number of valence electrons perturbatively in the case of CI allows reaching an accuracy of a few percent [104]. As higher-order electron-correlation corrections are often overruling QED corrections, for instance predicted in transition energies in the heaviest elements [105], these might be omitted in the calculations in view of the achievable accuracy of a few percent, as was seen in predictions for nobelium [102].

3. Current knowledge on the fermium nuclear and atomic structure

The chemical element fermium with proton number $Z = 100$ belongs to the chemical group of the actinides and is one of the heaviest members in this group. This exotic element does not occur in nature but instead has to be artificially produced. First discovered in 1952 during nuclear weapon tests, fermium was created in the high neutron flux and following neutron-capture processes of the uranium bomb material of the "Mike" detonation [106].

Despite the discovery of fermium several decades ago, the available atomic and nuclear structure information remains limited. The following section compiles the key information that served as the starting point and motivation for the investigations in this work.

3.1. Available nuclear structure information in fermium around *N*=152

In various experiments relying on nuclear decay-spectroscopy, fermium isotopes have been investigated on their ground state properties and excited level schemes. However, the available information especially on the introduced ground-state properties in Sec. 2.1.5 remains sparse. To date, the majority of the nuclear ground-state spins of fermium isotopes could only be tentatively assigned, as is shown in Fig. 3.1. Here, laser spectroscopy studies can give a decisive benefit, as the spin can be unambiguously assigned by resolving the hyperfine structure in atomic transitions.

Figure 3.1.: Known and tentatively assigned nuclear spins in fermium isotopes. The color coding reflects the main decay channels. Given spin assignments are following to the information from the ENSDF database[1].

A first laser spectroscopy study on ^{255}Fm, as is described in the following part, attempted to examine the hyperfine structure of an atomic transition. Due to the insuf-

[1]From ENSDF database as of October 22, 2023. Version available at http://www.nndc.bnl.gov/ensarchivals/

ficient spectral resolution inherent in the measurement technique, only estimates could be made on the nuclear electromagnetic moments [107]. These available values have to be handled with precaution, as large uncertainties of about 50 % were estimated for the extracted hyperfine constants. A magnetic dipole moment of $\mu_I = -3.46\,\mu_N$ was derived besides a spectroscopic and intrinsic quadrupole moment of $Q_s = 4.93\,\mathrm{b}$ and $Q_0 = 10.6\,\mathrm{b}$.

More recent nuclear spectroscopy experiments focused on the study of systematic trends of shell effects in fermium, and neighboring elements, around the shell gaps $N = 152$ and $Z = 100$ in a region of strong deformation. An extensive review of these studies can be found in Ref. [15]. This shell gap is reflected in the neutron shell gap parameter, defined as

$$\delta_{2n} = 2E_B(N,Z) - E_B(N-2,Z) - E_B(N+2,Z), \tag{3.1}$$

with the nuclear binding energy $E_B(N,Z)$. An enhancement of the neutron shell gap parameter of the heaviest actinide elements around $N = 152$ is indicative of the shell gap as visualized by the color-coding in the nuclear chart cut-out in Fig 3.2. The location of this shell gap was determined and its size accurately quantified. The shell gap parameter was measured with high-precision mass measurements in nobelium and lawrencium isotopes [13], and found to be about a factor of four weaker than that at the magic shell closure at $N = 126$ for the doubly-magic nucleus ^{208}Pb.

Complementary in-beam spectroscopy studies have contributed to a deeper understanding of the nuclear structure around this shell gap. Investigations of fermium isotopes around the $N = 152$ neutron shell gap are of special interest, as they also feature the proton shell gap at $Z = 100$. Even-even isotopes, spanning from $N = 146$ to $N = 156$, were investigated on their excited level schemes. Particularly the excitation energies of the first 2^+ state are of interest as they serve as a probe for deformation and shell effects [15]. The $E(2^+)$ (relative to the first $E(4^+)$ energy) is reflected in rotational bands, as observed for the isotopes ^{246,248,250}Fm [111, 112, 113]. It provides information on the moments of inertia and, in turn, on the evolution of deformation. Pairing correlations are expected to be reduced in the vicinity of the shell gap, leading to an increased moment of inertia. In systematic trends, it would be expected that ^{252}Fm, featuring both shell gaps, exhibits the highest moment of inertia and the lowest $E(2^+)$ energy, along with a maximum deformation.

In the systematic behavior of $E(2^+)$ energies extracted for even-even fermium isotopes and other even-even heavy actinide isotopes, a minimum is seen in the fermium chain at $N = 152$, as shown in the inset in Fig. 3.2, confirming a maximum quadrupole deformation for this nucleus. For ^{250}Fm, a deformation parameter $\beta_2 = 0.28 \pm 0.02$ was extracted indicating the strong prolate deformation [113]. The (prolate) axially symmetric deformation in fermium isotopes additionally facilitated the observation of K-isomers. Such an isomeric state was identified early on in ^{250}Fm with a half-life of 1.8(1) s [114], another longer-lived isomer was identified in ^{247}Fm with a half-life of 5.1 s

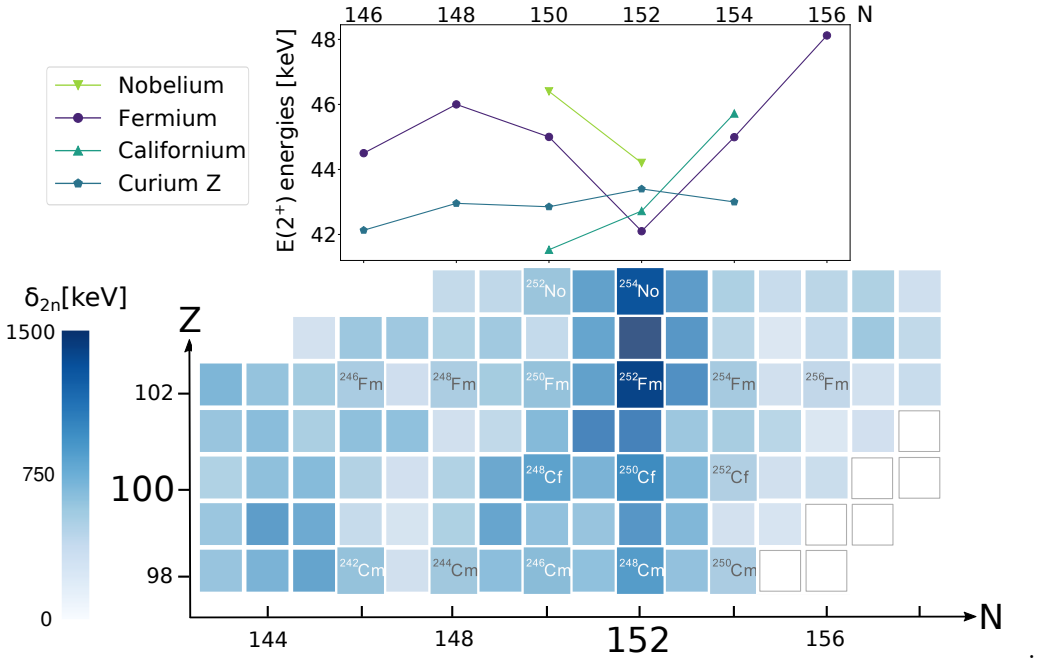

Figure 3.2.: Cut-out of the nuclear chart in the region of the heaviest actinide elements. The color coding reflects the size of the neutron shell gap parameter δ_{2n}. The data for this plot is taken from the Atomic Mass Evaluation 2020 [108]. The additional inset shows $E(2^+)$-excitation energies for even-even nuclei which indicate a minimum and thus a maximum deformation in the ^{252}Fm nucleus [15]. The data is taken from the ENSDF database[2] and from additional publications [109, 110, 111].

[115], while shorter-lived isomers are found in ^{248,251,256}Fm as tabulated in Ref. [116] and in ^{253}Fm [117].

3.2. Prior information on atomic structure properties in fermium

The existing information on the atomic level structure in fermium to date is scarce, as experimental studies are hampered by the limited sample access for detailed experimental studies and short half-lives for most of the isotopes. A detailed description on production mechanisms for fermium isotopes is given in the following chapter 4.

Until about two decades ago, fermium was the heaviest element for which no experimental information on its atomic level structure was available. Solely the ground state configuration was known to be $5f^{12}7s^2\ ^3H_6$ [118]. The development of the Ion Guide-detected Resonance Ionization Spectroscopy (IGRIS) method, tailored to the study of

[2] From ENSDF database as of October 22, 2023. Version available at http://www.nndc.bnl.gov/ensarchivals/

transuranium elements [119], yielded the first experimental insight into excited levels in fermium. In this method, the advantages of resonance ionization mass spectrometry and laser spectroscopy of atoms evaporated from a filament in a buffer gas cell were combined (the latter being the main method used in the RADRIS technique introduced in Sec. 4.3.1). A detailed description of this technique can be found in Ref. [120].

For the fermium level search campaign with IGRIS, a sample of about $2.7 \cdot 10^{10}$ atoms of ^{255}Fm was available. Guided by predictions from MCDHF calculations, two atomic levels were found at 25 099.8(2) cm^{-1} (denoted as transition R1) and 25 111.8(2) cm^{-1} (denoted as transition R2) transition wavenumber[3] from the ground state by applying a two-step RIS scheme with non-resonant ionization step. An upper limit on the ionization potential was extracted as 54 250 cm^{-1} in accordance to early predictions of 52 400(600) cm^{-1} [121]. In a second campaign, two more filaments of ^{255}Fm with $3 \cdot 10^{10}$ atoms and $8 \cdot 10^{10}$ atoms were available for further studies together with a sample of $3 \cdot 10^{8}$ ^{257}Fm atoms [107]. In summary, seven atomic levels were identified and for four of these the ground-state transition strengths determined. A transition rate of $A_{km} = 3.5 \cdot 10^{6}\,\mathrm{s}^{-1}$ was found for R2, similarly a rate of $A_{km} = 3.4 \cdot 10^{6}\,\mathrm{s}^{-1}$ was found for R1, about two orders of magnitude smaller than for the known ground-state transition $^{1}S_0 \rightarrow ^{1}P_1$ in nobelium [27].

These two levels were re-investigated with a narrow-band dye laser system of 1.5 GHz linewidth. However, hyperfine structure, considering a spin of $7/2$ [43], in the respective transitions could not be fully resolved but strongly broadened structures were detected. The analysis of the data, also considering saturation and optical pumping effects, provided indications of a transition type $J = 6 \rightarrow 6$ for R1 and $J = 6 \rightarrow 5$ for R2, which aligned with MCDHF predictions. A definite assignment from the experimental data, however, was not possible. Hyperfine constants were derived from fitting the observed structures, but uncertainties of about 50 % had to be taken into account. This hindered a better determination of values for the magnetic dipole moment and electric quadrupole moment [107].

The previous work on ^{255}Fm provided first insight into the atomic structure of fermium, revealing several ground-state transitions. However, due to the limited resolution and sample size, a detailed investigation of nuclear ground-state properties, such as nuclear moments or the evolution of mean-square charge radii could not be achieved. The experiments on fermium isotopes described in this thesis build upon the initial work by Backe et al. [107], used the previously identified transition R2, as shown in the RIS scheme in Fig. 3.3. This scheme was utilized for all experiments on fermium described in this work.

[3] The notation of the respective transitions with R1 and R2 follows the nomenclature used in Ref. [107].

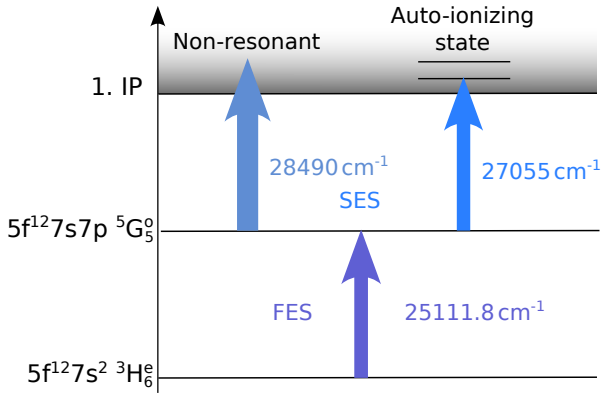

Figure 3.3.: RIS scheme applied for laser spectroscopy studies of fermium isotopes in this work. The FES was initially identified in off-line in-gas cell laser spectroscopy experiments on ^{255}Fm reactor-breeding samples [107]. The AI was found in the first fermium off-line experimental campaign on ^{257}Fm described in Sec. 6.2.3. The scheme here is shown with the FES targeting ^{255}Fm.

3.3. Extracting nuclear information from isotope shifts in fermium

To extract information on the change in nuclear mean-square charge radius from the measured isotope shift, the atomic mass shift and field shift factors have to be available. Regarding the investigated transition, or any other transition in fermium, no experimental information is available concerning these parameters. Consequently, conducting a King-plot analysis is not feasible. Instead, calculations of these atomic properties from theory can be utilized. Due to the complex electron configuration including the open f-shell in some actinides, theoretical calculations are challenging and still limited in availability. Recent advancements have provided some access to predictions for the actinides, including fermium.

Calculations applying CI in combination with perturbation theory by Allehabi et. al. [99] predicted field shift parameters for different transitions in fermium, particularly for the previously experimentally observed transitions [107]. The authors derived a field shift of $F_{\mathrm{FS}} = -3.14\,\mathrm{cm}^{-1}/\mathrm{fm}^2$ from their calculations for the transition R2, which was employed for the further analysis described in chapter 7. For the evaluation of changes in nuclear mean-square charge radii in fermium, the mass shift is expected to be insignificant enough to not contribute to the isotope shift [99].

Previous studies in other heavy actinide elements such as nobelium [28] adopted a similar approach by using only the field shift parameter from atomic models. In lighter nuclides, this approximation is not valid and the consideration of the mass shift is necessary, as was demonstrated in other laser spectroscopy ivestigations. These studies incorporated the mass shift either available from theoretical calculations or by employing a King plot analysis, see e.g. [122] and [123].

With the approximation of the negligible mass shift for fermium, changes in $\langle r^2 \rangle^{A,A'}$ can be calculated from the the observed isotope shift with

$$\delta\langle r^2 \rangle^{A,A'} = \delta\nu^{A,A'} \cdot \frac{1}{F_{\mathrm{FS}}}. \tag{3.2}$$

For convention, it has to be stated that the isotope shift is considered as $\delta\nu^{A,A'} = \nu^{A'} - \nu^{A}$, where ν^{A} denotes the transition frequency of the reference isotope, $\nu^{A'}$ denotes the transition frequency of the investigated isotope that exhibits the isotope shift.

4. Towards laser spectroscopy of heavy actinides

The level scheme structures of atoms, ions, and molecules have been investigated by applying laser spectroscopy for several decades. The first implementation of frequency tunable laser systems created opportunities for the developments of a variety of techniques, which have since evolved into powerful and highly sensitive tools for extracting nuclear structure information from atomic properties.

In particular, laser spectroscopy on radioactive isotopes has gained importance in the atomic and nuclear physics community. Studies of this nature are now being conducted at RIB facilities worldwide, which employ various production methods and techniques. Specific challenges emerge for the study of the heavy actinide elements with low yields of only a few particles per second or even less along with a separation from the primary beam necessitated for in-flight production schemes.

The main experimental techniques required for the initial production, the preparation of respective reaction product nuclei and the basic methodology of laser spectroscopy of the heaviest actinide isotopes are introduced. A general broad overview over laser spectroscopy techniques for nuclear structure studies can be found in Ref. [17] and [19], a focus on the actinides is given in Ref. [78].

4.1. Experimental access to the heaviest actinide elements

Chemical elements up to the light actinide element uranium ($Z = 92$) are naturally abundant in the Earth's crust. Until today, the high abundance of most of these elements allowed for intensive studies focused on their atomic and nuclear structure, including laser spectroscopy investigations. Despite the inherent instability of all actinide elements ranging from actinium ($Z = 89$) to lawrencium ($Z = 103$) against radioactive decay, trace-amounts of the primordial, long-lived actinide isotopes ^{232}Th (thorium, $Z = 90$), ^{235}U, and ^{238}U can be found in nature. In addition to these mainly abundant daughter nuclides from primordial decay chains, other isotopes of elements from actinium to uranium are naturally occurring. More exotic isotopes of the lighter actinides further away from stability need to be synthesized via nuclear reactions, e.g., spallation and fragmentation, for detailed studies at operational RIB facilities such as ISOLDE, CERN [124], TRIUMF [125] and other future facilities [126, 127]. Access to heavier actinide elements is gained by two techniques described as follows.

4.1.1. Production via reactor-breeding processes

To access long-lived, neutron-rich transuranium nuclides, macroscopic sample sizes can be produced via breeding processes in nuclear reactors [20]. The high neutron flux in these reactors promotes neutron-capture processes followed by subsequent β^--decays. The isotopes in reach and the respective yields depend on the cross sections of neutron capture and β^--decay branching ratios, as well as the half-lives of the nuclides in the breeding-path. In this way, certain long-lived isotopes of actinide elements ranging from neptunium ($Z = 93$) to fermium ($Z = 100$) can be produced in sample sizes of milligram to femtogram, depending on the isotope. As there are no β^--decaying fermium isotopes in reach via the breeding chain, as indicated by the color-coding in the cut-out of the nuclear chart shown in Fig. 4.1, the breeding path is naturally interrupted and heavier elements cannot be accessed.

Samples in femtogram amounts of the neutron-rich isotopes ^{257}Fm ($t_{1/2} = 100.5\,\mathrm{d}$) and ^{255}Fm ($t_{1/2} = 20.1\,\mathrm{h}$) for off-line laser spectroscopy studies in this work were produced via reactor breeding. The main breeding-path of the utilized reactor-based production scheme is marked in Fig. 4.1.

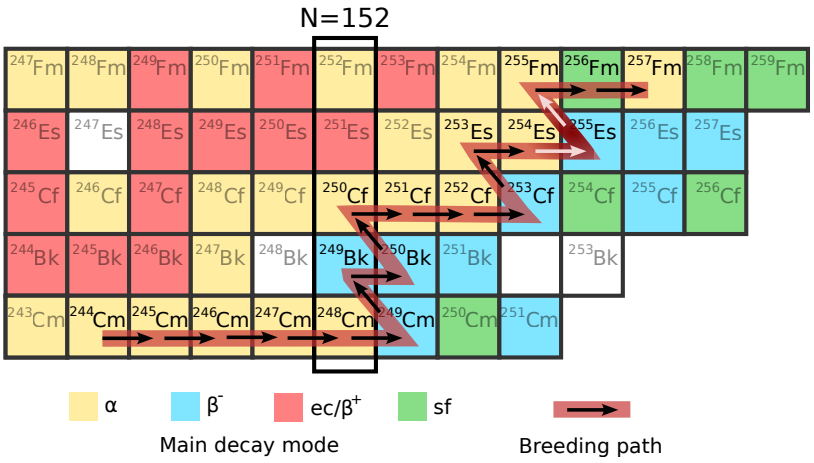

Figure 4.1.: Nuclear reactor-breeding path leading to long-lived fermium isotopes ^{255}Fm and ^{257}Fm. Black arrows indicate the main breeding path for the initial production of the latter isotope at the HFIR at ORNL. The white arrows indicate the re-irradiation of remaining ^{254}Es from the previous sample at ILL for production of ^{255}Es decaying to ^{255}Fm.

During breeding of initial curium targets containing $^{244-248}$Cm in the High Flux Isotope Reactor (HFIR) at Oak Ridge National Laboratory (ORNL), USA, macroscopic amounts of long-lived products such as ^{254}Es ($t_{1/2} = 275.7\,\mathrm{d}$) were produced [128, 129]. The continuing neutron-capture processes, in conjunction with β^--decays, facilitated the breeding path up to ^{257}Fm to proceed as marked by black arrows in the figure. The later re-irradiation of a fraction of the initial ^{254}Es HFIR sample in the high-flux reactor for research purposes at Institute Laue-Langevin (ILL) Grenoble, France, allowed breeding of ^{255}Es ($t_{1/2} = 39.8\,\mathrm{d}$). The latter undergoes β^--decay followed by ingrowth

of ^{255}Fm, providing access to this particular isotope for off-line measurements. The respective breeding and successive decay path is indicated in Fig. 4.1 with gray arrows. A subsequent chemical separation of ^{255}Fm from the ^{255}Es mother allowed the preparation of samples to be used for hot-cavity laser spectrosocopy. Further experimental details and findings are discussed in chapter 6 and subsequent chapters.

4.1.2. Accelerator-based production

For the study of the heaviest actinides beyond fermium and the SHEs, as well as for investigating more neutron-deficient isotopes of heavier actinide elements, their synthesis through fusion-evaporation reactions at accelerator facilities becomes essential. Such production schemes were used for the synthesis and finally the discovery of the SHEs with $Z = 107 - 118$ [78]. A more in-depth review can be found for instance in Ref. [130].

To induce nuclear fusion-evaporation reactions, a projectile beam is accelerated to a kinetic energy $E_{\mathrm{kin}}^{\mathrm{proj}}$ approaching the Coulomb-barrier. Typically, beam energies ranging from 4 MeV/u and 6 MeV/u are aimed for. The accelerated beam is subsequently directed towards a thin-foil target of about 0.5 mg/cm^2 areal thickness for bombardment. If the kinetic energy of the projectile is sufficiently high to overcome the Coulomb repulsion and penetrate the target nucleus, it can lead to the formation of a highly excited compound nucleus C* resulting from the fusion of both reactants, as schematically shown in Fig. 4.2. The excitation energy of C* can be derived as $E^* = Q - E_{\mathrm{kin}}^{\mathrm{proj}}$ [78], where the Q-value or reaction energy is given by

$$Q = \Delta m c^2 = (m_{\mathrm{compound}} - m_{\mathrm{target}} - m_{\mathrm{projectile}}) \cdot c^2. \tag{4.1}$$

Regarding the excitation energy E^*, fusion reactions can be classified in two categories: hot-fusion reactions, where 20 MeV $< E^* <$ 40 MeV, and cold-fusion reactions, where $E^* <$ 20 MeV. The compound nucleus, forming an intermediate stage in the reaction, has a short lifetime in the range of 10^{-14} - 10^{-19} s and will, in most cases, undergo rapid fission [78].

For de-excitation of a formed compound nucleus, different exit channels can compete. The compound nucleus can stabilize through the evaporation of few particles to form the final product nucleus. Typically, ejected particles include neutrons, protons, alpha-particles, and the combination of them. A reaction with an exit channel featuring the evaporation of several neutrons can be written as

$${}^{A}Z_{\mathrm{target}}({}^{A'}Z_{\mathrm{projectile}}, x\mathrm{n})^{A+A'-x\mathrm{n}}Z_{\mathrm{product}}. \tag{4.2}$$

Here, as discussed for a complete fusion, the proton number of the product nucleus is $Z_{\mathrm{product}} = Z_{\mathrm{target}} + Z_{\mathrm{projectile}}$, all denoting the respective proton number of the reaction partners, and A, A' giving the respective mass number. Besides a complete fusion and the creation of a compound nucleus, other reaction scenarios are possible,

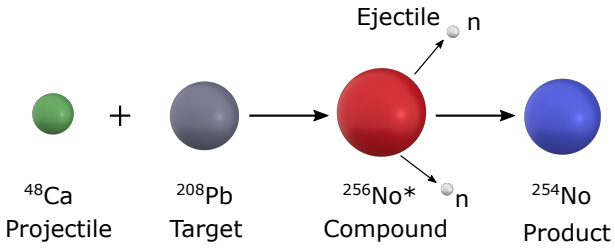

Figure 4.2.: Visualization of a fusion-evaporation reaction with a two neutron evaporation channel. In this reaction, ^{48}Ca projectiles from the accelerated primary beam bombard an isotopically enriched ^{208}Pb target to form a ^{256}No* compound nucleus. In the outgoing channel two neutrons are evaporated and a ^{254}No product nucleus is formed.

as for instance multi-nucleon transfer reactions [131]. In heavy-ion fusion reactions, thin-foil targets are typically selected. This allows the few resulting reaction residues, with kinetic energies in the order of tens of MeV, to recoil from the target and be studied in subsequent experiments.

The probability for such a fusion-evaporation reaction to occur is small, as most projectiles will instead be scattered elastically. The cross section for the formation of a specific product nucleus can furthermore be factorized in two parts: the initial capture of a projectile and the fusion with a target nucleus to form the compound nucleus, and the survival probability of the compound nucleus challenged by rapid fission [78]. Typically only a few product nuclei per second or less are produced, as it can be estimated from the cross sections shown in Tab. 4.1. By analyzing the excitation function of a specific reaction, which gives the cross section as a function of the primary beam energy or the excitation energy E^{*}, respectively, the optimal beam energy for a maximized production yield can be determined. Exemplary excitation functions calculated with the statistical code HIVAP [132] and measured for different neutron evaporation channels of the ^{48}Ca+^{208}Pb reaction are shown in Fig. 4.3. In this example, it can be observed that the exit channel for the evaporation of more neutrons only opens once the compound nucleus excitation energy is sufficiently high to facilitate the respective de-excitation process. Typically, E^{*} is reduced by 8 MeV per evaporated neutron in a reaction like this example, corresponding to the nucleon binding energy [78].

One of the highest cross sections, with about 2 µb, is obtained for the ^{208}Pb(^{48}Ca,2n)^{254}No reaction schematically shown in Fig. 4.2. The high cross section is due to the doubly-magic nature of both, projectile and target nucleus of the reaction, which results in a very high Q-value of the reaction. In this case, ^{254}No product nuclei, with the primary beam energy given in Tab. 4.1, recoil with about 40 MeV from the thin target. Via a similar production mechanism using cold-fusion reactions, on-line produced neutron-deficient fermium isotopes are in reach. However, the direct production usually features unfavorable target-beam combinations and low cross sections which challenge experimental studies.

Isotope	Reaction	Primary beam energy	Cross section
^{155}Yb	^{112}Sn(^{48}Ca,5n)^{155}Yb	4.55 MeV/u	7000 nb [133]
^{245}Fm	^{208}Pb(^{40}Ar,3n)^{245}Fm	4.85 MeV/u	15 nb [134]
^{246}Fm	^{208}Pb(^{40}Ar,2n)^{246}Fm	4.70 MeV/u	22.5 nb [134]
^{251}No	^{206}Pb(^{48}Ca,3n)^{251}No	4.80 MeV/u	30 nb [135]
^{252}No	^{206}Pb(^{48}Ca,2n)^{252}No	4.55 MeV/u	400 nb [136]
^{253}No	^{207}Pb(^{48}Ca,2n)^{253}No	4.55 MeV/u	1000 nb [136]
^{254}No	^{208}Pb(^{48}Ca,2n)^{254}No	4.55 MeV/u	1800 nb [136]
^{255}Lr	^{209}Bi(^{48}Ca,2n)^{255}Lr	4.56 MeV/u	437 nb [137]

Table 4.1.: Fusion-evaporation reactions and corresponding cross sections for a direct production of isotopes studied in the framework of the laser spectroscopy program at the separator SHIP. Given are the projectile energies which are typically requested for the primary beam from the UNILAC accelerator at GSI to maximize the production yields.

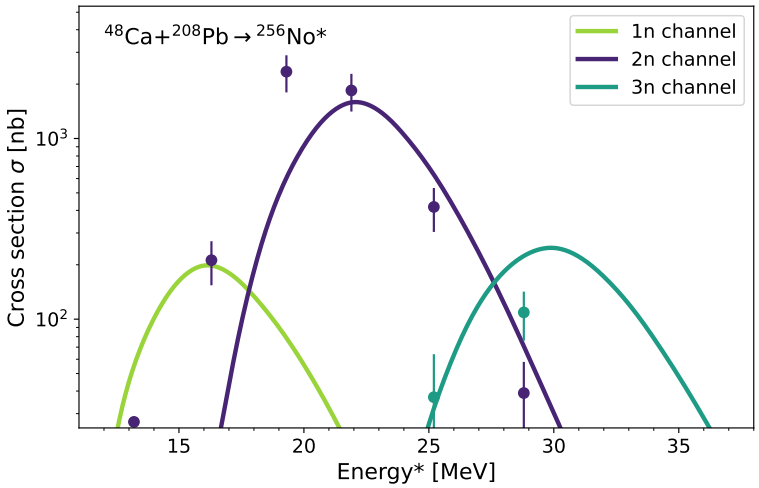

Figure 4.3.: Excitation function of the ^{208}Pb(^{48}Ca,xn)$^{256-x}$No fusion-evaporation reaction. Shown are cross sections for different neutron-evaporation channels as a function of the excitation energy E^* of the compound nucleus. The solid curves show calculations performed with the statistical HIVAP code [132][138]. The data points represent cross section measurements performed at SHIP [137].

A direct production of fermium isotopes with a ^{48}Ca beam was previously demonstrated using ^{202}Hg and ^{204}Hg targets (mercury, $Z = 80$) to access ^{248,250}Fm via the two-neutron evaporation channel for in-beam gamma ray spectroscopy studies [139]. Cross sections of 120 nb and 2 µb were determined in these measurements, respectively [112]. In a similar experiment, a cross section of 1 µb was determined for ^{250}Fm using the same reaction with a slightly higher energy [113]. However, the maximum beam intensity for irradiation of the target is restricted due to the low melting point of mercury, and handling these targets necessitates highest precaution. The neutron-deficient isotopes ^{245,246}Fm can instead be reached via the reactions ^{208}Pb(^{40}Ar,2/3n)$^{245/246}$Fm

and low cross sections of few tens of nb [134] as given in Tab. 4.1. Similarly, ^{244}Fm can be produced by evaporation of four neutrons or via the reaction ^{207}Pb(^{40}Ar,3n)^{244}Fm, however both featuring an even one order of magnitude smaller cross section of 1.7 nb and 3.6 nb, respectively [140]. Similarly, via the 3n-channel, the production of ^{243}Fm was shown [141]. In a more asymmetric reaction, the scheme ^{239}Pu(^{12}C,4n)^{247}Fm can offer the production of the latter isotope with about 0.2 µb [142]. To reach more neutron-rich isotopes, transfer reactions based on bombardment of ^{248}Cm targets with ^{44}Ca projectiles showed the production of isotopes $^{252-256}$Fm with maximum production cross sections ranging from 20.9 µb to 0.34 µb depending on the initial bombardment energy [143].

All on-line produced fermium isotopes investigated in this work were produced at the GSI facility with stable beams of intensities up to 1-2 particle µA, depending on the beam[1], and accelerated by the Universal Linear Accelerator (UNILAC). Isotopically enriched foils of the respective target material were mounted on a rotating target wheel which is synchronized with the beam pulses from the accelerator. The damages by high-intensity beam bombardment on the thin target can therefore be distributed over several target segments to prolong the lifetime of the target. Only the isotopes ^{245,246}Fm were directly produced with ^{40}Ar^{8+} beam with average intensities of 2 particle µA corresponding to $1.2 \cdot 10^{13}$ particles per second. Considering a target areal thickness of about 0.5 mg/cm^2, corresponding to 1.4^{18} atoms/cm^2 for ^{208}Pb, and the respective cross section of 15 nb for ^{246}Fm given in Tab. 4.1, only one nucleus every 4 s is produced of this isotope. As the product nuclei proceed in the direction of the intense primary beam, due to momentum conservation, a separation of both species is required.

4.1.3. Velocity filter SHIP

For the study of product nuclei from heavy ion fusion-evaporation reactions, separators are used to filter the product particles from the intense primary beam. Due to momentum conservation, projectiles and the compound nucleus move in the same direction after the reaction. For separation, various types of separators are used to access reaction products. The most common two separator types are gas-filled separators and vacuum separators [20, 78]. The velocity filter Separator for Heavy Ion reaction Products (SHIP) at the GSI is a recoil separator of the latter type [144]. The on-line experiments described in this thesis were performed at the focal plane of SHIP in different on-line experimental campaigns.

SHIP allows for an in-flight separation of reaction products from the primary beam via the differing velocities of both. It mainly consists of a combination of dipole magnets and electrostatic deflectors in connection with quadrupole lenses for focusing. The arrangement of electric and magnetic fields follows the principle of a simple Wien-

[1] Average beam intensities of up to 0.7 particle µA are routinely delivered for ^{48}Ca^{10+} beam corresponding to about $4.4 \cdot 10^{12}$ particles per second.

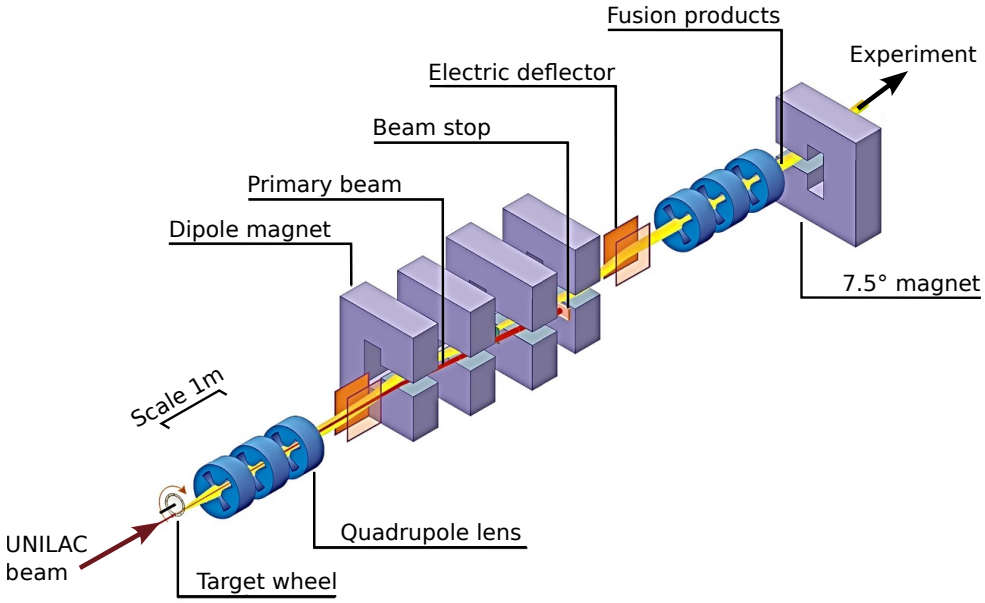

Figure 4.4.: Layout of the SHIP separator for heavy fusion evaporation products at GSI. Figure adapted from [145].

filter, where both fields are superimposed in a crossed geometry and penetrating ions are forced in opposite directions. The field strengths can be arranged such that the Lorentz force resulting from the magnetic field cancels out for a certain velocity v which is consequently transmitted [2]. Both fields are tuned following

$$\overrightarrow{F}_{\text{Lorentz}} = q \cdot (\overrightarrow{v} \times \overrightarrow{B} + \overrightarrow{E}) \stackrel{!}{=} 0 \quad \Leftrightarrow \quad v = \frac{E}{B}, \tag{4.3}$$

where B and E are the magnetic and electric field strengths and q the electric charge of the transmitted ions. For every velocity v, an arrangement of E/B can be found for which the Lorentz force cancels and SHIP transmits the respective species. From Eq. 4.3, it can also be shown that the separation is independent of the charge state q of the product nuclei. When SHIP is tuned to transmit fusion products of a known mass and kinetic energy, the primary beam projectiles, with a different velocity as the reaction products, will experience a remaining force and thus a deflection towards a beam dump. After the velocity filter, a subsequent 7.5°-deflecting dipole magnet enables further background reduction of scattered remaining projectiles [2]. The transmission through SHIP for the reaction of ^{208}Pb(^{48}Ca,2n)^{254}No can be estimated with about 30 % [146].

After passing the velocity filter, the fast recoil nuclei with tens of MeV kinetic energy, as described before in Sec. 4.1.2, are directed further towards the subsequent experimental setup for dedicated studies. For some of these studies, a deceleration of the fusion products is required, as in the case of the mass measurement program as well as

for the laser spectroscopy program at SHIP, to allow for a confinement and further manipulation of the nuclei of interest. For this purpose, buffer gas-filed stopping cells are applied.

4.2. Buffer gas-filled stopping cells

The application of buffer gas-filled stopping cells or gas catchers, respectively, allows for the efficient deceleration of highly energetic recoil nuclei to thermal energies within a compact stopping volume. With the combination of different degrader foils, the deceleration of recoil ions prior to the gas cell can be adapted. A thin entrance window of few µm thickness or less, used to separate the gas cell from the vacuum side, additionally acts as a degrader foil and contributes to the deceleration of incoming reaction products.

Through collisions with the buffer gas atoms in the gas cell, the recoil ions gradually reduce their kinetic energy in a step-wise manner while the charge state is continuously reset via charge exchange processes [147]. To avoid chemical reactions between the buffer gas atoms and the charged recoil ions, high purity inert buffer gases are used, such as helium or argon. The stopping power depends on the buffer gas species, for example, collisions with heavier argon gas atoms result in a faster energy loss compared to collisions with much lighter helium atoms. In addition, the final charge state is affected by the choice of the buffer, gas as it depends on the ionization potential of the gas species.

To date, the gas catcher technique is applied in many different on-line facilities for RIB experiments. The first implementation of this technique was at the IGISOL facility in Jyväskylä, Finland [148], where it is still used for studies of exotic radioactive isotopes produced in different nuclear reactions. Further development of the technique lead to the implementation of gas catchers for high-energy fragments from nuclear reaction studies at facilities such as at the RIKEN projectile fragment separator (RIPS) [149] and the GSI FRagment Separator (FRS) [150]. At the CARIBU facility, a gas catcher is used to stop fission products from a strong ^{252}Cf source [151]. For the high-precision mass measurements at SHIP with the Penning-trap setup SHIPTRAP, efficient recoil stopping is achieved with a cryogenic gas-stopping cell [152].

The RADRIS technique applied for laser spectroscopy studies in this work combines the resonance ionization spectroscopy technique with a buffer-gas cell for experimental studies tailored to the application at SHIP. In this apparatus, the deceleration of recoil ions, further manipulation, and final investigation are performed in the same gas cell. In the following section, a comprehensive description of the laser spectroscopy technique RADRIS and the previous state of the setup as it was applied in beamtime campaigns until 2020, including measurements on ^{248,249,250}Fm, is provided.

4.3. Laser spectroscopy studies at SHIP

Laser spectroscopy studies of the heaviest actinides pose specific challenges in terms of lowest production yields of only few nuclei per second or less and short half-lives of the species of interest [20]. Under these experimental conditions, commonly applied techniques are not suitable for the study of these exotic nuclei. The Radiation Detected Resonance Ionization Spectroscopy (RADRIS) method was specifically tailored to study short-lived heavy actinide fusion-evaporation products at the SHIP separator at GSI by means of laser spectroscopy [153, 133]. The method was based on the successful study of the fission isomers $^{240f,\ 242f,\ 244f}$Am (americium, $Z = 95$) [154]. A recent major milestone was the study of the heavy actinide element nobelium ($Z = 102$), to date the heaviest element investigated by laser spectroscopy. With the RADRIS technique, several atomic levels and the ionization potential were determined precisely for the first time [27, 155]. The success of this study set the foundation for further measurements of different nobelium isotopes and other heavy actinide elements.

4.3.1. RADRIS principle

The experimental setup of RADRIS mainly consists of an argon buffer-gas filled stopping cell situated after the velocity filter SHIP [153, 133]. A schematic presentation of the RADRIS principle is shown in Fig. 4.5. Fusion-evaporation products transmitted by SHIP enter the gas cell through a thin entrance window of typically 3.5 µm thin aluminum-coated mylar foil positioned on a stainless steel support grid. For moderation of the recoil energy loss before entering the gas cell, different combinations of mylar-degrader foils can be added in front of the entrance window. The gas cell itself is filled with 90-95 mbar high-purity argon buffer gas (99.9999 %) which allows thermalizing and stopping incoming reaction products in a short distance. For ^{254}No product nuclei, with an additional 1.5 µm mylar-degrader foil, recoil stopping is achieved after passing through a length of 6 cm into the gas cell. For much lighter ^{155}Yb products for example, with a kinetic energy of 67.6 MeV, a length of 9.3 cm until recoil stopping is required [156].

A hafnium-strip filament of 1 mm width and 25 µm thickness placed opposite to the entrance window is biased with an attractive potential to accumulate the thermalized recoil ions, which remain positively charged . On the filament surface, the ions adsorb and neutralize. By resistive pulse heating the filament, collected neutral atoms are re-evaporated from the filament surface to form an atomic cloud around the latter.

Following the desorption from the filament surface, the resulting atom cloud is illuminated by two or more laser beams with enlarged spot sizes, each approximately 2 cm in diameter, constituting the applied RIS scheme. Ions emerging from resonant laser ionization are guided with suitable electric fields towards the detection region equipped with a Passivated Implanted Planar Silicon (PIPS) detector. This detector type allows for registration and an unambiguous identification of the recoil ions by their characteristic alpha-decay energy. Laser-induced events of the nuclei of interest

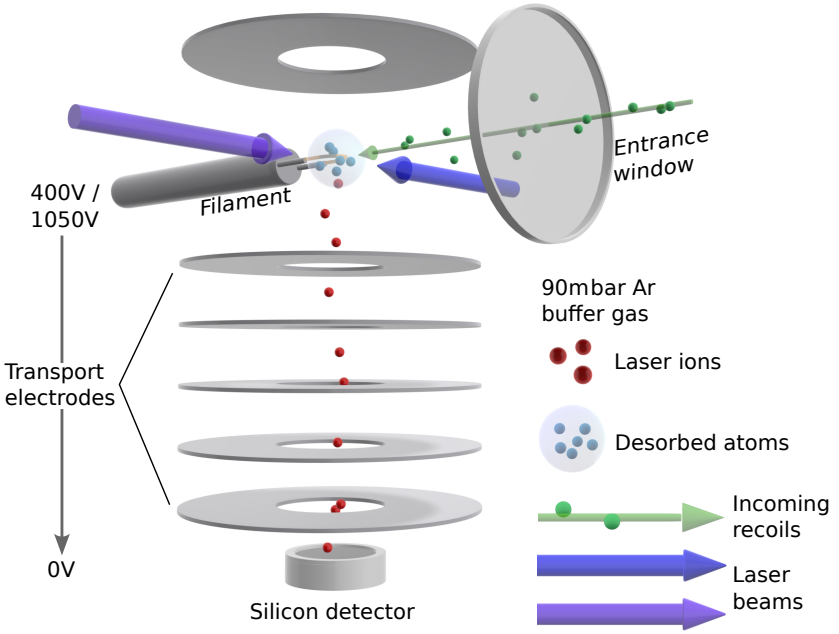

Figure 4.5.: Schematic illustration of the RADRIS principle. The argon buffer gas allows thermalizing incoming fusion-evaporation reaction products. The catcher filament, located opposite the entrance window, serves to attract thermalized recoil ions onto its surface where they adsorb and neutralize. After desorption from the filament, two laser beams following a two-step RIS scheme illuminate the created cloud of neutral atoms. Resulting ions are guided via transport electrodes towards a silicon detector for unambiguous identification via the characteristic alpha-decay energy.

can thus be discriminated from background contributions and subsequent decaying daughter nuclei. A 200 nm-thin aluminized Kapton foil is implemented in front of the detector, shielding it from scattered light of the high-intensity laser pulses and the filament heat-pulse creating significant amounts of background events.

4.3.2. Laser system

For RIS measurements with RADRIS, multiple laser systems are available, as shown in Fig. 4.6, to allow for a fast swap of RIS-schemes or a synchronous operation of multiple systems during level-search campaigns. A detailed description of the individual components can be found in [157]. In total, four tunable dye-laser systems are available which are pumped by high power excimer lasers and a Nd:YAG laser with third-harmonic generation output (355 nm), respectively. Depending on the gas mixture used for operation of the excimer lasers, different output wavelengths can be generated, such as 351 nm for Xe:F and 308 nm for Xe:Cl. With the optimal combination of pump laser and suitable dye, laser light from the visible range around 20 000 cm^{-1} or 500 nm to the deep Ultraviolet (UV) range around 30 000 cm^{-1} or 333 nm can be produced. With this setup, even the recently identified ground-state transition in nobelium at 334 nm

[27] can be reached without frequency-doubling. All pump-laser systems are operated at 100 Hz repetition rate for the in-gas cell laser spectroscopy. Pulse energies of 500 µJ or more, depending on the pump beam and the used dye, can be delivered by the lasers with a pulse width of about 18 ns. The dye lasers 1-3 in Fig. 4.6 can be operated in broad band configuration with a linewidth of about 6 GHz. With an additional intra-cavity etalon for narrow-band operation, the bandwidth can be reduced down to 1.2 GHz.

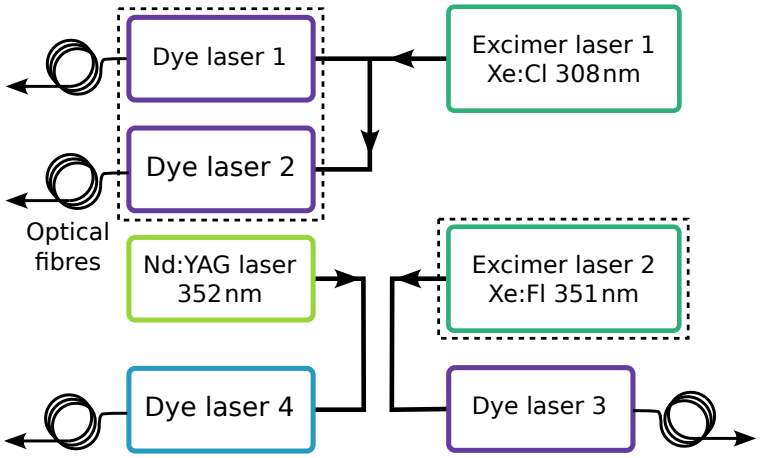

Figure 4.6.: Schematic diagram of the available laser systems in the laboratory at GSI. The laser systems applied for experiments on fermium and nobelium discussed here are marked with dashed boxes.

The dye-laser beams are transported via multi-mode optical fibers to the experimental setup providing the FES in the applied RIS scheme. The Xe:F excimer laser beam, often used as second, non-resonant ionization step, is transported via mirror optics to the experiment. After transport, pulse energies of typically about 30 mJ are available at the experiment for ionization. As an alternative, a second Nd:YAG laser with second and third harmonic generation units (532 nm/355 nm) is available, located in the vicinity of the experimental setup, for supplying the non-resonant ionization step. To ensure an optimum timing between the different steps in the RIS scheme, a pulse generator is employed as an external trigger for the individual pump lasers and the timing overlap is continuously monitored with photodiodes located at the experimental setup. For the excimer lasers, active synchronization units are additionally used to stabilize the timing of the lasing output using a feedback signal from a fast photodiode.

Finally, the laser wavelengths of all applied dye lasers are continuously recorded using a wavelength meter (HighFinesse WS7) with an optical fiber switch.

4.3.3. Filament desorption

The efficiency of the RADRIS technique crucially depends on a complete desorption of collected recoil nuclei from the filament surface. The required desorption temperature

is element specific and depends on the desorption enthalpy of the species of interest from the respective material. Within the filament heat-pulse duration, the minimum temperature for a full desorption has to be reached, a more increased temperature can additionally serve for a shortened desorption time. However, elevated temperatures can significantly decrease the filament lifetime, especially during extended measurement periods with a continuous succession of RADRIS cycles, such that a more frequent replacement is necessary. In addition, non-resonant background contributions from surface ionization effects may arise and hamper the sensitivity of the technique up to the point that laser-induced ions cannot be differentiated anymore from surface ions.

The creation of surface ions, similar as the desorption itself, strongly depends on the element under investigation and the filament material. The emerging rate of surface ions n_+ relative to the number of released neutral atoms n_0 is described by the Saha-Langmuir equation as

$$\frac{n_+}{n_0} = \frac{g_+}{g_0} \cdot e^{-\frac{E_{\mathrm{IP}}-\phi}{k_{\mathrm{B}}T}}, \tag{4.4}$$

where g_+, g_0 are the degeneracies of the ionic and atomic states, respectively, E_{IP} is the ionization potential of the studied element of interest, ϕ is the work function of the filament material, k_{B} denotes the Boltzman constant and T the filament temperature [158]. From this relation it can be concluded that a reduced work function in comparison to the respective ionization potential is beneficial to minimize the surface ion contributions.

The identification of the optimum filament configuration and temperature has to be ensured before a study with the RADRIS technique is possible. In the case of nobelium isotopes, a tantalum-wire filament of 125 µm thickness was applied. For an efficient desorption, a maximum heat pulse of 500 ms length and a temperature of only 1100 °C was required due to the low desorption enthalpy of 250 kJ/mol [159]. In addition, the low desorption temperature in combination with the ionization potential of about 6.33 eV [155] and the tantalum work function of 4.22 eV [160] gave rise to a negligible surface ion background during the measurements on nobelium.

Studies of other elements with RADRIS such as the heaviest actinide element, lawrencium, however require an adaption of the filament material and geometry. Calculations predict a desorption enthalpy of lawrencium from tantalum of 600 kJ/mol [161], which is significantly higher than for nobelium. Therefore, higher desorption temperatures are required. The first ionization potential of lawrencium, on the other hand, was recently determined to be 4.96 eV [162] and thus lower than the one of nobelium. Therefore, an elevated surface ionization contribution has to be expected. In recent investigations, the desorption behavior of the homologue element lutetium was studied for different filament types to identify the optimum filament material for studies in lawrencium. The previously used tantalum filament showed strongly enhanced surface ion contributions and a mechanical instability at the required desorption temperature.

It was therefore found unsuitable for an successful investigation of lawrencium with RADRIS [163]. These experimental challenges can be overcome by using a hafnium-strip filament as introduced before in Sec. 4.3.1. This filament type ensures a higher longevity, as a lower temperature for desorption is sufficient compared to tantalum, along with minimal surface ionization. Using a filament strip instead of a thin wire guarantees a more mechanically stable geometry. The hafnium-strip filament was successfully employed for studies also on nobelium and for the on-line campaigns on fermium described in this work. For the successful desorption of fermium, heat-pulses of about 1450 °C were required, while surface ion contributions remained negligible due to the higher ionization potential of about 6.52 eV [162].

4.3.4. RADRIS cycle concept

The RADRIS technique is based on a cyclic application of the measurement scheme. An example of such a standard cycle as applied for laser spectroscopy of ^{155}Yb ($t_{1/2}$ =1.8 s) is visualized in Fig. 4.7. Each cycle is divided into filament accumulation mode of stopped recoil ions, and subsequent ionization and guiding mode to the detector. During the accumulation mode, the pulsed primary beam from the UNILAC[2] is continuously requested for a persistent production of recoil nuclei. After entering the gas cell, the thermalized reaction products are guided towards the filament by applying an attractive potential relative to the surrounding gas cell chamber itself and the electrodes enclosing the stopping volume [133, 164]. With completion of the accumulation, the primary beam request is stopped, the laser shutters are opened to illuminate the volume around the filament and the setup is switched to ionization/guiding mode. For this, the filament is biased to be on the most repellent potential within the apparatus, while the voltages on the surrounding electrodes are adjusted to create an attractive gradient, directing the emerging ions towards the silicon detector at ground potential. To complete the change between the two modes, the electrostatic potentials applied to the filament, the first surrounding transport electrodes and the experimental chamber itself are switched by providing an analogue trigger signal to the respective power supplies. The respective potentials on the individual electrodes for both modes are summarized in Tab. 4.2 and a technical drawing including the transport electrodes to be switched is shown in Fig. 4.8.

Once the switch of modes is completed, the filament heat-pulse is triggered for desorption of collected fusion products and both the laser resonance ionization and the transport of ions to the detector enabled. For initialization of the setup for the next cycle, the electrostatic potentials are switched back to accumulation mode, the laser shutters are closed and the primary beam is requested again.

The efficiency of the cycle itself is dependent on the half-life of the studied species

[2]The total beam from the UNILAC is constituted of pulses with 50 Hz repetition rate. For the experiments using "main" beam described in this work, about 40-45 Hz corresponding to 80-90 % of the UNILAC pulses were made available. In case of "parasitic" beam usage, commonly a repetition rate between 5-10 Hz corresponding to 10-20 % of all pulses is available for experiments.

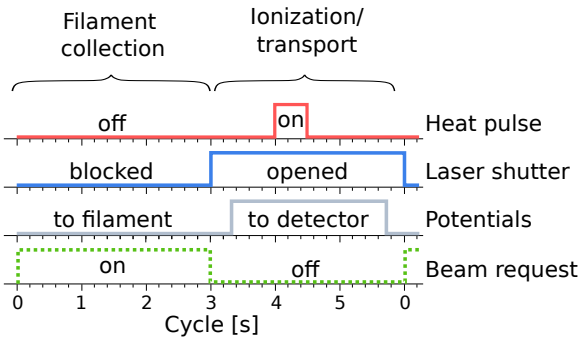

Figure 4.7.: Standard RADRIS cycle applied for laser spectroscopy measurements of ^{155}Yb. The collection time depends on the half-life of the studied species, whereas the beam-off period is independent from it and remains the same for different isotopes. Figure adapted from [164].

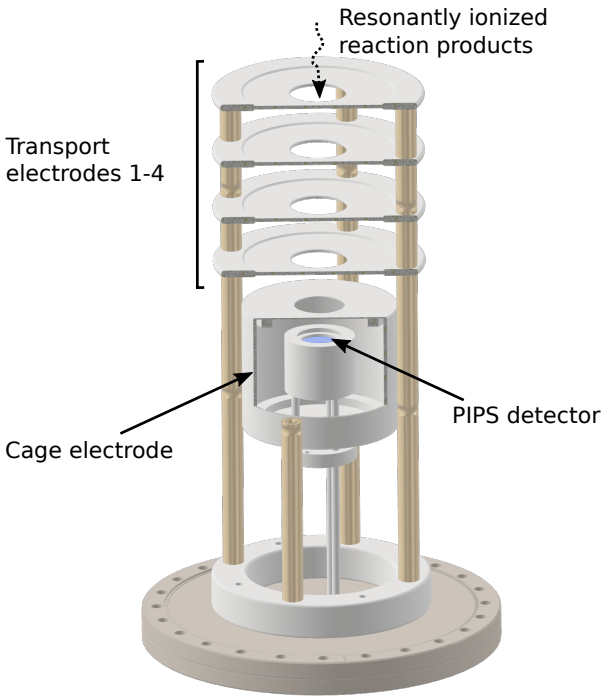

Figure 4.8.: Technical drawing of the RADRIS detector setup as used until the on-line beamtime campaign in 2020. With this setup, the first laser spectroscopy of the heavy actinide element nobelium became feasible [27].

$t_{1/2}$, the beam-on-target time $t_{\text{beam on}}$, the beam-off time $t_{\text{beam off}}$, as was previously described in [159]. An additional efficiency loss due to decay losses within a delay time t_{delay} between the stop of the filament accumulation and the final detection has to be taken into account. The cycle efficiency therefore follows the relation

Electrode	Accumulation [V]	Transport [V]
Filament	300	1015
Cross Piece	746	1025
Lower electrode	746	1025
Electrode 1	749	1000
Electrode 2	800	800
Electrode 3	605	605
Electrode 4	580	580
Cage	245	245
Detector	0	0

Table 4.2.: Potentials applied in the RADRIS setup prior to developments made within this work. The settings for filament accumulation and ionization/guiding mode potentials with partly required potential switching are included. The potential of the experimental chamber itself is switched, here called the cross piece.

$$\epsilon_{\text{Cycle}} = \frac{t_{1/2}}{(t_{\text{beam on}} + t_{\text{beam off}}) \cdot \ln(2)} \left[1 - e^{\frac{-\ln(2)}{t_{1/2}} \cdot t_{\text{beam on}}}\right] \cdot e^{\frac{-\ln(2)}{t_{1/2}} \cdot t_{\text{delay}}}. \tag{4.5}$$

Within this description, half-life dependent decay losses during the cycles and the overall duty cycle in terms of UNILAC beamtime usage are considered. For an optimum duty cycle, the beam-off period, which is independent of the studied isotope and half-life, should be kept as short as possible. To maximize the cycle efficiency for a specific isotope, the beam-on period has to be optimized for the given half-life. However, the usually short half-lives of studied species, especially those with half-lives $t_{1/2} < 1\,\text{s}$, limit the total efficiency of the cyclic RADRIS method due to substantial decay losses in the time t_{delay}, posing challenges for experimental studies.

In the technical implementation of the RADRIS cycles, limitations arise due to the time-consuming switching between filament accumulation and guiding mode, resulting in additional delays and, consequently, decay losses in the beam-off period. Before the filament potential can be switched, a complete stop of the primary beam has to be ensured to avoid a direct transport of incoming, positively charged fusion-evaporation products to the detector. These are unrelated to any laser interaction and would contribute to background signals. Therefore, a delay of 0.3 s between the beam stop and the trigger signal for potential switching was included in the cycle. In a similar manner, an additional delay of 0.7 s between the potential switching and the desorption heat-pulse was included to allow the potentials to reach their setpoint before the maximum temperature is reached. Here, about 0.2 ms from the trigger signal are required for the supplies to reach the potential. These limitations can be seen in the extended beam-off period of 3 s in a standard RADRIS cycle shown in Fig. 4.7 with an equally long beam-on-target period. A more detailed description can be found in Ref. [164].

The technical limitations and physical limitation of half-live dependent decay losses were further investigated as described in the following chapter 5. Developments towards a reduction of the required beam-off period were performed along with further advances of the RADRIS detection setup to enable more efficient measurements of shorter-lived ($t_{1/2} < 1\,\mathrm{s}$) and longer-lived ($t_{1/2} > 1\,\mathrm{h}$) isotopes. The cyclic application of RADRIS additionally opens up opportunities for new indirect production schemes, providing access to isotopes that were previously inaccessible for a direct production.

4.3.5. Indirect production schemes for fermium isotopes

For laser spectroscopy studies at SHIP employing (cold) fusion-evaporation reactions for production, the respective isotopes have to exhibit a production cross section of at least few tens of nb to perform an experiment with sufficient statistics. With respect to direct production schemes, only ^{245,246}Fm with a suitable target-beam combination were in reach for laser spectroscopy with RADRIS.

For the investigation of some more fermium isotopes with RADRIS, the cyclic measurement approach allows for schemes of an indirect production. Nobelium mother isotopes, produced in direct fusion-evaporation reactions with relatively high cross sections as described in Sec. 4.1, are collected on the filament as they undergo alpha-decay, transforming into their respective fermium decay daughter. The accumulation time can be arranged such that the nobelium nuclei are collected with a sufficiently long waiting time between stop of the primary beam and filament-pulse heating to await their decay. Approximately half of the positively charged fermium recoil nuclei will be emitted into the surrounding buffer-gas atmosphere, in which they again thermalize and be re-attracted to the filament. The other half will be implanted deeper into the material and partially captured. The subsequent pulse-heating allows desorption of accumulated daughter recoil nuclei from the surface [165]. Similarly, other decay paths for an indirect productions can be used, such as the electron capture branch for example in ^{255}Lr to access ^{255}No [164].

In this context, the element-specific desorption can be advantageous, as it may selectively inhibit the desorption of other species, such as remaining mother nuclei, depending on their respective desorption enthalpies. This is beneficial for an indirect production scheme for ^{255}No, as lower desorption temperatures are required compared to the lawrencium mother. For an indirect production of fermium on the other hand, no beneficial effect is gained as filament heat-pulses of around 1100 °C were sufficient to desorb the nobelium mother, while 1450 °C heat-pulses were applied for fermium.

The alpha branching of the isotope of interest and the respective decay branch of the mother isotope are both decisive for the overall efficiency. In addition, the efficiency of the cycle is not only dependent on the half-life of the investigated species as described in Eq. 4.5, but additionally on the half-life of the mother. Therefore, the filament accumulation and decay waiting time before the heat pulse have to be tailored for each combination of mother-daughter nuclei production scheme.

The new indirect production scheme was initially tested in a proof-of-principle experiment on ^{250}Fm via the decay of the ^{254}No mother. This first measurement was previously described in greater detail in Ref. [165] and in the PhD thesis of E. Rickert [166]. With the indirect production method, even more fermium isotopes came in reach as summarized with their respective production schemes in chapter 6 in Tab. 6.1 and visualized in the nuclear chart cut-out in Fig. 6.1. These isotopes include those with mass numbers 248, 249, 250 and 254, which were otherwise inaccessible for laser spectroscopy with RADRIS.

5. Advancing the RADRIS method

The current RADRIS setup and the implemented cycle impose limitations to the isotopes which can be studied using this method. To address these limitations and enhance the sensitivity and efficiency of the technique for accessing more exotic isotopes, efforts were directed towards upgrading the detection system and developing a more efficient cycle. The new advancements introduced in the framework of this work are discussed in the following.

5.1. Enhancing the overall RADRIS efficiency

The overall efficiency of the RADRIS method for a specific radio-isotope can be defined as the ratio of the number of registered alpha events from ions generated through RIS on the RADRIS detector to the rate of recoil ions in the focal plane of SHIP, therefore [133]

$$\epsilon_{\text{RADRIS}} = \frac{N_{\alpha,\text{detector}}}{N_{\text{ions, SHIP}}}. \tag{5.1}$$

The rate of incoming ions can be determined using a 16-strip silicon detector positioned at the focal plane ahead of the experimental setup. The efficiency of the gas cell and the method itself can furthermore be divided into partial efficiencies contributing to the overall RADRIS performance following

$$\begin{aligned}\epsilon_{\text{RADRIS}} =& \epsilon_{\text{incoming}} \times \epsilon_{\text{stopping}} \times \epsilon_{\text{filament collect}} \times (1 - \epsilon_{\text{neutralization}}) \\ & \times \epsilon_{\text{evaporation}} \times \epsilon_{\text{RIS}} \times \epsilon_{\text{cycle decay}} \times \epsilon_{\text{transport}} \times \epsilon_{\alpha\text{-branch}} \times \epsilon_{\text{detection}}.\end{aligned} \tag{5.2}$$

Considered are the efficiency for recoil ions to enter the gas cell through the entrance window, the stopping efficiency in the buffer gas, the transport efficiency of the thermalized ions to be collected on the filament, losses due to neutralization in the gas cell, and the efficiency of the filament evaporation. Additionally included are the efficiency of resonant laser ionization, the cycle efficiency dependent on the half-life of the studies species (the duty cycle of overall beamtime usage as defined in Eq. 4.5) is neglected here), the transport efficiency through the electrode structure, the alpha-decay branch of the respective isotope, and the detection efficiency of the silicon detector, primar-

Partial efficiency	^{254}No [%]
$\epsilon_{\text{incoming}}$	76
$\epsilon_{\text{stopping}}$	100
$\epsilon_{\text{filament collect}}$	88
$(1 - \epsilon_{\text{neutralization}})$	93
$\epsilon_{\text{evaporation}}$ ϵ_{RIS}	36
$\epsilon_{\text{cycle decay}}$	85
$\epsilon_{\alpha\text{-branch}}$	90
$\epsilon_{\text{detection}}$	40
$\epsilon_{\text{combined}}$	6.9

Table 5.1.: Partial efficiencies to be considered for the overall performance of the RADRIS technique for ^{254}No. Values taken from Ref. [133]. Here, for the RADRIS efficiency, the cycle efficiency ϵ_{cycle} is included in terms of half-life losses. The duty cycle considering beamtime usage is not included in the considerations.

ily determined by its solid angle coverage. The known partial efficiencies previously calculated or determined in Ref. [133] are presented in Tab. 5.1.

The overall RADRIS efficiency was previously established to be 6.4(10) % for ^{254}No and 3.3(10) % for ^{252}No [27]. In this case, the efficiency for the shorter-lived ^{252}No ($t_{1/2} = 2.46\,\text{s}$) was found to decrease by a factor of two, primarily due to the reduced cycle efficiency ϵ_{cycle} considering decay losses.

Advancing the overall RADRIS efficiency is consequently based on the enhancement of the partial efficiencies. In the framework of this work, development efforts have been carried out with a focus on the optimization of the cycle efficiency ϵ_{cycle}, particularly for short-lived reaction products, and the improvement of the transport efficiency $\epsilon_{\text{transport}}$. In addition, an enhancement in the solid angle coverage and therefore an increased $\epsilon_{\text{detection}}$ was addressed.

5.2. Improving the RADRIS cycle

With the introduced RADRIS cycle scheme previously used for studies of shorter-lived species such as ^{155}Yb ($t_{1/2} = 1.8\,\text{s}$), decay losses dominantly limit the overall efficiency. Beginning with the beam-off period, the accumulated fraction of fusion-evaporation products on the filament starts to decay until laser-induced ions reach the detector. The time span between the stop of the beam and the ion arrival on the detector not only comprises the two delays due to the technical limitations described before. In addition, the transport time of the ions drifting through the gas cell needs to be considered, yet it was not measured before. Altogether, the overall delay up to a registration of ions on the detector is significant, particularly for isotopes with half-lives as short as $t_{1/2} < 1\,\text{s}$, which prevented their study with the RADRIS technique so far.

To extend the range of nuclides accessible with the technique, a new short-cycle was developed and characterized in an on-line experimental campaign on short-lived ^{154}Yb with a half-life of $t_{1/2} = 0.4\,\mathrm{s}$. The optimized short-cycle scheme is shown in Fig. 5.1, where the beam-off period is significantly reduced compared to the old cycle scheme in Fig. 4.7. The isotope ^{154}Yb was suitable for this study as it can be produced with relatively high cross sections compared to heavy actinide isotopes in the fusion-evaporation reaction of ^{112}Sn(^{48}Ca,6n)^{154}Yb at SHIP. To enhance the overall efficiency by shortening the beam-off period, the delay between the stop of the primary beam and the potential switching was reduced to 0.2 s, as this showed to be sufficient to avoid a direct transport of incoming reaction products to the detector. The remaining delay additionally ensures a completed accumulation of the last incoming ions before the switch.

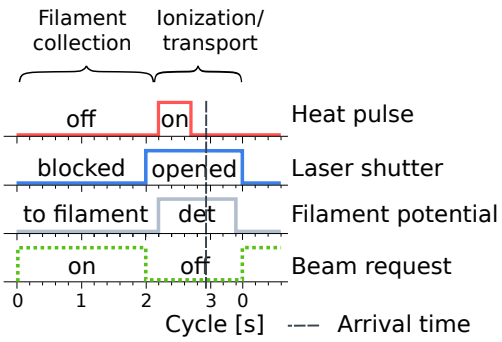

Figure 5.1.: Improved RADRIS cycle adjusted for laser spectroscopy measurements of ^{155}Yb with shorter beam-off period. The arrival time of the ions after the stop of the beam request is marked with the gray dashed line. The delayed arrival is due to the delayed heat-pulse after the beam stop to ensure a switching to transport mode before desorption, and the required ion transport time due to the physical limitation of the ion mobility in the gas cell. Figure adapted from [164].

For a faster potential switching itself between filament accumulation and transport mode, a new setting of switching only the filament potential without adjusting other electrodes was investigated. Here, the surrounding transport electrodes and the experimental chamber (referred to as the cross piece) were kept on a constant potential. A fast high-voltage switch (model Behlke GTHS) was employed to swap between the low attractive and the high repellent potential on the filament supplied by two individual voltage supplies. This allowed a complete switch between both modes in a few milliseconds, about two orders of magnitude faster compared to the switching of the single supply used before. In addition, the heat-pulse trigger was set earlier to follow the potential switching trigger. As the maximum temperature is only reached towards the end of the 500 ms long heat-pulse, the faster filament potential switch is already concluded at the time of desorption.

Physical limitations on the minimum cycle time, resulting from the drift time of ions in the gas cell itself, were investigated. Here, the minimum waiting time after desorption,

which is required for the ions to reach the detector before initializing the setup for the next cycle, was determined. For this test, beam pulses of 1 Hz repetition rate and a pulse length of 5 ms were requested from the UNILAC for the creation of ^{154}Yb nuclei. The reaction products entering the gas cell were guided directly towards the detector, bypassing the filament. The estimated time of flight from this procedure for a direct transport was considered as an upper limit of the desorbed, laser created ions flying a similar distance through the gas cell. The measured time structure of the respective time-binned alpha events in dependence of time after the beam-request trigger is shown in Fig. 5.2.

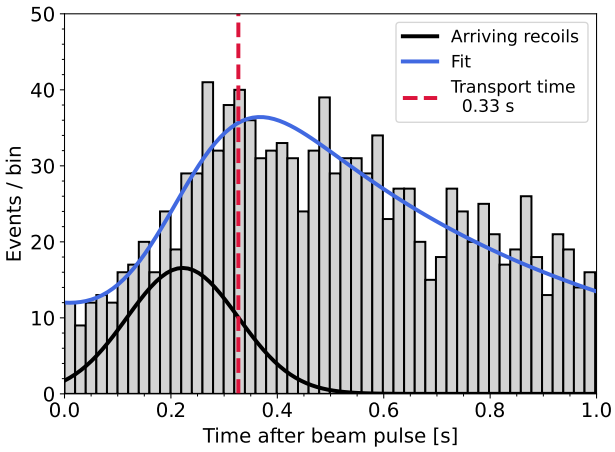

Figure 5.2.: Decay-time structure of incoming ^{154}Yb product nuclei directly transported to the detector. The recoil nuclei were produced by single primary beam pulses from the UNILAC, each with a pulse length of 5 ms and 1 Hz repetition rate, enabling the tracking of the arrival time structure. The time structure of the incoming ions moving in the gas cell was modeled with a Gaussian distribution shown in black. The arrival time required for 84.13 % of the ions to reach the detector is determined via a fit to the time structure, here marked in red. More details can be found in the text. Figure adapted from [164].

Besides a delayed arrival of ions on the detector, due to the limited mobility, an increased stopping distribution of the ions and diffusion processes in the gas cell lead to an enhanced width which can be observed in the arrival time distribution. The rate of arriving ions after the beam pulse can be described by the differential equation

$$\frac{dN_{\text{ions}}}{dt} = A \cdot e^{\frac{-(t-t_c)^2}{(2 \cdot w^2)}} - \lambda \cdot N_{\text{ions}}, \tag{5.3}$$

where N_{ions} is the number of ions, t is the time after the beam trigger, A is the amplitude, t_c the centre and w the width of the time distribution of incoming ions. For simplicity, a Gaussian time distribution of the ions moving in the gas cell was assumed. With the latter part and the decay constant $\lambda = \frac{\ln(2)}{t_{1/2}}$, decay losses are thus considered in the calculation. A fit of this function to the observed time structure in

the detector ultimately allowed quantifying the arrival time. The latter is determined as the time required for 84.13 % of the ions to reach the detector, which corresponds to the time t_c plus $1w$. From the fit, an arrival time of 0.33 s for ^{154}Yb was derived, which can be assumed to be similar for other considered species under the same experimental conditions in RADRIS with 90 mbar argon buffer gas and a potential gradient of about 29 V/cm. For the optimization of the cycle, decay losses due to the limited transport time had to be considered. A faster ion transport with a larger voltage gradient through the cell would allow shortening this delay time. However, in the current setup under the applied buffer-gas pressure, steeper gradients, starting from the filament at 1050 V, are not applicable as this would create discharges.

Combining all considered delays, a total delay time of 0.93 s between the stop of the primary beam and the arrival of resonantly laser ionized reaction products is expected for the new short cycle. Respective decay losses within this time interval ultimately determine the limit for isotopes with short half-lives to be studied with RADRIS.

In summary, the short-cycle was established with a total beam-off period of 1.5 s and therefore reduced by half in comparison to the previous cycle. This allows for a more efficient usage of given beamtime. In addition, the ion arrival delay was shortened by a factor 2 reducing decay losses especially for short-lived isotopes. In Fig. 5.3, a comparison of the calculated efficiencies for both, the standard cycle and the short-cycle, for ^{254}No and the shorter-lived ^{251}No ($T_{1/2} = 0.8$ s are shown as a function of the total cycle time following Eq. 4.5. The beam-off periods are fixed with regard to the respective cycle and the beam-on-target time is varied thus affecting the total cycle time. Based on this, the optimum beam-on-target period for accumulation on the filament can be determined for the investigated isotope and a fixed beam-off period to maximize the cycle efficiency.

Finally, a direct comparison of the RADRIS efficiencies $\epsilon_{\mathrm{RADRIS}}$ of the previous cycle and the new short cycle is visualized with solid lines in Fig. 5.4 in dependence of the half-life of the studied species as suggested from Eq. 4.5. Besides the expected efficiencies normalized to the overall efficiency of ^{254}No from RIS [27], experimentally determined efficiencies for different isotopes are included for the previous cycle with black data points, and for the short cycle with blue data points. These efficiencies were extracted from the ratio of detected laser-induced ions relative to the rate of ions from a direct transport to the detector ("flushing"). The extracted relative RIS rates were normalized to the respective rate of ^{254}No to estimate the total efficiencies for these cases. The data points shown in red present the estimated efficiencies for short-lived and longer-lived nobelium isotopes including the changes of the RADRIS transport electrode structure described below[1], which will be further discussed in Sec. 5.3.

[1] In comparison with the measurements performed with the standard RADRIS setup described in Ref. [133], the upgraded setup with optimized electrode potentials showed a changed ratio between RIS versus flushing rates and a generally lower flushing efficiency, as the setup was optimized for ions originating from the filament. For a comparison of the relative RIS efficiencies with the previous measurements shown in blue in Fig. 5.4, the flushing rates for the new setup (red) were therefore

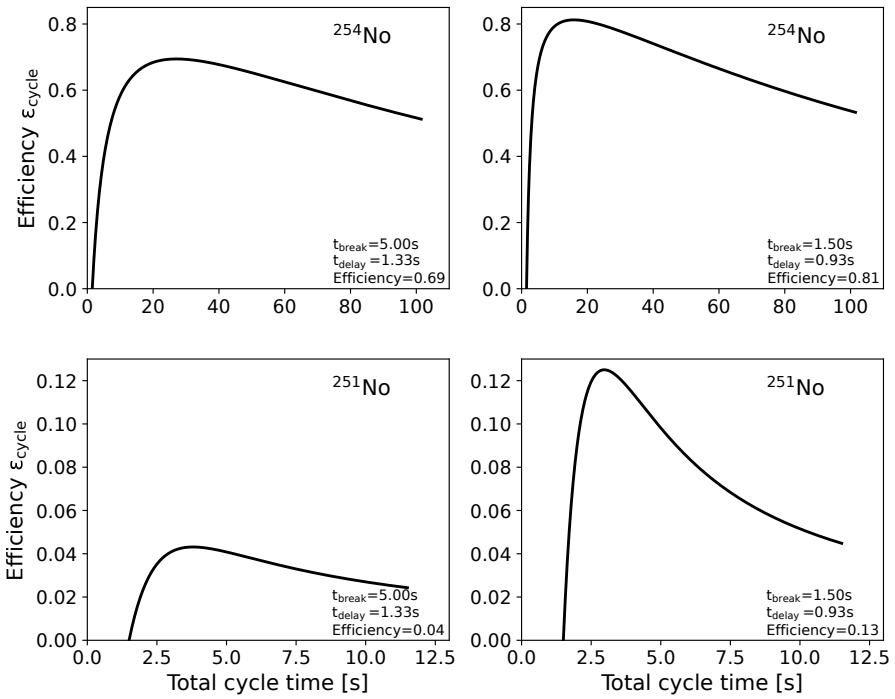

Figure 5.3.: Simulated RADRIS cycle efficiencies for ^{254}No and ^{251}No in dependence of the total cycle time. The beam-off periods are fixed and the beam-on-target period varied. The left panels show the standard RADRIS cycle with extended beam-off period used in prior beamtime campaigns for ^{254}No and assumed for ^{251}No. The right panel shows the expected cycle efficiency ϵ_{cycle} for the new short cycle featuring a reduced beam-off period and minimized delay time before ion detection on the detector.

owever, as the ratio of signal from RIS versus direct transport has changed with the new upgraded electrode structure, for a more precise value,

A general enhancement in the overall efficiency is suggested, in particular, for isotopes with half-lives of 1 s and more which were previously studied. In comparison to the overall efficiency of 6.4 % for ^{254}No [27] with the previous cycle, the enhancement in ϵ_{cycle} alone, simulated for the short cycle, reflects an increased efficiency of $\epsilon_{\text{RADRIS}} = 7.5\,\%$.

corrected by a factor of 1.4 which was found between earlier higher flushing rates and those for the new setup. For a precise determination of the overall efficiency, it should better be inferred directly from comparison of the rate of detected ions from RIS relative to incoming ions from SHIP.

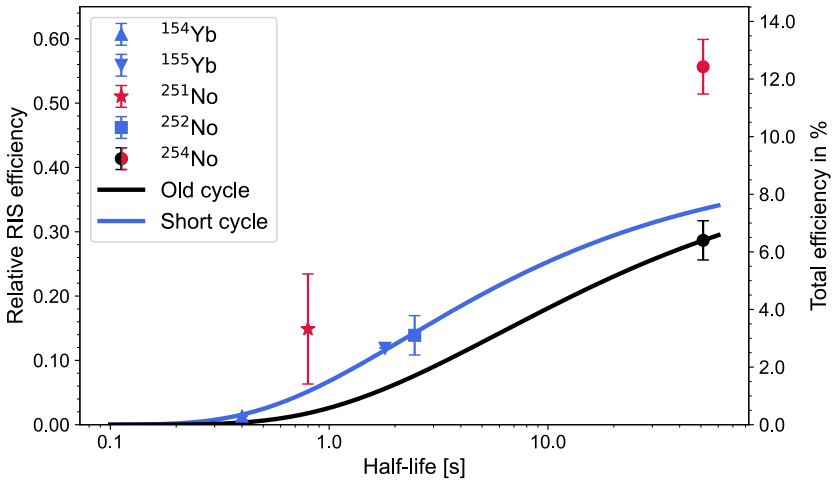

Figure 5.4.: Comparison of efficiencies for different isotopes and RADRIS cycles. Solid lines show the simulated efficiency ϵ_{cycle} as a function of the half-life of the studied isotopes for the previous longer RADRIS cycle (black) and the optimized short cycle (blue). Data points show the measured RIS efficiencies relative to the respective direct transport ("flushing") rate. Measurement points in blue show respective values extracted with the applied short cycle. Overall RADRIS efficiencies are added via the right scale and calculated relative to the known efficiency of ^{254}No [27]. Red data points show efficiencies extracted for the new optimized RADRIS setup with upgraded transport electrode structure (see Sec. 5.3). Figure adapted from [164].

5.3. Optimizing the RADRIS detection setup

In order to enable the application of the RADRIS technique to more exotic nuclides with production cross sections as small as only tens of nb as for instance for ^{251}No or ^{245,246}Fm (see Tab.4.1), an optimal efficiency must be ensured. Furthermore, an improved efficiency can provide a significant benefit for search experiments of yet unidentified atomic levels such as in the case of lawrencium. Here, the production cross section is about one order of magnitude lower compared to the nobelium isotone previously targeted in a level search experiment with RADRIS (see Tab.4.1). Additionally, the odd proton number, and consequently a non-zero spin, results in a hyperfine splitting within atomic levels, leading to a spread of the resonance signal over several frequency scan steps. Hence, an optimum performance throughout a level search campaign is crucial to avoid missing a resonance signal from experimentally unknown atomic levels. An upgraded detection system with an enhanced sensitivity and efficiency for applications to species with half-lives $t_{1/2} > 5\,\text{s}$ was developed, increasing both $\epsilon_{\text{transport}}$ and $\epsilon_{\text{detection}}$, tailored to the search for atomic levels in lawrencium.

The original RADRIS setup, as discussed in Sec. 4.3.1 and shown in Fig. 4.8, used a single PIPS detector in combination with a thin collection foil in front. A solid angle coverage for the emitted alpha particles of about $\epsilon_{\text{detection}} = 40\,\%$ was achieved with this configuration [27]. In the new setup, the previously used detector was replaced by

a custom manufactured PIPS detector with an active area of 600 mm^2 and a 125 nm aluminum layer for suppression of background from scattered laser light and the filament heat pulses. With this new light-shielded detector, the collection foil became obsolete.

It is important to note that the coating had to be kept as thin as possible, to preserve a good resolution for alpha events resulting from ions directly collected on the active area. If the coating layer becomes too thick, significant tails in the alpha spectrum may be observed due to increased energy loss within the layer. In particular, the effective thickness experienced by alpha particles emitted at shallow angles on the detector surface is considerably larger than the one seen by alpha particles emitted nearly perpendicular to the active surface or at steeper angles from a collection foil in front. Nonetheless, the decreased resolution comes with the advantage of an increased solid angle of up to 50 % and therefore a gain in detection efficiency.

With the custom coating, an optimum resolution of 46 keV for alpha particles emitted at about 5.2 MeV energy from a closed triple-alpha source[2] at a large distance to the detector was achieved. The observed performance of this detector type was comparable to a non-coated 450 mm^2 PIPS detector and no strong impact of the coating on the resolution was determined. For alpha particles emitted by collected ions on the detector surface itself, an optimum resolution of about 150 keV at 8 MeV was reached in on-line conditions coupled to SHIP. The comparison between different utilized PIPS-detector types is discussed in the appendix in Sec. A.1.

Furthermore, for the custom coated new detector type, no background events from the laser or the filament heat pulses were registered in the alpha-energy range of the events of interest, typically between 6 MeV and 10 MeV. Although the resolution in on-line condition is relatively low, it is still sufficient to distinguish alpha events from all investigated isotopes of interest and their decay daughters, for instance ^{254}No from ^{250}Fm. For the lawrencium level search on the other hand, this resolution is at the limit of resolving the ground state with an alpha energy of 8365 keV from the isomer with 8457 keV [167].

5.3.1. Movable double-detector setup for an enhanced detection efficiency

The cyclic application of RADRIS offers the opportunity for a new detection scheme: it enables the movement of the collection detector to an off-axis position during the filament accumulation period. In this time, the detector can be moved on a rail system with a pneumatic linear actuator of 50 mm stroke between the collection spot in the detection area of RADRIS and an off-axis detection position. In this location, a second identical PIPS detector is positioned close to the collection detector with the active areas facing each other and a gap of about 4 mm between them. This approach allows

[2] The available triple-alpha source contained the isotopes ^{239}Pu, ^{241}Am and ^{244}Cm, example spectra are shown in the appendix in Sec. A.1.

for the detection of alpha particles emitted in the hemisphere opposite the active area of the primary detector. These alpha particles, which would usually be missed, can thus be detected by this additional detector. Fig. 5.5 shows the technical implementation of the movable-double detector setup.

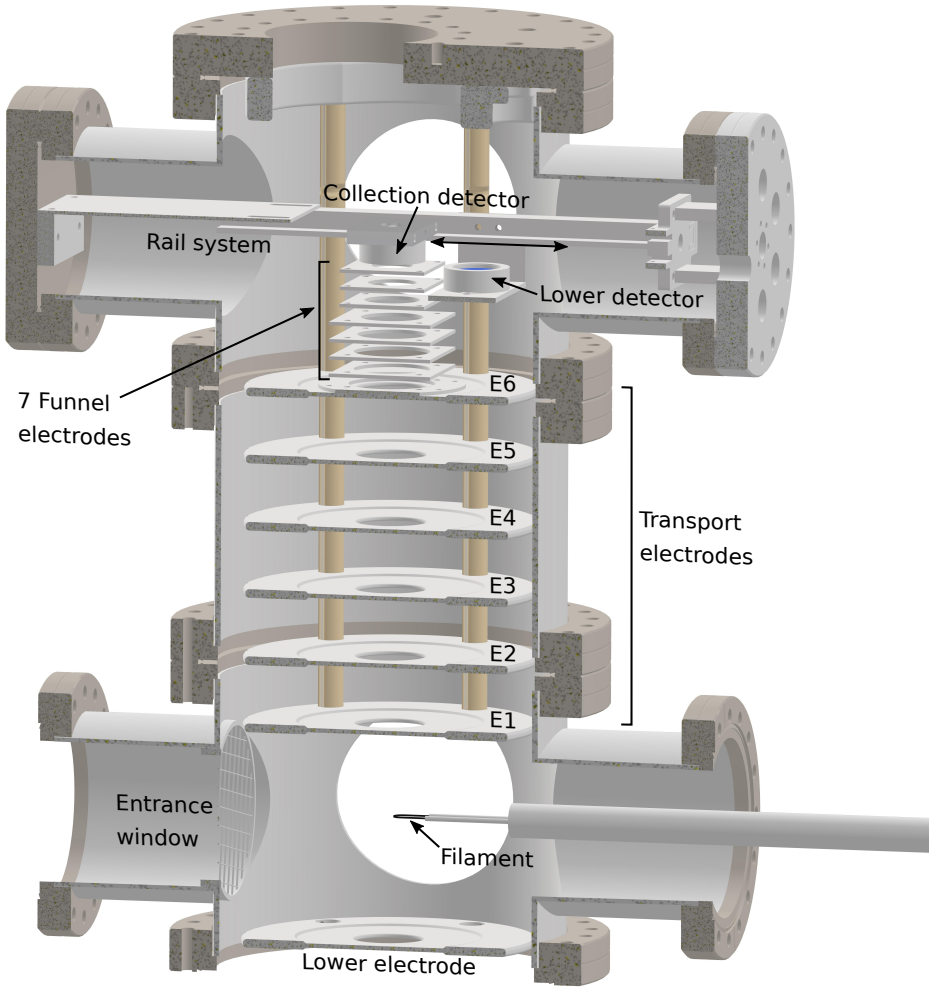

Figure 5.5.: Upgraded RADRIS setup with improved transport electrode structure and movable double-detector setup for an increase in solid angle coverage. The beneficial feature of the additional detector can be used for isotopes with half-lives $t_{1/2} > 5\,\mathrm{s}$. This setup was used during the lawrencium level search campaign in 2022.

To realize the new setup within the RADRIS experimental chamber, the transport electrode structure in the previous setup shown in Fig. 4.8 had to be re-designed. The cage electrode around the primary detector had to be removed to gain space for the rail system in the new arrangement. Two additional main transport electrodes

Electrode	Accumulation [V]	Transport [V]
Filament	400	1050
Cross Piece	1025	1025
Lower electrode	1015	1015
Electrode 1	925	925
Electrode 2	818	818
Electrode 3	711	711
Electrode 4	604	604
Electrode 5	497	497
Electrode 6	390	390
Funnel entrance	365	365
Funnel exit	130	130
Detector	0	0

Table 5.2.: Potentials applied in the upgraded RADRIS setup including the advancements in the transport electrode structure and the short cycle implementation described in this chapter. The filament accumulation and ionization/transport mode potentials are constant up to the filament potential, which is switched during the cycle.

were added to ensure an optimal ion transport to the detection area. To confine the spacial distribution of the ions towards the detector surface, a DC-funnel structure with progressively decreasing apertures was integrated in the new design.

To achieve optimal transmission through the newly developed transport electrode structure for efficient collection on the detector, the ion trajectories in the buffer-gas atmosphere were initially simulated using SIMION 8.1 [168]. Here, a study of the effect of different voltage gradients in the DC-funnel structure in combination with the main transport electrode structure was conducted to determine the optimal potential settings for highest transmission. With prospective settings from the simulations, an analogue study was performed on the setup itself by testing the transmission of ions for the respective potential settings. Here, a ^{225}Ac recoil source was mounted onto the entrance window flange yielding ^{221}Fr recoil ions that were firstly collected on the filament and subsequently surface ionized via an applied heat-pulse. The resulting ^{221}Fr ions were subsequently guided to the detector. Few of the most promising settings for a maximized collection of ions were tested on-line, and the optimal settings found are summarized in Tab. 5.2. These were applied in the advanced RADRIS setup for measurements on ^{251}No and ^{245,246}Fm described in this work, as well as for the level search campaign in lawrencium. Further discussion of the ion trajectory simulations and optimization of the transport potentials can be found in the appendix A.2.

The movable double-detector setup with the improved transport electrode structure was commissioned in the beamtime campaign in 2022 in laser spectroscopy measurements on ^{254}No. In the short cycle scheme in Fig. 5.6, which illustrates only the

beam-off period, the movement of the linear actuator driving the detector is included. The main collection detector is positioned in the off-axis location during filament accumulation mode. It should remain in this position in combination with the additional detector as long as possible to benefit from the increased solid angle coverage. Following the trigger of the potential switch, the detector is moved on-axis to collect ions resulting from resonance ionization. It is returned to the detection position following the potential switching 0.2 s before requesting the primary beam again. The velocity of the movement is sufficiently fast to reach the on-axis position before the arrival of the ions. No losses or background from induced noise in the alpha-energy gate due to the movement were observed compared to a stable position in this location. For possibly arising noise from the movement after enduring operation, the a veto gate of the Data Acquisition (DAQ) to neglect noise events during the movement was foreseen.

Several RADRIS cycles were performed with this setup and resonantly laser ionized reaction products guided towards the collection detector. The efficiency gain with the additional detector was determined by comparing the detected alpha events from ^{254}No on both detectors. The accumulated alpha spectra in both detectors are shown in Fig. 5.7. The additional detector captured 67 % of the alpha-decays registered by the collection detector alone. These events would usually be missed and therefore give a direct gain in detection efficiency $\epsilon_{\text{detection}}$. An overall efficiency of $\epsilon_{\text{RADRIS}} > 15\,\%$ was determined and the RADRIS efficiency for ^{254}No therefore more than doubled.

This dual-detector system was applied in the extensive level search campaign in lawrencium in the beamtime in 2022. The results of the campaign will be published independently [169]. The performance of the detector system was stable over the entire duration of a few weeks of continuous beamtime. It is therefore planned to be applied for future experiments on more exotic isotopes with suitable half-lives.

5.3.2. Rotatable detector setup for studies of longer-lived isotopes

In the standard RADRIS detection scheme, resonantly laser ionized reaction products are collected on one primary detector located on the chamber axis. Their alpha-decays have to be registered either by the single detector or the combination of two detectors in the movable double-detector scheme. Regardless, in all cases the subsequent alpha-decay of remaining recoil ions on the detector must be awaited after completing a desired number of RADRIS cycles for a laser scan step. To ensure the complete decay, a waiting time equivalent to about 3-4 half-lives of the considered species is included before probing the next laser wavenumber. For longer-lived isotopes with half-lives in the order of tens of minutes or even longer, the waiting time for subsequent decays is time-consuming and hinders an efficient utilization of beamtime. For such long-lived isotopes, a new detection scheme was developed enabling parallelization of the collection of ions from laser resonance ionization and the registration of subsequent decays from a previous scan step. As a result, collection mode and detection mode off-axis are disentangled in time.

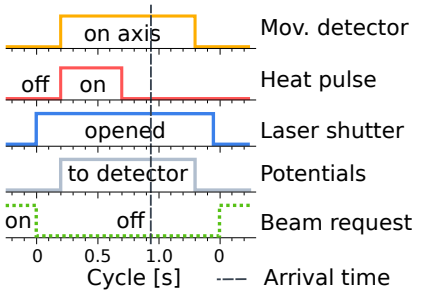

Figure 5.6.: Schematic of the RADRIS cycle beam-off period combining the newly developed short-cycle and the movable double-detector setup. The primary collection detector is moved in the on-axis position 0.2 s after the beam stop to receive ions from the ongoing RADRIS cycle. The latter are expected to arrive about 0.93 s after the beam stop. After 1.3 s it is moved back in the off-axis position and the next cycle is started.

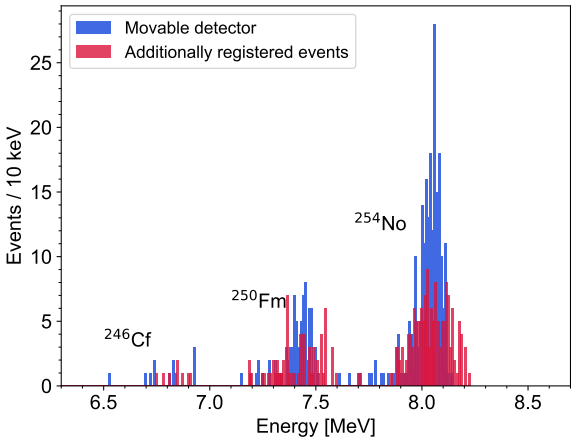

Figure 5.7.: Alpha spectrum of registered events per bin from RIS measurements on ^{254}No with the movable double-detector setup. Events from ^{254}No and subsequent decay daughters on the primary collection detector are shown in blue, additionally registered events seen by the lower detector are presented in red. These events would usually be missed.

The design of the rotatable multi-detector setup is shown in Fig. 5.5. A set of three identical PIPS detectors, each with an active area of 450 mm^2, is mounted on a disk connected to a rotatable feed-through with a rotation axis off from the chamber axis. The rotation of this setup allows for a single detector to be aligned on the chamber axis for collection mode, while the other two detectors remain in an off-axis position in detection mode. After concluding the collection of the last RADRIS cycle for a scan step, the detector is rotated to an off-axis position for detection mode, where subsequent decays are registered. The next detector, now located on-axis for collection, can immediately receive ions from cycles of the next laser scan step to be probed.

This new detection scheme was commissioned in the beamtime campaign in 2021 during laser spectroscopy studies of the long-lived isotope ^{254}Fm ($t_{1/2}$ = 3.2 h). The experiment as part of this thesis work is explained in detail in chapter 6 and results are presented in chapter 7.

5.4. First laser spectroscopy of ^{251}No

The advancements made in the RADRIS system and the improved measurement principle, which offer a generally enhanced efficiency, particularly for shorter-lived species, have opened up new opportunities for laser spectroscopy studies of nuclides that were previously inaccessible. An isotope of high interest was ^{251}No with a half-life of only 0.8 s and a low production cross section of 30 nb [135]. For the previous less efficient

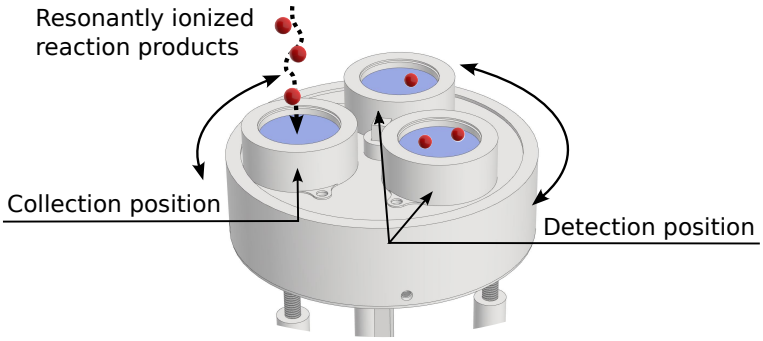

Figure 5.8.: Schematic representation of the rotatable multi-detector setup used for laser spectroscopy studies of long-lived ^{254}Fm. The setup is rotated to align one detector on axis for collection of laser induced ions. The additional two detectors located off-axis register subsequent events of reaction products collected in previous laser scan steps.

RADRIS setup, considering the low production yield and the significant decay losses, the detection and study of this isotope was not feasible. Due to the enhanced overall efficiency and the short-cycle development, laser spectroscopy for this particular case came in reach. A first experiment targeting this isotope was conducted during the beamtime campaign in 2022. Due to the short half-life and thus cycle time relative to the required time for driving the movable detector, the collection detector was kept in the on-axis position resulting in a reduced solid angle coverage and therefore $\epsilon_{\text{detection}} = 50\,\%$. The result of successfully resonant laser ionized reaction products is shown in Fig. 5.9. As previously introduced in Fig. 5.4, a total efficiency of 3.3(1.9) % was estimated with the short cycle and the optimized RADRIS setup. However, as the ratio of signal from RIS versus direct transport has changed with the new upgraded electrode structure, for a more precise value, this efficiency should better be inferred directly with the rate of incoming recoil ions in comparison to detected ions from RIS.

In this first RIS spectrum, a resonance structure was observed. Due to an elevated laser power used in this experiment, power broadening is expected. Furthermore, the nuclear spin of 7/2 [115] leads to a sub-structure of three hyperfine levels that could not be resolved, and additionally complicates and broadens the spectrum. The existence of an isomer adds more complexity to the underlying, not resolved sub-structure. With a similar half-life of 1.0 s and a comparable alpha energy of 8612 keV for the ground state and 8668 keV for the isomer, both species cannot be distinguished with the limited resolution of the PIPS detector under on-line conditions. Therefore, transition resonances from both, the ground state and isomeric state, may be included in the same RIS spectrum as the isomer shift can be expected to be relatively small. With an expected spin of 9/2 for the isomer [115], the hyperfine structure in the atomic transition would also be observed.

More in-depth studies are required to investigate ^{251}No via laser spectroscopy and to extract nuclear properties such as the change in mean-square charge radius from the isotope shift to extend the range of studied isotopes in nobelium [28]. Nonetheless,

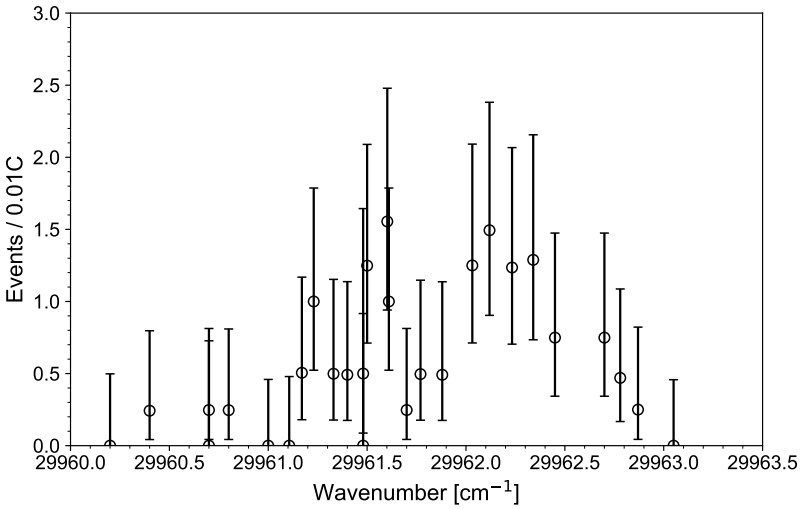

Figure 5.9.: First laser spectroscopy results on ^{251}No. This proof-of-principle experiment showcased the capabilities of the advanced RADRIS setup to study isotopes with half-lives shorter than 1 s and with production cross sections of only few tens of nb. More detailed studies will be required to investigate the underlying sub-structure for the extraction of nuclear information.

this proof-of-principle experiment opened doors for the study of more exotic nuclides showcasing the capabilities of the RADRIS technique for short-lived and rare nuclides. In the same experimental campaign, laser spectroscopy of ^{246}Fm with an even lower cross section and a half-life of 1.54 s was shown to be feasible as discussed in more detail in Sec. 6.1.

6. Measurement and analysis procedures

Ongoing developments in laser spectroscopy, applying the RADRIS method and aimed at the study of exotic heavy elements, have created opportunities for the investigation of isotopes which were previously not in reach. In the following chapter, experiments on the heavy actinide element fermium performed in the framework of this thesis are introduced. These studies, ranging from neutron deficient ^{245}Fm up to ^{257}Fm in the vicinity of the $N = 152$ shell gap, combined various off-line and on-line production schemes along with complementary laser spectroscopy techniques. Methodological advancements in the two applied techniques, the previously introduced RADRIS method and hot-cavity laser spectroscopy, gave access to this long chain of isotopes.

The experimental techniques will be explained and details on the measurements are presented. The analysis procedure of the obtained data will be introduced before results are presented and interpreted in the following chapters.

6.1. On-line studies of short-lived fermium isotopes

In the following, the specific production and measurement schemes for the investigated fermium isotopes are individually explained. A summary is shown in the nuclear chart cut-out in Fig. 6.1 with the studies isotopes highlighted and their decay modes given. The indirect production schemes via respective nobelium mother isotopes are indicated. For the isotopes studied on-line, a summary of the parameters for the RADRIS schemes such as the half-life of the isotopes and the respective cycle times is presented in Tab. 6.1

6.1.1. Production and measurement of ^{245}Fm and ^{246}Fm

The isotopes ^{245}Fm, ^{246}Fm were produced directly using a $^{40}Ar^{8+}$ main beam with a beam energy of 4.837 MeV/u and 4.62 MeV/u, respectively, and average intensities of 2 particle µA from the UNILAC accelerator in combination with an isotopically enriched ^{208}PbS target. Laser spectroscopy with RADRIS became feasible for these two isotopes, with production cross sections of 15 nb - 22.5 nb, thanks to the enhanced sensitivity of the upgraded setup featuring the short RADRIS cycle and the overall increased ion transport efficiency described in Sec. 5.1. For ^{246}Fm, along with one of

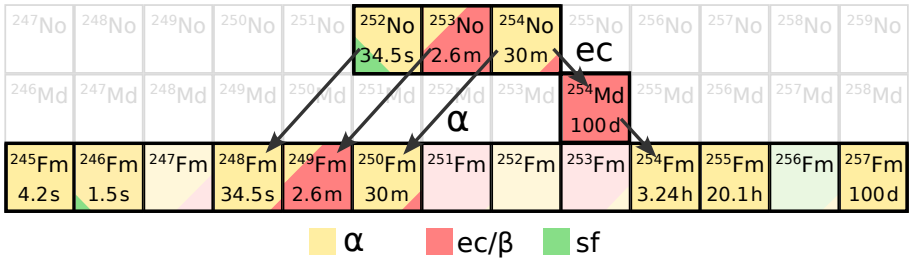

Figure 6.1.: Nuclear chart excerpt with on-line production schemes of studied fermium isotopes. The indirect production paths via the respective nobelium decay mother are marked with arrows. The decay modes with relative branching ratios are color-coded.

Direct or indirect production	Branching ratio%	Half-life	Cycle	Time
^{208}Pb(^{40}Ar,3n)^{245}Fm	100	4.2 s	2.5 s, 1.75 s	2 h
^{208}Pb(^{40}Ar,2n)^{246}Fm	93	1.54 s	2.5 s, 1.75 s	2 h
^{206}Pb(^{48}Ca,2n)^{252}No $\xrightarrow{\alpha}{}^{248}$Fm	65, 95	34.5 s	30 s, 5 s	25 min
^{207}Pb(^{48}Ca,2n)^{253}No $\xrightarrow{\alpha}{}^{249}$Fm	55, 33	2.6 min	300 s, 5 s	1 h
^{208}Pb(^{48}Ca,2n)^{254}No $\xrightarrow{\alpha}{}^{250}$Fm	90, 90	30 min	360 min, 5 s	2.5 h
^{208}Pb(^{48}Ca,2n)^{254}No $\xrightarrow{ec}{}^{254}$Md $\xrightarrow{ec}{}^{254}$Fm	10, 100, 99.9	3.24 h	1 h, 3.1 min, 5 s	22.1 h

Table 6.1.: Direct and indirect production schemes for on-line produced fermium isotopes. The alpha- and electron capture-branching ratios, respectively, of the involved isotopes in the production scheme are presented. The respective RADRIS cycle with the collection and beam-off time are given for each isotope. The total time per measurement point, as indicated in the respective column, was selected to ensure sufficiently good statistics.

the lowest production cross sections of species studied via the RADRIS method to date, only about one nucleus per 100 s was available in the gas cell. Additionally, the shorter half-life (see Tab. 6.1) leads to a 40 % lower efficiency of the RADRIS cycle in comparison to ^{245}Fm. The direct production scheme for both isotopes featured a collection time of 2 s on the filament, followed by the short RADRIS cycle beam-off period and laser resonance ionization as described in Sec. 5.2. With the intense argon main beam, the scan of the resonance on both isotopes was performed in less than a day.

6.1.2. Production and measurement of ^{248}Fm, ^{249}Fm and ^{250}Fm

The indirect production of the isotopes ^{248}Fm, ^{249}Fm, and ^{250}Fm was enabled via alpha-decay of their respective nobelium mother isotopes as depicted in Fig. 6.1. Details on the production of ^{254}No, ^{253}No, and ^{252}No, respectively, via a ^{48}Ca^{10+} beam with average beam-on-target intensities of 0.64 particle µA, are described in Sec. 4.1. Main beam from the UNILAC with a 40 Hz pulse repetition rate was available for the experiments.

Firstly, ^{250}Fm was accessed via the collection and subsequent decay of directly produced ^{254}No on the filament for a duration of 6 min per RADRIS cycle. A total number

of 5 cycles was performed per laser scan step and a subsequent waiting time of 2 h ensured the complete decay of all ^{250}Fm recoil nuclei on the PIPS detector. Due to the much longer half-life of ^{250}Fm of $t_{1/2} = 30$ min compared to the ^{254}No mother, decay losses of ^{250}Fm in the waiting time after the beam stop and the beam-off period in the cycle are negligible. A reduction of 50 % due to implantation into the filament material and the 90 % alpha-branch of ^{254}No need to be considered, thus leaving a maximum fraction available of 45 % of ^{250}Fm for RIS relative to the number of incoming ^{254}No nuclei. A total of about 3 days of main-beam time were required for the full resonance scan with 17 scan steps.

The isotope ^{249}Fm, indirectly produced via the alpha-decay of directly produced ^{253}No, was collected for 5 s on the filament per RADRIS cycle. Each laser scan step was concluded after performing 10 cycles and a subsequent decay time of 10 min. The low alpha branch of both, mother nuclide and daughter nuclide, of only 55 % and 33 %, respectively, and the lower direct production yield of the mother isotope (see Tab. 4.1) reduced the overall efficiency. Furthermore, due to the comparable half-life of ^{249}Fm relative to ^{253}No ($t_{1/2} = 1.6$ min), large decay losses are expected in the waiting time between the stop of the primary beam and the filament desorption, leading to a further reduced cycle efficiency. The experiment was concluded in about 2 full days of measurement. More details on the experiment procedure can be found in Ref. [166].

The shorter-lived ^{248}Fm with $t_{1/2} = 34.5$ s was indirectly produced via collection of ^{252}No on the filament for 30 s, followed by a decay time of 2.5 s on the PIPS detector after concluding 10 cycles. Due to the relatively long half-life of the daughter nuclide compared to ^{252}No with $t_{1/2} = 2.46$ s, the decay of produced nuclei in the short decay time is small and not expected to lead to significant losses. The full resonance scan was performed in half a day with parasitic beam.

In the first laser spectroscopy experiment of ^{250}Fm using the new indirect production scheme, an elevated laser power was used. In this way, the laser ionization efficiency was maximized, however, at the expense of a decreased resolution due to power broadening effects. For this measurement, a laser pulse energy of 150 µJ/pulse was applied, whereas it was kept around 70 µJ/pulse for all other isotopes studies at GSI. Assuming a laser-spot size of approximately 3 cm^2 and the respective transition wavenumber of about 25 112 cm^{-1}, a photon flux of $1 \cdot 10^{14}$ photons/cm^2 and $0.5 \cdot 10^{14}$ photons/cm^2 would be expected, respectively. Comparing these experimental conditions with the saturation behavior probed with the initial IGRIS measurements [120], saturation is expected to be reached for the higher flux of $1 \cdot 10^{14}$ photons/cm^2. The increased linewidth in the observed transition, discussed in chapter 7 in Fig. 7.1, is visible in the resonance spectrum of ^{250}Fm in comparison to ^{248}Fm. These measurements were both performed in the same on-line beamtime campaign under similar experimental conditions, yet with lineshapes differing by 2.5 GHz in FWHM, solely accountable to power broadening effects, as discussed in Sec. 7.1.

6.1.3. Production and measurement of ^{254}Fm

The rather long-lived isotope ^{254}Fm with $t_{1/2} = 3.2\,\mathrm{h}$ was indirectly produced via the decay of ^{254}No as stated in Tab. 6.1. Parasitic beam from the UNILAC was available for this experiment with a 5 Hz pulse rate and an average beam-on-target intensity of 80 particle nA. The mother nuclide ^{254}No was produced with an isotopically enriched ^{208}PbS target and collected on the filament. The decay path, involving the 10 % electron-capture branch, followed by the intermediate electron-capture decay of ^{254}Md with $t_{1/2} = 10\,\mathrm{min}$, was utilized for accumulation of ^{254}Fm on the filament. A primary accumulation time of 1 h of ^{254}No and an additional 3.1 min decay time on the filament before desorption ensured the close to complete decay of the intermediate isotope ^{254}Md. The absolute fraction of available ^{254}Fm recoil nuclei relative to the incoming primary nobelium nuclei was expected to be only 5 %, accounting for the alpha-branching ratios and the assumed loss of 50 % of captured recoil nuclei.

For sufficient statistics, seven RADRIS cycles were performed per laser scan step, each of a duration of 3790 s. Due to the long half-life, a complete measurement of a laser scan step required an additional waiting time of at least 13 h corresponding to 4 half-lives of ^{254}Fm. In summary, the total measurement time of a laser scan step lasted 22.1 h.

The experiment was performed by applying the dedicated rotatable-multi-detector setup described in Sec. 5.1 to allow for a reasonable and time saving beamtime usage. The collection of ions for a laser scan step were concluded on one PIPS detector. To start the next measurement, the setup was rotated such that a "fresh" PIPS detector was positioned on-axis to receive ions from the next laser scan step with a new wavenumber to be probed. The decay of the recoil ions on the previous PIPS was awaited in an off-axis position to complete the measurement. In this way, every detector was re-used for a new measurement every $2 \times 7.4\,\mathrm{h}$ after concluding the previous collection. This time resembles more than five half-lives such that a clean detector and no remaining activity of ^{254}Fm was available by the time a new scan step was started. Finally, the complete experiment of RIS of ^{254}Fm was performed in about five and a half days.

6.2. Off-line studies of long-lived isotope samples

Macroscopic sample sizes of the neutron-rich fermium isotopes ^{255}Fm and ^{257}Fm became accessible from reactor breeding processes. The initial HFIR sample, produced in three irradiation cycles of three to four weeks each, contained a fraction of 1.38 pg of ^{257}Fm besides nanogram amounts of ^{249}Cf and ^{253,254}Es[1]. A radio-chemical separation [128] was performed on the fermium of the sample in collaboration with Florida State University and the Department of Chemistry - TRIGA site Johannes Gutenberg-

[1] A detailed description and analysis of the sample composition via mass scans in the RISIKO mass separator are contained in the PhD thesis of S. Nothhelfer [170].

Universität Mainz. The separated ^{257}Fm sample, with an estimated size of maximum $5 \cdot 10^7$ atoms, was finally deposited on a zirconium carrier foil (10 mm × 10 mm). The latter facilitates the release of fermium atoms, enabling for laser spectroscopy studies on the neutral state. More details on the chemical separation will be compiled in Ref. [171].

The remaining ^{254}Es fraction with an assumed sample size of $6.8{\cdot}10^{11}$ atoms (equivalent to a sample size of 290 pg) from the initial HFIR sample was re-irradiated for seven days at ILL for breeding of ^{255}Es to a sample size of about $1{\cdot}10^9$ atoms. The remaining sample of ^{255}Es constituted a radionuclide-generator system for ^{255}Fm via β^--decay of the former. The fraction of the ^{255}Fm decay daughter was chemically separated when it was found in radioactive secular equilibrium with its decay mother. In total four separations in appropriate time intervals could be performed. Similar to the prior case, ^{255}Fm was deposited on a zirconium carrier foil for further usage of the sample. In this way, three samples of $3.8 - 8.8 \cdot 10^6$ atoms each of ^{255}Fm were produced.

Both reactor-bred fermium isotopes were investigated at the RISIKO mass separator in the physics department of Johannes Gutenberg-Universität Mainz in the vicinity of the TRIGA-site. The proximity of both laboratories allowed minimizing decay losses after chemical separation of the shorter-lived isotope ^{255}Fm. The versatile RISIKO apparatus is well suited for laser spectroscopy on sample sizes down to the trace-analysis level. It therefore allowed for laser spectroscopy studies on prepared fermium samples as will be described in the following section.

6.2.1. RISIKO mass separator

The Resonance Ionization Spectroscopy in Collinear geometry (RISIKO)[2] mass separator mainly consists in the combination of a hot-cavity laser ion source and a mass separating dipole magnet similar to laser ion sources at on-line RIB facilities such as the Resonant Ionization Laser Ion Source (RILIS) at ISOLDE, CERN [90] or TRIUMF [125]. Initially, RISIKO was developed for laser-based resonance ionization mass spectrometry (RIMS) for trace analysis studies in environmental samples such as of ^{90}Sr [172]. Presently, RISIKO is primarily used for applications such as separation and implantation of isotopically pure ion beams into specific target wafers and microcalorimetric detectors [83, 173]. Additionally, it is employed for laser RIS studies of both, stable and radioactive long-lived isotopes [174, 175, 176] as it allows the off-line production of RIBs. A schematic overview over the RISIKO apparatus is shown in Fig. 6.2. A detailed description of the experimental setup and its applications is given in Ref. [177].

The RISIKO separator is rather compact with about 7 m total length and allows measurements under high vacuum conditions with 10^{-7}mbar – 10^{-8}mbar. The hot-cavity laser ion source of RISIKO consists of a tantalum atomizer tube oven

[2] The acronym is derived in German from Resonanz-Ionisations Spektroskopie In Kolinearer Geometrie (RISIKO).

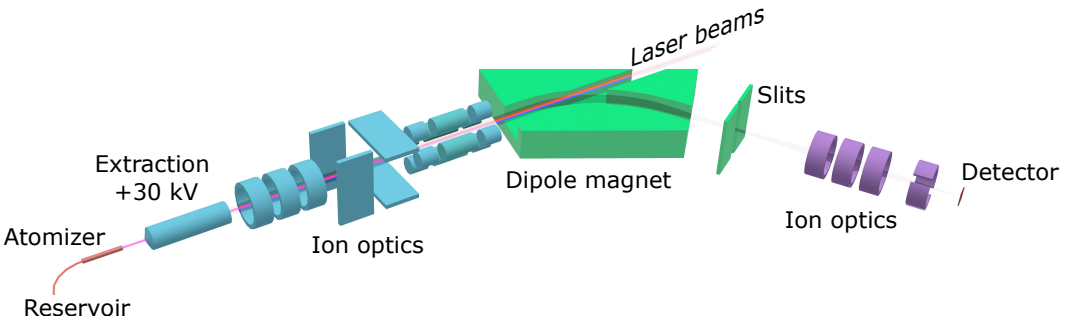

Figure 6.2.: Schematic overview of the RISIKO mass separator at Johannes Gutenberg-Universität Mainz. It mainly features a hot-cavity laser ion source shown on the left. Samples are evaporated and resonantly ionized by laser illumination in the atomizer before extraction and beam shaping downstream of the source. The dipole magnet in the middle of the setup allows for mass separation followed by single ion detection at the end of the beamline. Figure adapted from [173].

(19 mm depth × 2.5 mm inner diameter × 1 mm thickness) with a bent capillary connected to the back of the atomizer, acting as sample reservoir. Chemically separated fermium samples on the zirconium carrier foils were placed inside the atomizer, which was resistively heated. With sufficiently high temperatures between 1100 K and 1600 K, fermium was evaporated, whereas the zirconium material of the carrier foil supported the release in the form of neutral atoms. To minimize background from surface ions of the same or other species[3], the atomizer was initially baked in high vacuum condition at temperatures of about 2000 K. Throughout the measurement campaign, the temperature of the sample heating was maintained at the lowest possible level to minimize surface ionization effects.

Two laser beams following the respective ionization scheme illuminated the localized hot vapor in the hot cavity anti-collinearly to the final ion-beam extraction direction. Resonantly laser created ions were subsequently extracted from the ion source and accelerated by a 30 kV extraction potential. Ion optics for beam shaping and guidance in combination with a dipole magnet for mass selection (mass resolving power $\frac{m}{\Delta m} \approx 1000$) allowed the transmission of ions of a specific mass-to-charge ratio downstream to a secondary electron multiplier detector for single-ion counting.

Recent developments of the RISIKO apparatus facilitated an additional improvement in the signal-to-background ratio by laser-beam gating of the arriving ion species at the downstream detector [178]. By analyzing the characteristic arrival time structure of resonantly laser-ionized species of interest, determined to be about 30 µs after the laser trigger, a time gate was set to capture the respective ions within this time interval. Ions created from surface ionization on the other hand are independent from any laser interaction and hence showed a continuous distribution in the arrival time. This

[3]The reader is referred to Sec. 4.3.3 where the surface ion creation is explained via the Saha-Langmuir equation 4.4, which also applies here similarly to the case of the RADRIS filament desorption.

time-gated detection approach enabled the measurement of samples containing as few as 10^7 atoms, or even less, for the first time in preceding measurements conducted on ^{254}Es samples obtained from ORNL [179]. Similar laser spectroscopy studies were recently performed on ^{253}Cf, produced as byproduct in the boosted einsteinium sample from ILL, using the Perpendicularly Illuminated Laser Ion Source and Trap (PI-LIST) structure in RISIKO [180]. This measurement proved the sensitivity of the technique paired with highest resolution down to a level of $5 \cdot 10^7$ atoms (corresponding to only 21 fg sample size) [29].

6.2.2. Laser system at RISIKO

The laser system used for the presented off-line laser spectroscopy measurements at RISIKO is based on custom-built Titanium:Saphhire (Ti:Sa) lasers. These lasers originated from the initial design described in Ref. [181] and have undergone continuous development since then. The utilized Ti:Sa lasers were pumped with the Second Harmonic Generation (SHG) output of high power Nd:YAG lasers with repetition rates of 10 kHz. Typical pulse widths of the Ti:Sa laser are between 40 ns and 60 ns and, depending on the cavity design, up to 5 W output power can be reached. The standard cavities yield a laser bandwidth of up to 10 GHz, while alternative designs also offer narrower bandwidth options. The RIS for the described fermium measurements was implemented by two Ti:Sa lasers delivering the FES and SES, respectively. Different laser systems in particular for the FES were applied in the two individual off-line campaigns at RISIKO.

For the initial measurement on ^{257}Fm, two grating-cavity lasers with intra-cavity SHG were used. The grating as wavelength-selective element yields a wide tuning range, which is especially beneficial for scanning broad wavelength ranges. The commonly used grating-cavities at RISIKO optionally feature a single intra-cavity etalon for narrow-bandwidth operation of 2-3 GHz linewidth. For further bandwidth reduction, a second, thick intra-cavity etalon was utilized in the FES laser system, which allowed for narrow-bandwidth operation at about 1 GHz linewidth [182]. The SES laser remained in the usual arrangement. The average output power remained alike for both configurations and ranged from 200 mW to 600 mW. For more detailed measurements on ^{255}Fm, an injection-locked Ti:Sa laser [183] with external SHG was applied for the FES. This system was seeded by a cw Ti:Sa laser [184] and enabled narrow-band spectroscopy down to a laser linewidth of 20 MHz at average output powers of 100 mW after frequency doubling.

For synchronization of the laser pulses of FES and SES, external triggering of the Nd:YAG pump lasers was enabled via a pulse generator. The laser wavelengths were monitored using a wavelength meter (HighFinesse, models WS7 and WSU). Regular calibrations were performed to a reference laser locked to a rubidium cell as described in Ref. [185].

6.2.3. Scheme development and comparison to prior in-gas cell work

During the initial campaign on ^{257}Fm, the SES step laser was scanned in order to search for a suitable AI. The development of an efficient RIS scheme with resonant ionization step was crucial for the presented off-line measurements, as available lasers for non-resonant ionization did not exhibit satisfyingly high pulse energies. An AI for the investigated transition R2 was identified around 52 165.5 cm^{-1} as shown in Fig. 6.3. The applied scheme with a resonant SES significantly improved the efficiency of the laser-based ionization compared to non-resonant ionization with the available Ti:Sa laser systems. The identified RIS scheme was subsequently applied for laser spectroscopy of both isotopes from reactor-breeding.

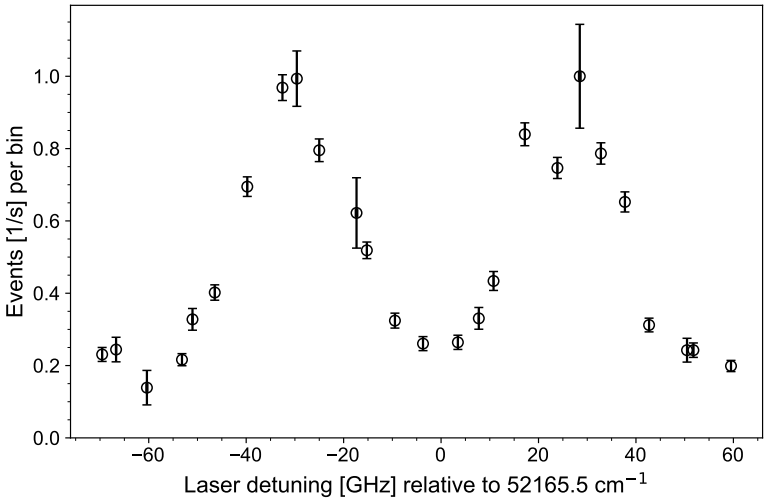

Figure 6.3.: Scan of an auto-ionizing state in fermium with the second excitation step laser. This AI resonance was found in off-line measurements on ^{257}Fm for transition R2 and subsequently applied in the fermium RIS scheme for the off-line studied isotopes

The results on ^{255}Fm from the hot-cavity work was compared to the previous in-gas cell work by Backe et al. [107], in which the same isotope was investigated. In Fig. 6.4, the direct comparison shows a good agreement between the centroid of the observed resonances within their uncertainties, indicated with gray shaded bands. The former work exhibits a much larger linewidth broadening due to the in-gas cell environment and thus pressure broadening. A shift between both spectra may be expected due to the Doppler and pressure shift contributions. However, as both shifts are assumed to be of a similar magnitude and sign, no net shift between the two is observed. This agreement validates the quality of the measurement procedure in the latest off-line campaign. It furthermore allows excluding large systematic shifts between the hot-cavity and the similar in-gas cell work performed with RADRIS for the on-line studied isotopes.

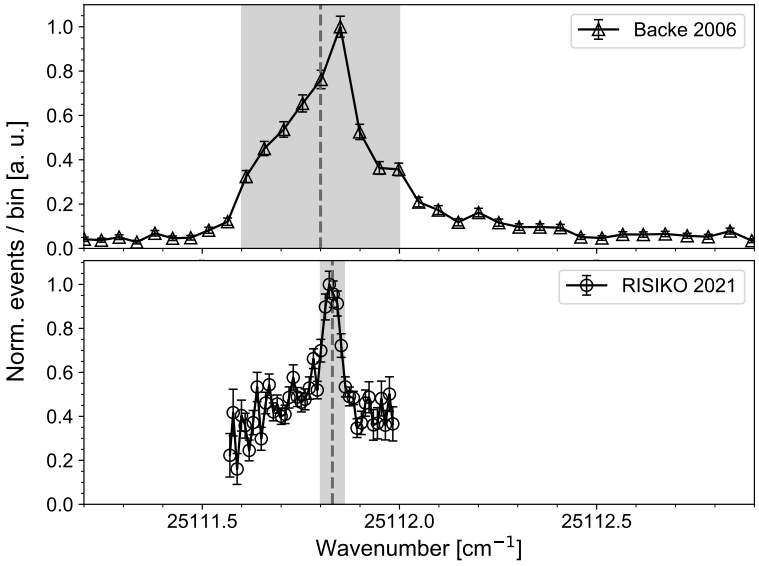

Figure 6.4.: Comparison of previous in-gas cell work on ^{255}Fm with recent narrow-band laser spectroscopy measurements at RISIKO. The data of the in-gas cell work was taken from Ref. [107]. Gray shaded bands indicate the uncertainty of the extracted resonance wavenumber.

6.3. Data collection and processing

In the RADRIS-DAQ system, resulting alpha-decay events on the PIPS detectors are recorded in dependence of the respective laser wavenumber. For the different experiments during the beamtime campaigns at GSI up until 2020 (^{248,250}Fm), in 2021 (^{249,254}Fm) and in 2022 (^{245,246}Fm, ^{251}No), different DAQ systems were used. Nonetheless, all worked in a similar manner. A very detailed description of the RADRIS-DAQ system used until 2020 is given in [155].

In all cases, Field-Programmable Gate Array (FPGA) based DAQ systems were employed to allow for a high timing resolution for instance in the registration of alpha events. Moreover, the DAQ system also handled the RADRIS cycle realization, necessitating both, precise timing and stability. Environmental parameters, including the wavelength meter readout, the gas cell pressures, the relative laser powers for stability monitoring via photodiodes, the electrode potentials, and the filament heat-pulse temperatures, were monitored and crucial parameters written to file. In the campaigns until 2020, a LabVIEW-based DAQ system was used, writing environmental parameters in 1 s intervals and alpha events in a dedicated file for the duration of a measurement. As the incoming recoil rate available for laser spectroscopy inherently depends on the production yield, the primary beam current integral on the beam dump in SHIP was continuously recorded in 1 s intervals. Beam instabilities coming from the UNILAC accelerator could thus be accounted for in the forthgoing analysis. In 2021,

this system was updated for continuous writing of alpha events beyond the duration of a single measurement. Starting from 2022, the implementation of a database enabled real-time monitoring and continuous storage of all parameters. Additionally, a LabVIEW-based user interface with backup file writing functionality was employed for controlling the RADRIS system and cycles.

Prior to conducting the analysis, a data pre-processing was undertaken, which involved identifying alpha gates around the anticipated alpha-decay signal peaks in the recorded and calibrated spectra[4]. The alpha-energy spectra obtained from RIS measurements of all performed laser scan steps were combined to ensure sufficient statistics. The resulting summed histogram, as in the example shown in Fig. 6.5 for ^{250}Fm, featured significant alpha peaks which were fit with skewed Gaussian profiles. The high-energy gate right to the alpha peak was determined as the energy at which the fit function response declined to 1 % of its maximum value. This gate was set in close proximity to the peak maximum, as the maximum energy of alpha events is sharply defined here. The low-energy edge was determined as the energy at which the fit function response declined to 0.1 % in order to consider the full tailing effect due to energy loss in the detector surface layer. The described procedure was applicable for all investigated isotopes, as there were no instances of another decay daughter isotope or similar registered with an alpha energy close to the region of interest.

The accumulated events per laser scan step, detected within the corresponding alpha gates, were subsequently correlated with the wavenumber values. Therefore, the mean value of the wavelength meter readings, obtained during the time when the shutters were opened and the laser beams transmitted to the experiment, was extracted from the recorded data. Since the wavelength meter output occasionally exhibited artefacts from side modes originating from the wavelength meter itself, these artefacts were filtered from the wavenumber data before processing.

The events that can possibly be registered from successful laser resonance ionization are most dominantly influenced by the rate of available recoil ions reaching the gas cell. Consequently, primary beam instabilities causing fluctuations in the production of the isotopes of interest have to be considered. Furthermore, the full measurement time for different laser scan steps may differ, particularly when a varying number of RADRIS cycles was required to accumulate ions on the detector for some scan steps. It is however not appropriate to normalize over the number of cycles or a measurement time. Instead, the occurrence of events depends alone on the rate of produced recoil ions and analogously the accumulated charge integral over the measurement duration. Normalizing the registered event rate to the beam charge integral in the respective time interval counteracts both these effects.

[4] A first calibration in all cases was performed prior to the on-line campaigns using a triple-alpha source, and, if available, data from the ^{225}Ac recoil source. In the analysis, the calibration was further checked with alpha-signals of several on-line studied isotopes.

For further analysis, the processed alpha events were investigated relative to the measured mean wavenumber of the laser scan step. The granularity of the data in the on-line experiments is usually coarse such that binning of the full data set is not required. If the same laser scan step was probed multiple times, such as at the expected centroid wavenumber of the resonance, the mean value of these measurements was extracted for the processed data set.

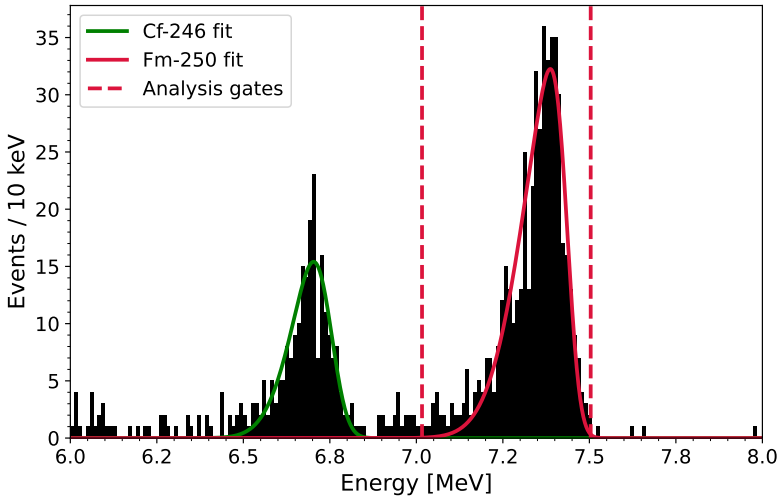

Figure 6.5.: Alpha spectrum of ^{250}Fm RIS measurements. With a skewed Gaussian profile fit to the data, alpha gates for the further analysis were determined. The energy of the alpha events from the decay daughter ^{246}Cf differs sufficiently from the isotope of interest, preventing them from reaching into the analysis gates.

6.4. Data analysis procedure

6.4.1. Fitting methodology

In the data analysis process, the observable of interest is extracted from the processed data. A best fit to the data is applied to determine the observable with an approximate confidence interval as one of the fit parameters. Of fundamental importance in the process is the choice of the right model which describes the data, along with the appropriate cost function that matches the underlying statistics the data follows. Two different cost functions were applied, depending on the experimental data and conditions. For the analysis, the Python package Lmfit with different lineshapes was utilized, such as Gaussian and Voigt-fit profiles, together with a scaled Voigt profile which will be discussed further below. In addition, the data was analyzed with the Statistical Analysis Toolbox for Laser Spectroscopy (SATLAS) package [186], also based on Lmfit, which eases treating the low count rate data sets with different minimizer methods and lineshapes.

In the fitting procedure, the model function, denoted as $f(\tilde{\nu}_i)$ with the laser wavenumber $\tilde{\nu}_i$, is optimized to best describe the original data. Through the calculation of a cost function, the discrepancy between the model and the data is iteratively minimized by adjusting the model input parameters. Two different cost functions are introduced here.

- Least-square (χ^2): this method is applied in counting experiments with sufficiently high count rates such that a normal distribution can be utilized for the distribution of events. In the fitting procedure, minimization of the χ^2 defined as

$$\chi^2 = \sum_{i=1}^{N} \left(\frac{y_i - f(\tilde{\nu}_i)}{\sigma_i}\right)^2, \tag{6.1}$$

  leads to the local best fit for the given data set and start parameters. Here, y_i is the measured event rate and σ_i the corresponding uncertainty, which in counting experiments following Poissonian statistics can be assumed to be $\sigma_i = \sqrt{y_i}$ and $\sigma_i = 1$ for $y_i = 0$ [186].

- Maximum-Likelihood calculation (mle): in experiments where the distribution of events cannot be approximated by a normal distribution but is assumed to follow a Poissonian distribution, the mle calculations are performed. This is especially crucial for low count rate experiments with small y_i. A Poissonian distribution around $f(y_i)$ is assumed and the log-likelihood is calculated as

$$L(y_i, f(\tilde{\nu})) = \sum_{i=1}^{N} y_i \cdot \log(f(\tilde{\nu})) - f(\tilde{\nu}). \tag{6.2}$$

  This property is maximized to find the best fit or, analogously, the negative log-likelihood is minimized to achieve the same result [186].

The on-line experiments in this work feature event statistics in the range of only tens of events per laser scan step or in some cases even less. Therefore, the data exhibits a pronounced Poissonian distribution character, requiring the selection of an appropriate cost functions. As a result, a maximum-likelihood fit would be the suitable choice to account for the underlying uncertainties in the data. Applying this fitting routine to the processed and normalized data necessitated the usage of a custom fit model.

To maintain the assumption of the Poissonian distribution around the data, the raw accumulated events must be given as an input for the fit procedure. To account for the fluctuating beam charge integral over the different measurements, the respective fit model function is scaled accordingly [187]. Hence, for the customized fit model, the commonly used Voigt profile is multiplied with a step function following a scaling factor accounting for the beam charge integral. The upper panel in Fig. 6.6 presents a demonstration of such a fit to the processed data with raw events of ^{254}Fm, using a maximum-likelihood routine in Lmfit. The respective Poissonian 1σ-uncertainties in the recorded events are indicated by the error bars.

After the maximum-likelihood fitting routine determined the best fit to the data, both the resulting best-fit function and the events can be re-scaled using the beam charge integral step function. The result provides the desired normalized count rate and a standard Voigt-profile fit to the data as shown in the lower panel of Fig. 6.6.

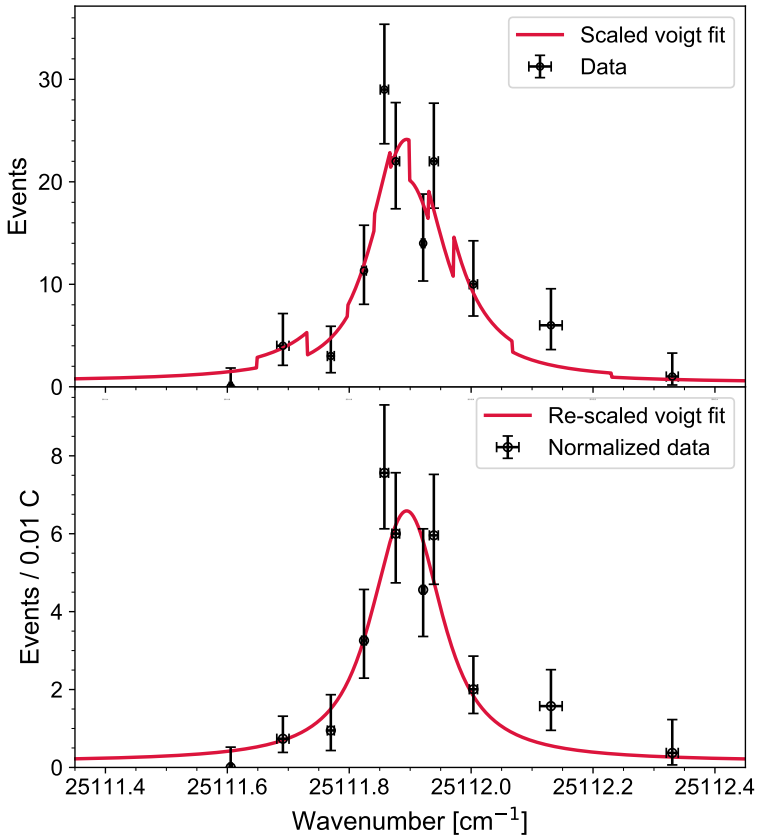

Figure 6.6.: Demonstration of the maximum-likelihood fitting procedure for ^{254}Fm. The upper panel displays the stepwise-scaled Voigt profile, compensating for the varying primary beam charge integral at each measurement point. After normalizing the registered raw event numbers and the obtained fit with the scaling function, a regular Voigt profile is obtained. An analogous routine was applied to the other on-line studied isotopes.

6.4.2. Choice of fit model functions and initial parameters

Analysis of even-even isotopes

The above described procedure was applied for all investigated isotopes studied at GSI, as they feature low count rate statistics and require the normalization to the respective beam charge integral per measurement. For the even-even isotopes ^{246}Fm,

^{248}Fm, ^{250}Fm, and ^{254}Fm, a single-line Voigt profile is suitable for the fit, as there is no underlying structure in the observed transition resonance for these spin-zero isotopes. By selecting a Voigt profile, the dominant linewidth broadening mechanisms can be considered when initial start parameters are chosen. Gaussian linewidth broadening is taken into account due to the limited laser bandwidth, as well as Doppler broadening based on the assumed thermal velocities at room temperature of the atoms. A Lorentzian linewidth broadening contribution may arise from power broadening and additionally from pressure broadening effects. The latter is the dominant cause for linewidth broadening in the in-gas cell laser spectroscopy with RADRIS.

In all narrow-band measurements conducted with the RADRIS laser system, the laser bandwidth was about 1.5 GHz. With the assumption of thermal velocities of the atoms in the gas cell, after desorption from the filament and prior to the ionization by the lasers, the Doppler broadening contribution can be estimated to 0.58 GHz by using Eq. 2.31. Both contributions add up quadratically to give a Gaussian width of approximately 1.61 GHz. Therefore, in the fitting procedure, the Gaussian contribution to the linewidth was fixed as a fit parameter as it can be well estimated.

Following the typical assumptions in Sec. 2.2.2, a pressure broadening at room temperature of at least 1 GHz has to be expected. Possible contributions due to power broadening cannot be excluded, as the saturation curve was not measured under the respective experimental conditions with the lasers and beam spot sizes used at RADRIS. Particularly in the case of ^{250}Fm, this broadening effect on the lineshape could not be disregarded in the analysis. Therefore, the Lorentzian contribution was kept as a free parameter in the Voigt-profile fit.

Due to the low statistics data in the on-line experiments, it was generally challenging to keep the background parameter, which represents a constant offset in the Voigt profile fit, unconstrained. In order to achieve convergence in the fit, it had to be fixed in some cases. To assign a reasonable value, the background measurements taken at laser wavenumbers farthest from the resonance on both sides were averaged to determine a mean background rate. In all cases, the background level was minimal, typically consisting of single events per measurement, if background events were registered at all. The scale parameter of the Voigt profile was kept as a free fit parameter.

The centroid position of the observed resonance, which is the main parameter of interest for determining the isotope shift, was naturally kept as a free parameter in the fit procedure. A proper evaluation of uncertainties arising in the analysis on this parameter are discussed with the results in Sec. 7.1.

Limitations in the analysis for odd-even isotopes

The choice of a single-line Voigt profile was discussed to be an appropriate model to fit even-even isotopes. However, it is in principle not suitable for fitting even-odd isotopes. As these isotopes feature a non-zero spin, hyperfine structure complicates

the spectrum and multiple lines in the observed transition resonance are expected. The isotopes ^{249}Fm and ^{255}Fm feature a spin of 7/2, with the spin for the former being only tentatively assigned, based on the experimental trend in the $N = 149$ isotones [188] and supported by theoretical predictions [189]. With the atomic total angular momenta of $J = 6$ and $J = 5$ of the ground state and the excited state, respectively, 21 hyperfine structure components are expected. For ^{257}Fm with a spin of 9/2, 27 hyperfine components are included. For ^{245}Fm, the spin was predicted to be 1/2 based on nuclear theory calculations and compared to systematics in the $N = 145$ isotones [190]. This only suggests three lines to appear in the hyperfine spectrum.

For the on-line studied isotopes ^{249}Fm and ^{245}Fm, the hyperfine structure could not be resolved, similarly as in the previous work on ^{255}Fm by Backe et al. [107]. Besides the limited resolution in the buffer gas environment in the RADRIS apparatus, the broadband laser arrangement with 6 GHz linewidth used for the measurement of ^{249}Fm significantly enhanced the linewidth broadening for this case.

Since no underlying hyperfine structures could be extracted, a single-line Voigt profile was fitted to the data. This is clearly an approximation that does not correspond to the appropriate choice of model, which should include hyperfine structure. This assumption however enables the extraction of the resonance centroid wavenumber as the center of gravity with sufficient accuracy. The uncertainties arising from this choice of fit model have to be considered carefully and are discussed in Sec. 7.1.

Similarly, the hot cavity laser spectroscopy measurements on the off-line studied isotopes ^{255}Fm and ^{257}Fm exhibited a Doppler linewidth broadening which did not allow resolving the hyperfine structure in the transition. From Eq. 2.31, a Gaussian linewidth contribution of 1.35 GHz for a temperature of 1600 K of the atomizer was estimated. The additional Gaussian broadening due to the finite laser bandwidth of 1 GHz for ^{257}Fm and 20 MHz for ^{255}Fm, respectively, adds to the full Gaussian width of the observed transition. The latter is dominated solely by the Doppler broadening due to the extremely small bandwidth of the single mode Ti:Sa laser used for this measurements. With the reduced laser pulse energies employed for the measurements of both isotopes, power broadening effects were assumed to be negligible compared to the dominating Gaussian linewidth broadening effects.

In summary, as no hyperfine structure could be resolved, the experimental data of isotopes studied at RISIKO were fitted with a single Gaussian profile to accommodate the dominant linewidth broadening effects and resulting shape of the observed lines. Uncertainties associated with the extracted resonance centroid wavenumber, arising from the choice of fit model, will be discussed in Sec. 7.1

7. Results

The accessible information from atomic structure investigations as performed for eight fermium isotopes is manifold and provides a comprehensive insight on nuclear ground-state properties. Results on the isotope shift measurements in the centroid of the observed transition resonance were extracted. With this experimental data, the evolution of nuclear mean-square charge radii relative to a reference isotope could be explored. The findings of these various measurements and the corresponding limitations on the extraction of nuclear structure information are compiled in the following chapter.

7.1. Isotope shift results

The results of the isotope shift measurements on all investigated fermium isotopes are shown in Fig. 7.1. Resonances of the probed atomic transition in isotopes investigated in both, off-line and on-line laser spectroscopy studies were combined. The best fits to the data utilized to extract the isotope shift results are included. The isotope shift in the atomic transition is clearly observed across the range of studied isotopes, spanning approximately 70 GHz from ^{245}Fm to ^{257}Fm. A similar representation featuring absolute transition wavenumbers for all isotopes with respective best fits to the data is included in the appendix Sec. A.3.

In the spectra of the processed data, clear differences in the width of the transition resonances are observed. In the on-line studied isotopes, similar spectral linewidths of about 4 GHz FWHM were obtained for the isotopes ^{245}Fm, ^{246}Fm, and ^{254}Fm. Comparing the spectra of ^{248}Fm and ^{250}Fm measured in the same beamtime campaign under similar conditions directly reflects the impact of power broadening on the spectral lineshape: For the measurement of ^{248}Fm, the laser power was maintained near saturation, resulting in a higher resolution measurement with a FWHM of 2.7 GHz. In the case of ^{250}Fm, the elevated laser pulse energies led to an enlarged FWHM reaching 5.2 GHz. The spectral linewidth of ^{249}Fm appears to be about four-times broader than for the other isotope and is primarily assumed to be influenced by the underlying hyperfine structure in addition to the broad-band configuration of the laser system. The spectral linewidth of the off-line measurements in the hot cavity are dominated by Doppler broadening. The additional contribution to the broadening by the laser linewidth, which is about the same size as the Doppler broadening, becomes evident in the measurement of ^{257}Fm. In general, the width of the observed resonances does

not affect the isotope shift result itself, yet the uncertainties of the fit may be enlarged for the broader resonances.

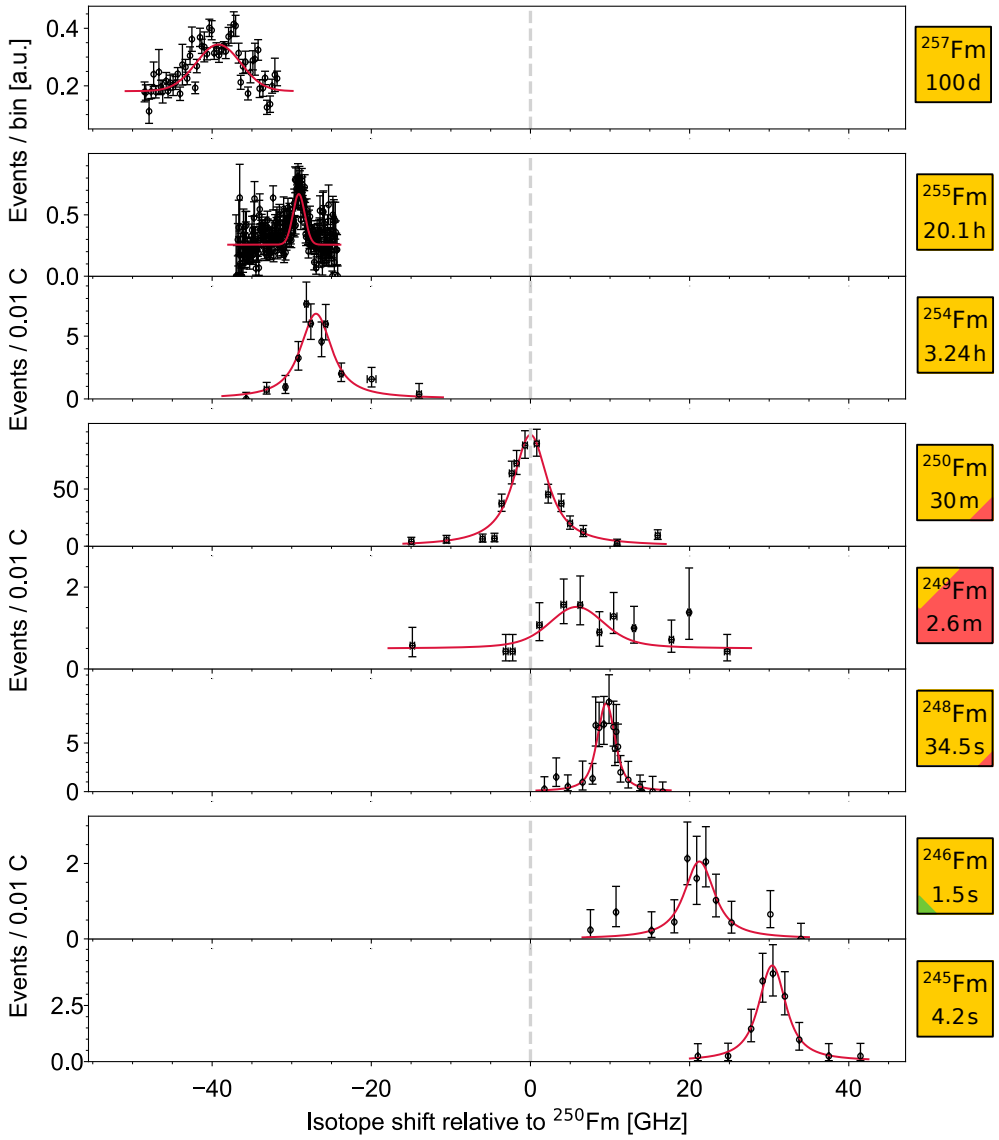

Figure 7.1.: Overview over observed RIS resonances for the measurement of isotope shifts in eight fermium isotopes. The isotope shift was determined relative to the reference isotope ^{250}Fm. Registered events from on-line experiments are normalized to the primary beam charge integral in units of 0.01 C. Results from off-line and on-line laser spectroscopy experiments were combined to provide a complete overview of isotope shift measurements. The respective best fits to the data are added with red solid lines.

The most favorable reference for isotope shift measurements in principle would be the isotope at the shell gap $N = 152$ to investigate its effect on the evolution in mean-square charge radii. With the available techniques, however, ^{252}Fm was not in reach for laser spectroscopy. Instead, the closest isotope in the chain, ^{250}Fm, was chosen as reference for all measurements. From the best fits to the experimental data the resonance center positions were extracted, as discussed in detail in Sec. 6.3. With these results, the isotope shifts in units of cm^{-1} and GHz were calculated relative to the reference isotope. The results are summarized in Tab. 7.1.

	Centroid [cm^{-1}]	$\delta\tilde{\nu}^{250,A}$[$\mathrm{cm}^{-1}$]	$\delta\nu^{250,A}$[GHz]
^{245}Fm	25 113.81(7)	1.013(73)	30.4(2.2)
^{246}Fm	25 113.50(5)	0.701(57)	21.0(1.7)
^{248}Fm	25 113.11(3)	0.317(32)	9.5(1.0)
^{249}Fm	25 112.99(10)	0.194(104)	5.8(3.1)
^{250}Fm	25 112.80(3)	0	0
^{254}Fm	25 111.90(4)	-0.899(45)	-27.0(1.4)
^{255}Fm	25 111.83(2)	-0.971(30)	-29.1(0.9)
^{257}Fm	25 111.49(7)	-1.308(77)	-39.2(2.3)

Table 7.1.: Summary of extracted absolute transition wavenumbers and derived isotope shifts relative to the reference isotope ^{250}Fm. Statistical uncertainties are given in parentheses.

Uncertainties in isotope shift

For the evaluation of the changes in nuclear mean-square charge radius, a profound analysis of the various sources of uncertainties of the isotope shift and their respective contributions has to be made. The different laser spectroscopy techniques applied here involve slightly different sources of uncertainties which need to be considered. The main contributions to the final uncertainty of the isotope shift given in units of GHz are summarized in Tab. 7.2.

In all cases, one of the primary sources of uncertainty arises from the accuracy of the chosen fit to the data. The quality of the fit, including the choice of the fitting model, the selection of fit parameters, and the determination of their uncertainties, can have a significant impact on the final results. For the fermium isotopes with mass numbers 245, 246, 248, 250, 254, a mle-fit routine was applied to better estimate the uncertainties from the underlying Poissonian counting statistics. For the isotopes 249, 255, 257, the final value was taken from a least-square fit. This approach as approximation was sufficient, as the uncertainty is strongly dominated by the choice of fit model itself. Due to the unresolved hyperfine structure and limited information on nuclear moments or hyperfine parameters, the fit could not be sufficiently constrained when including hyperfine structure components, thus prohibiting fit convergence. The fit for the odd-A isotopes therefore only allows extracting the centroid position with an increased uncertainty compared to the even-even isotopes. To account for this, a model uncertainty

of one third of the fit FWHM was included in the extracted centroid for all odd-even isotopes. Comparing the measurement results in Fig. 7.1 to the fits, it is apparent that the granularity of the data points, or scan step size, in the on-line experiments are without exception considerably wider than the centroid fit uncertainties. Therefore, the uncertainty associated with the fit itself may be considered underestimated with respect to the low statistics on-line data. Instead, to account for the low density in data points and potential limitations in the fit, an upper boundary for the uncertainty was set by assuming one third of the mean step size in the measurement. As the binning width of data points in the off-line measurements was of similar magnitude as the fit uncertainty itself, the latter was considered instead.

The absolute measurement of the laser wavenumber in the wavelength meter itself exhibits an uncertainty which has to be included. The accuracy of the employed device here is decisive. The wavelength meter HighFinesse WS7 applied for studies at GSI is expected to feature a precision of 200 MHz in the respective wavenumber range, while the absolute accuracy is stated not to be better than 20 % of the laser linewidth[1]. For the isotopes measured in narrow-band configuration, this fraction of the respective laser linewidth is assumed as uncertainty and similarly for the broad-band configuration used for ^{249}Fm. For the isotopes 255, 257, a HighFinesse WS8 wavelength meter was applied featuring a much greater precision in the wavenumber readout. Nonetheless, a similar uncertainty in the wavenumber measurement of 20 % of the laser linewidth was taken into account.

The stability of the laser wavenumber over the measurement duration of a single data point in the on-line measurements was investigated by determining the wavenumber standard deviation in the analysis. In almost all cases, no considerable drift was observed with respect to the limited accuracy of the wavelength meter readout. In these measurements, the drifts were found much smaller than the uncertainty from the fit itself. Only in the case of the long-lived isotope ^{254}Fm, the effect of wavenumber drifts was observed due to the extended measurement time of more than 8 h per data point. To address this concern of wavenumber drifts at a certain measurement point to affect the final fit result, a bootstrapping method was employed. This involved generating a random set of wavenumber values within the 1σ-standard deviation interval around one individual data point. For each of these randomly generated wavenumber values, a fit to the data was performed and the fit result on the centroid stored. After iteratively performing this procedure, a distribution of fit centroid wavenumbers is created from which an uncertainty can be estimated. Similarly as for the other isotopes, the uncertainty in the fit was found smaller in comparison to the general assumed uncertainty due to the coarse granularity discussed previously.

[1]Information on the respective wavelength meter devices are summarized in a data sheet supplied by the manufacturer HighFinesse and can be found at https://www.highfinesse.com/en/wavelengthmeter/wavelengthmeter-further-information/product-overview-wavelengthmeter-ws-series.pdf, last access July 5, 2023.

Another source of uncertainty arises due to the pressure shift in the gas cell and the Doppler shift in the hot cavity, which can be assumed to be of the same order of magnitude and estimated to be maximum 0.4 GHz. For all isotopes studied in the same respective environment, the systematic shift is the same. The systematic shift can be neglected for the isotope shift uncertainties of all on-line studied isotopes, as they exhibit the same pressure shift as the reference isotope ^{250}Fm. The respective shift on the contrary needs to be considered for the off-line studied isotopes such that it remains included in the total uncertainty for ^{255,257}Fm.

Uncertainty [GHz] / Isotope	245	246	248	249	250	254	255	257
Centroid fit	0.35	0.45	0.15	1.35	0.16	0.28	0.06	0.27
Measurement granularity	1.50	1.50	0.45	0.45	0.45	1.05	/	/
Model uncertainty	1.35	/	/	2.74	/	/	0.58	2.17
Wavenumber measurement	0.4	0.4	0.4	0.4	0.4	0.4	/	/
Pressure & Doppler shift	/	/	/	/	/	/	0.4	0.4

Table 7.2.: Individual contributions to uncertainties in the extracted isotope shifts in fermium relative to ^{250}Fm. Summarized are the different effects considered for each isotope leading to the total uncertainty in the isotope shift.

7.2. Extracted changes in mean-square charge radius

With the predicted field shift constant from atomic calculations [99], values for $\delta\langle r^2\rangle^{250,A}$ were calculated from the results on isotope shifts using Eq. 3.2. With the reference isotope ^{250}Fm regarded for the extraction of the isotope shifts, the evolution of mean-square charge radii in the vicinity of the $N = 152$ shell gap was investigated. The results are summarized in Tab. 7.3.

	$\delta\nu^{250,A}$[GHz]	$\delta\langle r^2\rangle^{250,A}$[fm^2]	
	Isotope shift	Experimental data	spherical DM
^{245}Fm	30.4(2.2)	-0.323(23)[32]	-0.279
^{246}Fm	21.0(1.7)	-0.223(19)[23]	-0.223
^{248}Fm	9.5(1.0)	-0.101(10)[10]	-0.111
^{249}Fm	5.8(3.1)	-0.062(33)[6]	-0.055
^{250}Fm	0	0	0
^{254}Fm	-27.0(1.4)	0.286(15)[29]	0.220
^{255}Fm	-29.1(0.9)	0.309(10)[31]	0.275
^{257}Fm	-39.2(2.3)	0.415(26)[43]	0.383

Table 7.3.: Summary of experimental results. Values for $\delta\langle r^2\rangle$ were evaluated from the measured isotope shifts. Statistical uncertainties are noted in parentheses, the systematic uncertainties due to the limited accuracy of atomic theory predictions are presented in brackets. Predictions of the spherical DM are included for comparison with the experimental data.

Uncertainties in changes in mean-square charge radius

The uncertainty in the extracted changes in mean-square charge radii are mostly dominated by the absolute isotope shift uncertainty discussed previously. Within this analysis procedure, this is the only contribution to the statistical uncertainty for $\delta\langle r^2\rangle$. However, the systematic uncertainty arising from the limited accuracy of the atomic theory prediction of the field shift constant needs to be included as additional source.

At first, for the predicted field shift factor F_{FS}, an accuracy on the 10 % level is considered, such that an uncertainty of $\Delta F_{\mathrm{FS}} = 0.314\,\mathrm{cm}^{-1}/\mathrm{fm}^2$ is included in the evaluation. The mass shift itself was assumed as zero in the calculations on the change in mean-square charge radius. However, an additional contribution to the overall uncertainty based on this assumption is included. In principle, the NMS as described in Sec. 2.2.5 can be calculated to be approximately $K_{\mathrm{NMS}} \approx 0.4\,\mathrm{THz{\cdot}u}$. For s-p-transitions, such as this case in fermium, it is expected to be of the same order of magnitude as the SMS. To provide a conservative estimate of the uncertainty resulting from the zero-assumption on the mass shift, a five times larger systematic uncertainty contribution is considered with $\Delta K_{\mathrm{MS}} = 2.0\,\mathrm{THz{\cdot}u}$.

Both these systematic error contributions combined yield a total systematic uncertainty indicated by the blue band in Fig. 7.2. The systematic uncertainties increase for isotopes further away from the reference ^{250}Fm and, in principle, they feature a change in sign across the reference isotope in the chain. While the overall trend may be flattened or steepened in the extreme cases within these uncertainties, the trend from one isotope to another remains unaffected.

Results on the mean-square charge radius evolution

The experimental results are visualized in Fig. 7.2 with error bars showing statistical uncertainties. The blue shaded band around the data points represents the referred systematic uncertainties. The data is complemented with predictions by the spherical DM [31] with values calculated using the second parametrization given in Ref. [58]. A more detailed description of the DM calculations presented here is included in the appendix in Sec. A.4.

A constant deformation may be included in the DM predictions in a heuristic approach using the approximation given in Eq. 2.12, here considered up to the second order β_2 and with the predictions from the spherical droplet model $\langle r^2\rangle_{\mathrm{sph}}$ [17]. The mean-square deformation parameter $\langle\beta_2^2\rangle$ can be divided into $\langle\beta_2^2\rangle = \beta_{2,\mathrm{static}}^2 + \beta_{2,\mathrm{dynamic}}^2$, a dynamic and static nature of the deformation [191]. For comparison here, we assume a full static and constant deformation of approximately $\beta_2 = 0.3$, which is predicted for fermium isotopes around the shell gap [192]. Comparing the spherical and deformed DM predictions in Fig. 7.2, both show similar trends, the deformed model with a slightly larger increment. The deviations between both however remain smaller than the uncertainties in the experimental data for the respective neutron number. For

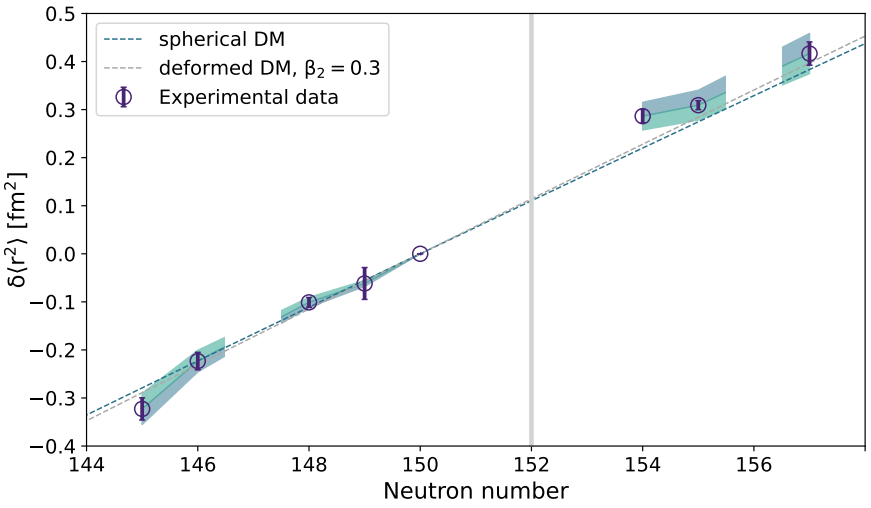

Figure 7.2.: Evolution of mscr in fermium in dependence of the neutron number. Changes in mean-square charge radius were calculated relative to ^{250}Fm. Statistical uncertainties are shown with error bars around the data points. Systematic uncertainties due to the limited accuracy of the predicted atomic parameters are presented with the blue shaded band. Calculated trends from the spherical DM and considering a deformation of $\beta_2 = 0.3$ are included.

further comparison with the experimental data, the predictions from the spherical DM are considered without including the purely phenomenological contribution of deformation.

In a first comparison of the experimental results with the predictions of the model, a good agreement between both is found, and the trend in size increase seems to be captured by the spherical DM. For a further interpretation, the extracted results on $\delta\langle r^2\rangle$ will be discussed and interpreted with respect to various nuclear model predictions in the following chapter.

8. Interpretation and Discussion

The isotope shift data in combination with additional input from atomic theory allowed exploring the evolution of nuclear mean-square charge radii in the vicinity of the $N = 152$ shell gap. For a further in-depth analysis of the results, a comparison with state-of-the-art nuclear models is valuable to facilitate the interpretation of the data. Not only does this enable benchmarking the predictive power of the models for these heavy, very complex systems. It also may provide a deeper understanding into underlying nuclear structural effects, given that the models take different effects on the single-particle level into account. With the additional perspective from nuclear models, the new data can be compared to existing studies around other deformed shell gaps to give an enhanced comprehension of their impact on nuclear observables.

8.1. Comparison of experimental results to state-of-the-art nuclear models

A direct comparison of the experimental data with the DM predictions, as shown in Fig. 7.2, is useful to compare trends in the mean-square charge radii. For a more quantitative comparison, it is beneficial to regard absolute deviations between the two. The spherical DM predicts a trend approximately increasing linearly with $A^{1/3}$ for higher masses. Subtracting this linear trend from the data can help highlighting variations between both more effectively. Such residual changes in $\langle r^2 \rangle$ relative to the DM predictions were calculated. The result is shown in Fig. 8.1 in the upper panel a).

In this representation, an overall good agreement between the experimental data and the DM predictions is observed. Particularly, the calculations for the neutron-deficient isotopes below $N = 152$, the even-even isotopes ^{246,248,250}Fm and ^{249}Fm, albeit with a relatively significant uncertainty, are well reflecting the data. The lightest investigated isotope ^{245}Fm deviates towards a smaller mean-square charge radius. This trend can be explained with an expected decrease in deformation with increasing difference from the shell gap, where the deformation is maximal [15]. The data on the neutron-rich isotopes ^{254,255,257}Fm all indicate a larger nuclear size than predicted. Furthermore, a considerable staggering can be observed between the even-even isotope ^{254}Fm and the even-odd neighbor. A small discontinuity in the trend of the mean-square charge radii nearby the shell gap is seen between the neutron-deficient and neutron-rich isotopes with relatively larger radii. For ^{254}Fm, this deviation from the DM model amounts to $0.066\,\mathrm{fm}^2$. To pin down the exact location and type of a potential discontinuity,

however, additional experimental information at the shell gap, such as for ^{252}Fm and its direct neighbors, would be required. Based on the available data, there is no indication of a kink in the nuclear size evolution, as the overall trend remains consistent when comparing neutron-deficient and neutron-rich isotopes. The observed difference lies in an offset between the data and the model. A comparison to more sophisticated state-of-the-art nuclear model predictions is required to understand the agreement between the data and the predominantly macroscopic DM model, and thus the importance of shell effects acting on charge radii around $N = 152$.

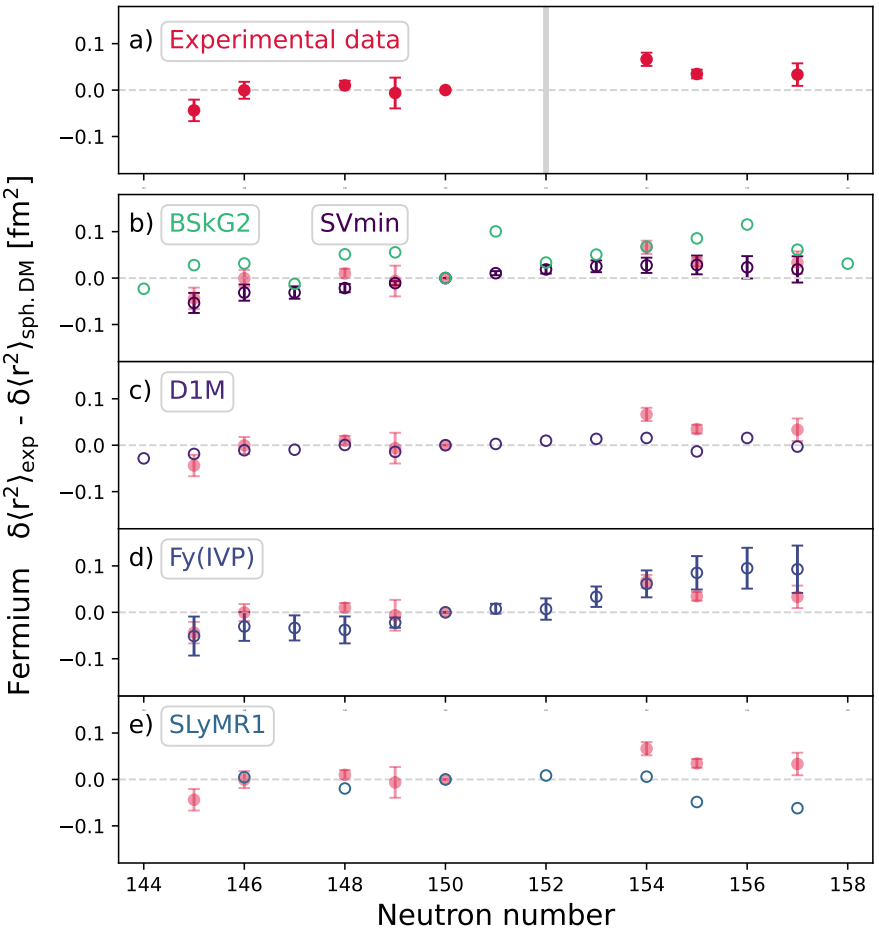

Figure 8.1.: Residual changes in mean-square charge radii relative to the trend of spherical droplet model predictions. The upper panel shows the experimental data with statistical uncertainties on relative changes in $\langle r^2 \rangle$. The four lower panels show predictions by different nuclear models. For a better comparison, the experimental data in opaque shade is included in the model panels.

Predictions from a variety of EDF-based model approaches were made available for comparison to the experimental data in this work[1]. The various calculations all ground in symmetry-broken HFB frameworks, allowing to account for the microscopic description of single-particle structure effects and the influence of deformation. The available models can be divided into subgroups of three types: calculations were carried out using the Skyrme-type functionals SV-min [65], BSkG2 [66], and SLyMR1 [67], the Fayans-type functional Fy(IVP) [193], and the Gogny-type D1M functional [71].

The functionals SV-min and BSkG2 are built as common Skyrme-types and feature a density dependence in the pairing term. While the SV-min approach relies on a single-reference, the latter incorporates phenomenological corrections towards a beyond-mean field description and considers triaxiality. In the SLyMR1 functional, the common density dependence is substituted by a direct three-body interaction. It was applied for MREDF calculations and includes configuration-mixing and the restoration of particle number and angular-momentum symmetries [194]. Similarly as for BSkG2, the D1M Gogny-type functional integrates corrections towards a beyond mean-field approach, the Fy(IVP) Fayans-type functional is alike SV-min based on a single-reference approach.

Tuning of all nuclear models was done using experimental data on nuclear ground-state properties, however different sets of data were used for optimization. For the functionals D1M and BSkG2, a large, global variety of nuclei were considered to fit the models to hundreds of experimental data of nuclear charge radii and thousands of experimental mass values. Finite and specifically selected sets of experimental data on the contrary were applied to tune the SV-min, Fy(IVP) and SLyMR1 functionals, respectively. Statistical uncertainties resulting from the calibration process could be extracted for the SV-min and Fy(IVP) models. The uncertainties on predicted changes in mean-square charge radii increase with the distance to the reference isotope ^{250}Fm. Similar uncertainties can be expected for all model predictions.

The results from nuclear calculations applying these different approaches are shown in Fig. 8.1 in panels b)-e). For a better comparison to the experimental data, the same linear trend from DM calculations is subtracted in this representation. The experimental results are included in each panel as half-transparent data points. Available information on statistical uncertainties of the models are included with error bars.

Within the assumed uncertainties of the individual models, a good agreement with the experimental data is evident, particularly for the neutron-deficient isotopes. On the other side, the trends of all models tend to deviate more from the data after crossing the shell gap. Nonetheless, most models are still in agreement with the experimental data within the given uncertainties. The observed localized enhancement in mean-square charge radius for ^{254}Fm is best captured by the Fy(IVP) model, which generally

[1]The results of shown calculations were made available by -personal data removed in online version- and are greatly acknowledged for the interpretation of the experimental data. More information on the respective model frameworks and calculations will be compiled in an upcoming publication [171].

features a steeper increase over the isotopic chain. This may be explained by the reduction in the pairing correlations in the vicinity of the shell gap at $N = 152$ [195]. For the more neutron-rich nuclei however, this model over-predicts the experimental trend. The size evolution between the neutron-rich isotopes is reflected by the SV-min, D1M and SLyMR1 approaches. The latter two methods also capture the observed odd-even staggering, yet with a larger offset of more than $0.05\,\mathrm{fm}^2$ compared to the experimental data.

In general, the experimental data was found in accordance with the EDF-model predictions, as well was the models among themselves. The observed smooth trend, consistent with the heuristic DM calculations, can be explained by bulk properties which strongly dominate the charge radius evolution in heavy nuclei. On the contrary, the impact of shell effects arising from the microscopic single-particle structure appears to be reduced in this observable. This shell gap at $Z = 100$ and $N = 152$, in the region of the heaviest actinide nuclei with strong deformation, is smaller and less localized compared to spherical shell gaps in lighter nuclei [5, 196]. At the well-localized spherical shell gaps in lighter and medium heavy nuclei up to $N = 126$, for instance for ^{208}Pb [24], kinks in the mean-square charge radius are observed as indicator of the impact of the neutron shell gap.

With the obtained results, a first insight into the evolution of mean-square charge radii on both sides of the $N = 152$ shell gap was achieved. Further valuable insight on the effect of the deformed shell gap on this observable can be gained by investigating the nuclear size evolution in neighboring isotopic chains. This allows exploring the localization of observed effects, in particularly of the small but constant enhancement in nuclear size across the shell gap, and probes its re-occurrence in isotopic chains away from the $Z = 100$ shell gap. Therefore, the experimental data from this study was combined with literature values from other actinide chains to evaluate potential similarities.

8.2. Mean-square charge radius evolution in the actinide elements

The presented study on fermium represents the longest chain of isotopes for which data on the charge radius evolution across the $N = 152$ shell gap is currently available. Recent laser spectroscopy investigations on neutron-rich californium isotopes have provided isotope shift data over a chain of five isotopes crossing the shell gap. Yet, missing information on atomic parameters from theory does not allow to asses the changes in mean-square charge radii [29]. Similarly, such information could not yet be extracted from laser spectroscopy studies of einsteinium [179]. Isotope shift measurements have not been conducted for the lighter actinides protactinium, neptunium, and berkelium ($Z = 91, 93$, and 97), as laser spectroscopy was only performed on only one single respective isotope or the data is not yet available to date. In the heavy

actinide elements mendelevium and lawrencium ($Z = 101$ and 103), no experimental information on atomic levels is presently available to allow for studies of this kind.

The data in this work is compared to available literature data on experimental changes in mean-square charge radii of other actinide elements between $N = 136-157$, as shown in Fig. 8.2. In panel a), $\delta\langle r^2\rangle$ values are shown for actinide elements with even proton numbers with circles, for odd proton numbers with squares. The different isotopic chains exhibit an offset in this representation as different reference isotopes had to be chosen. For a direct comparison of the experimental trends in the various chains, no common reference neutron number could be identified in the available data [2]. In panel b), residual values $\delta\langle r^2\rangle$, with the trend of the spherical DM subtracted from the experimental data, are shown. For each individual isotopic chains, spherical DM predictions for the respective chain were calculated and subtracted from the literature values.

As the available literature data does not include any actinide isotopic chain crossing the shell gap, a comparison of trends among neutron-rich isotopes with the fermium data is currently not possible. In the representation shown in Fig. 8.2 b), an increasing deviation from the DM predictions emerges as the neutron number decreases relative to the shell gap. Particularly in the case of the lightest actinide elements, the variations in $\delta\langle r^2\rangle$ exhibit a distinct trend towards smaller relative charge radii for neutron-deficient isotopes. In contrast, the size evolution for the heavier actinide elements remains rather constant, and consistent with the DM, as previously discussed for fermium and also for nobelium.

This changing trend in the mean-square charge radius evolution can be attributed to a varying deformation in this region. With the relation given in Eq. 2.12 and equations given in Sec. 2.1.5, $\langle r^2\rangle$ can be related to the quadrupole deformation parameter β_2 and consequently to the intrinsic quadrupole moment Q_0. A decreasing deformation therefore leads to a relatively smaller mean-square charge radius. Available literature data on the electric quadrupole moment, ranging from the lanthanide elements to the actinide elements between $Z = 57 - 102$ and $N = 82 - 156$, are shown in Fig. 8.3 as a function of neutron number.

As the spherical shell closure at $N = 126$ (or $N = 82$) (solid gray lines) are approached, the quadrupole moments of the respective isotopes are observed to be small and close to zero, reflecting little to no deformation. Near the magic shell gap at $N = 126$, only few valence nucleons can contribute and hence lead to small quadrupole moments. With increasing distance from this shell gap, the collective motion as correlations and excitation of several valence nucleons contributes to large quadrupole moments and an increased deformation [26].

[2] The neutron numbers of respective reference isotopes are: $N = 140$ for actinium, $N = 142$ for thorium, $N = 144$ for uranium, $N = 146$ for plutonium and americium, $N = 148$ for curium, and $N = 150$ for fermium and nobelium.

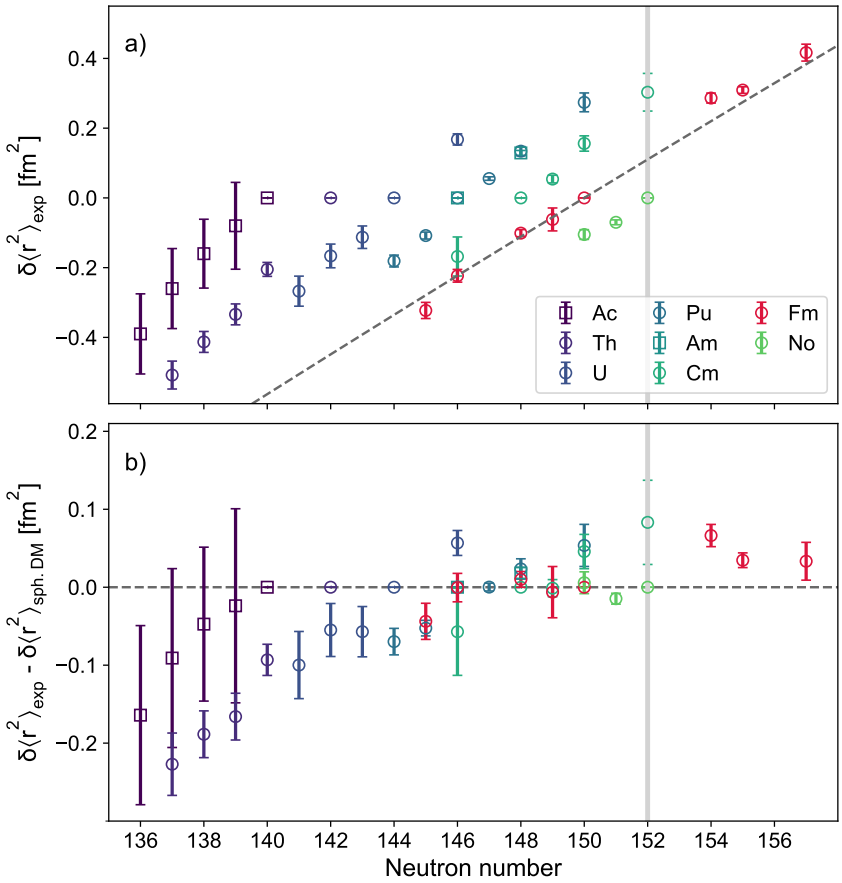

Figure 8.2.: Changes in mean-square charge radii in actinide elements known from literature [28, 154, 197, 198, 199, 200, 201] in comparison to results from this work. The upper panel a) shows the respective evolution in mean-square charge radii for the different isotopic chains. Predictions from the spherical DM for fermium are shown with a gray dashed line with reference $N = 150$. Panel b) shows residual changes in mean-square charge radius relative to predictions by the spherical DM. Isotopic chains with even proton number are visualized with circles, these with odd proton numbers with squares. More information is found in the text.

After crossing the spherical shell gap towards heavier nuclei, a small but rapidly increasing prolate deformation is observed from the lighter to the heavier actinide nuclei. This explains the relatively smaller nuclear size of the lighter actinide isotopes, similarly as for ^{245}Fm, which deviate from the spherical DM calculations. As $N = 152$ is approached, a stable, prolate deformation is seen, with the maximum suggested at the shell gap [15]. The size increase in the vicinity of the shell gap is thus not affected by an increasing deformation. Therefore, the better agreement of the fermium data, similarly as in nobelium, with the spherical DM can again be understood.

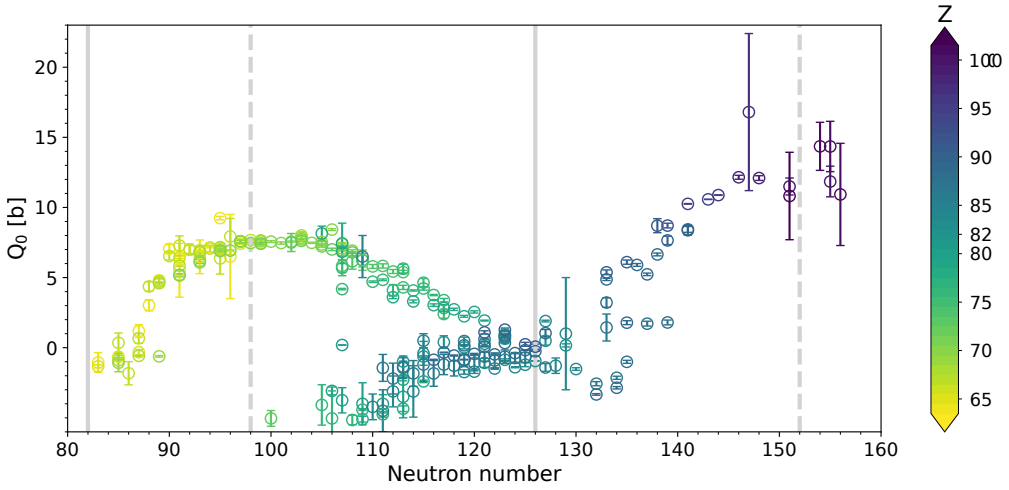

Figure 8.3.: Intrinsic electric quadrupole moments of heavy elements around the spherical shell gap at $N = 126$ (solid line) and the shell gaps in regions of strong prolate deformation at $N = 98$ and $N = 152$ (dashed lines). The color coding refers to the respective Z of the shown isotopic chains. Data taken from literature [28, 197, 198, 199, 202, 179, 29].

8.3. Influence of other known shell gaps in lighter deformed nuclei

Besides the $N = 152$ shell gap in a region of strong deformation, other sizable shell gaps in regions of deformed, lighter nuclei were identified around $N = 40$ and around $N = 98$. For a comparison of the impact of shell gaps, particularly in view of the different locations on the nuclear landscape, available data from literature on mean-square charge radii is compared to the findings in this work.

The shell gap at $N = 40$ is well established from the trend in $E(2^+)$-energies in the nickel ($Z = 28$) chain around the "magic" ^{68}Ni nucleus [7]. It was however seen to be a localized effect compared to neighboring isotopic chains with even proton numbers as in iron and zinc ($Z = 26, 30$). An effect of this shell gap was also seen in the trends of other observables as in nuclear masses [19, 203, 204]. Laser spectroscopy studies have unveiled a local minimum in the residual mean-square charge radii after subtracting the predicted trend by the spherical DM, analogously to the approach in Fig. 8.1[3]. This subtle effect of the shell gap was found as localized phenomenon in the nickel and neighboring copper ($Z = 29$) chain, but disappeared in the zinc isotopic chain as suggested before. A presentation of respective literature data is shown in Fig. A.6 a) in the appendix. Here, a pronounced disagreement is found for the data of these two chains compared to the DM predictions. In the available data on fermium on the contrary, no such hint on a similar effect around the shell gap is

[3]Note in the data presented in Fig. 8.1 it is the residual changes in mean-square charge radii after subtracting the spherical DM predictions.

reflected. This comparison showcases the dominating single-particle structure in the lighter nickel region on the contrary to the dominating macroscopic regime interpreted for the heavy region around fermium.

As this lighter region is very distant with close to 200 mass numbers difference from the heavy actinide region, a more appropriate comparison may be drawn with a closer deformed shell gap, such as around $N = 98$. Evidence for this shell gap was found in ^{160,162}Eu (europium, $Z = 64$), featuring the proton mid-shell [10], whereas further studies also suggest the location of a deformed shell gap at $N = 100$ [205, 206][4]. A minimum in the $E(2^+)$-energies and observations from further in-beam gamma-spectroscopy studies hinted on a maximum deformation for $N = 98$ isotones near the (deformed) proton shell gap at $Z = 60$ [12]. Isotopes located near both, the proton and neutron shell gaps are far from stability, and their challenging production generally sets limitations to conducting detailed experimental studies on nuclear ground-state properties. Investigations with laser spectroscopy in this region are therefore hampered.

As of now, data regarding the nuclear size evolution across this neutron shell gap are available only for the elements thulium ($Z = 69$) to hafnium ($Z = 72$). In Fig. A.6 b) in the appendix, a similar representation of residual changes in mean-square charge radius relative to DM predictions are shown for available literature values. No subtle effect corresponding to the expectations from the nickel chain could be identified in this region. Nevertheless, a shell gap effect in the charge radii could be a similarly localized phenomenon. To explore if the deformed neutron shell gap features a characteristic effect on the nuclear size, additional experimental studies in isotopic chains combining the vicinity of the proton shell gap would be valuable.

Contrary to this shell gap in the rare-earth elements, the shell gap at $N = 152$ is well established as it was introduced in Chap. 3 and its effect was quantified in many nuclear observables such as Q_α-values [16], $E(2^+)$ energies [15] and nuclear masses [13]. An effect of this deformed shell gap is revealed in literature values on the two-neutron shell gap parameter as presented in Fig. 8.4. Here, the impact on this quantity is shown to be a factor of four reduced compared to the spherical shell gap at $N = 126$. The insets in the figure provide a more detailed view at the regions around the two deformed shell gaps at $N = 98$, with neighboring isotopic chains to the proton shell gap at $Z = 60$, and $N = 152$ around $Z = 100$. Whereas an enhancement in the shell gap parameter is evident at the deformed shell gap in the actinides of close to 1000 keV, no clear signature of a shell effect of a comparable size can be isolated for $N = 98$ and a shell effect seems reduced in this observable.

In summary, the heavy deformed region around $N = 152$ stands out in comparison to lighter deformed regions featuring sizable shell gaps. The actinide region provides an ideal framework to study the extremes in the effect of deformed shell gaps on

[4] Recent experimental studies on β-decay half-lives [207] and mass measurements in the the rare-earth elements [208] could not confirm the location of a deformed shell gap at $N = 100$.

nuclear ground-state properties, which are less understood than those of spherical ones. Recent experimental advancements, also described in this work, have given experimental access for more laser spectroscopy studies in this region, whereas similar studies around $N = 98$ remain hampered by production capabilities. The presence of strong shell effects in nuclear structure properties in the heavy actinide region was previously confirmed [15, 13]. A surprisingly smooth trend was observed in the nuclear size increase in fermium isotopes across the $N = 152$ shell gap. This is in contrast to the subtle effects of the shell gap seen around the lighter $N = 40$ shell gap, and confirmed shell effects on other observables around $N = 152$.

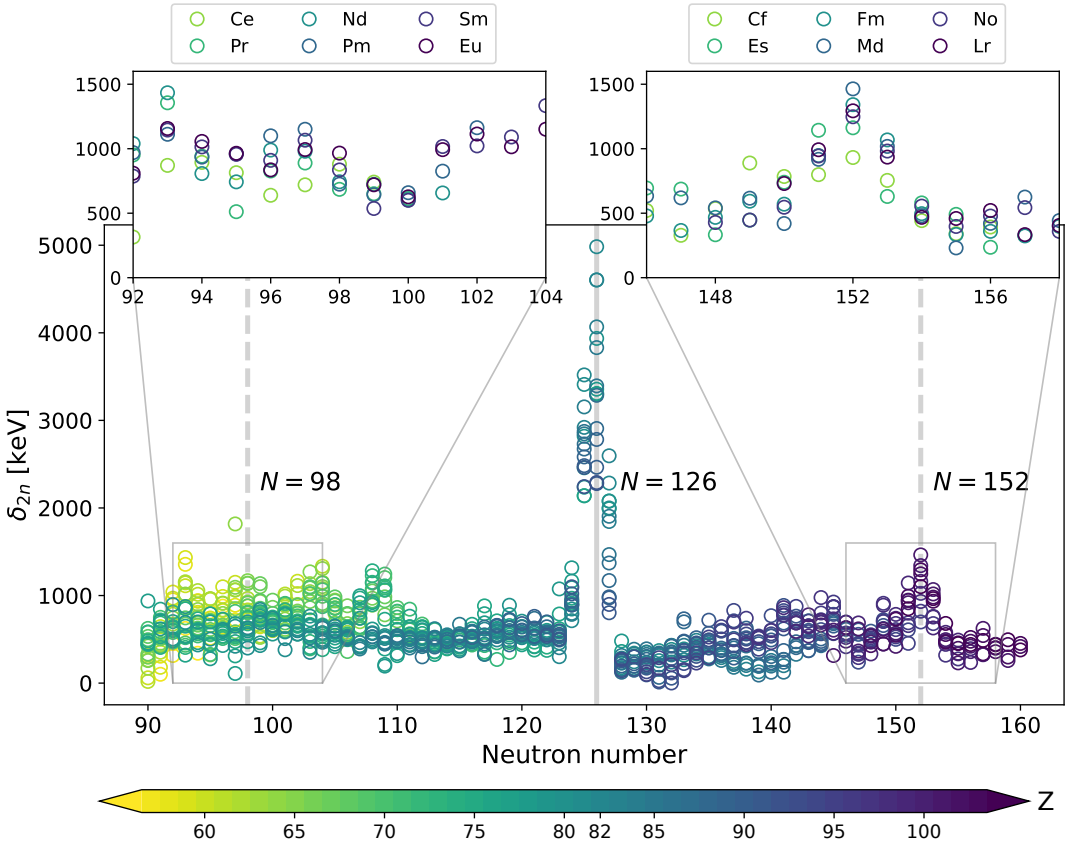

Figure 8.4.: Neutron shell gap parameter in the lanthanide to actinide region. The insets show the shell gaps at $N = 98$ and $N = 152$ in regions of strong prolate deformation with isotopic chains in the vicinity of the proton shell gaps $Z = 60$ and 100. The spherical shell gap at $N = 126$ is crossed between these two regions. Values taken from the recent Atomic Mass Evaluation 2020 [108].

9. Conclusions and Outlook

In this work, laser spectroscopy studies were performed on eight fermium isotopes on either side of the known $N = 152$ shell gap in a region of strong prolate deformation. The combination of different production mechanisms and laser spectroscopy techniques, along with methodological advancements, gave access to isotopes that were previously not in reach.

The isotope shift measurements combined with new calculations from atomic theory [99] facilitated the extraction of changes in the mean-square charge radius for a chain of isotopes ranging from ^{245}Fm to ^{257}Fm. The experimental data was compared to results of different nuclear mean-field models applying a variety of methods and energy density functionals. All considered models were found to be in good agreement with the data, considering the uncertainties of the respective calculations. Furthermore, both, the experimental observations and state-of-the-art model predictions followed the trend obtained by the heuristic spherical droplet model. The investigated complex and heavy nuclei, featuring a large number of nucleons, were therefore well described by the various models applying a mean-field approximation. This highlights the dominant influence of macroscopic bulk properties on the nuclear size evolution across the shell gap, as opposed to the single-particle structural effects at known spherical shell gaps $N = 28, 50, 82, 126$, as for instance the prominent kink. A small discontinuity in the available experimental data was observed after crossing the shell gap but could not be further explored by the nuclear models at the present level of uncertainties.

To investigate this further, additional experimental data in the vicinity of the shell gap, particularly for ^{252}Fm, is essential. The access to this isotope, however, is limited as it cannot be produced in common cold-fusion reactions of stable beam-target combinations [109]. Alternatively, using the indirect production method applied in this work and described in more detail in Refs. [165, 166], new production schemes can be developed. An indirect production via the nobelium isotope ^{256}No ($t_{1/2} = 2.9\,\mathrm{s}$) transforming to ^{252}Fm via alpha decay with a 99.5 % branching ratio [209] could be applied. The mother nuclide can be obtained through the fusion-evaporation reaction ^{238}U(^{22}Ne, 4n)^{256}No with a cross section of approximately 45 nb [210]. Experimental challenges may arise through the lower transmission by SHIP of only about 3 % for such asymmetric reactions [146] and the low recoil energy. These factors lead to reduced yields, requiring further adjustments to the setup. Nonetheless, with the recent advancements aimed at enhancing the overall efficiency of RADRIS and an expected high neon-beam flux provided by the UNILAC accelerator, an indirect production of ^{252}Fm comes in reach.

A major challenge for a study of this isotope with the RADRIS technique lies in the long half-life of $t_{1/2} = 25.4\,\mathrm{h}$ [211], which poses challenges for the decay-based detection method. Present development work focuses on an extension of the rotatable multi-detector setup demonstrated in this work for ^{254}Fm to study such long-lived isotopes. The adaption towards an eight-fold linear movable array of PIPS detectors is currently under construction. This modification aims to parallelize the collection and measurement times on all detectors, enabling studies of isotopes with half-lives in the range of few tens of hours. Future prospects for a combination of an ion extraction extension with a mass filter unit, integrated into the existing RADRIS technique, will enable a detection based on selective single-ion counting and, consequently, eliminate limitations for longer-lived species.

Moreover, an extension of the studied fermium isotopic chain would could give a more detailed view on the occurrence of single particle structural effects in the charge size evolution, for instance contained in OES. The achieved resolution of few GHz for the even-even isotopes in this work was sufficient to reveal staggering effects, however, an increased resolution would allow for a more precise quantification of the staggering, particularly for the even-odd isotopes. The first successful application of the RADRIS method to the short-lived isotope ^{251}No, facilitated by to the short-cycle implementation and improvements in the overall efficiency, creates the possibility of the indirect production of ^{247}Fm via the alpha decay of the former. The case of ^{247}Fm ($t_{1/2} = 31\,\mathrm{s}$) is particularly intriguing as it presents the opportunity for laser spectroscopy of both, the ground state and the isomeric state. These states can be well differentiated by their alpha energy, making it possible to extract first information on the change in nuclear size between both with RADRIS. Further neutron deficient isotopes as, e.g., ^{243,244}Fm can practically be directly produced with cross sections of few nb [140]. However, the short lifetime of these isotopes with $t_{1/2} = 231\,\mathrm{ms}$ and $t_{1/2} = 3.12\,\mathrm{ms}$ [140] do not allow for an application of the RADRIS technique due to inevitable decay losses. Alternative techniques, possibly with an increased resolution, have to be considered.

As a next step, it would be highly interesting to investigate the nuclear magnetic dipole moments and electric quadrupole moments of the accessible non-spin zero isotopes. Experimental data on nuclear moments, extracted from atomic hyperfine structures, would serve as a benchmark test for nuclear models, particularly for their predictive capabilities for odd-mass number nuclei. The study of quadrupole moments offers a more in-depth exploration of the evolution of deformation and the collective nature in the vicinity of the shell gap. The magnetic moment can yield insight into the occupation of underlying single-particle orbitals by the unpaired nucleon and arising collective motion. Furthermore, a resolution of hyperfine structure would enable to unambiguously assess the nuclear spins especially for the neutron-deficient even-odd isotopes, which remain only tentatively assigned. However, due to the limited spectral resolution of the in-gas cell method, the extraction of hyperfine structure components was not achievable.

The recent establishment of the in-gas jet laser spectroscopy technique has enabled hyperfine spectroscopy and the extraction of nuclear moments in exotic actinium isotopes with a ten-fold improved resolution of 400 MHz compared to resolution achieved with the RADRIS technique [198, 212]. Following on this success, the combination of the in-gas jet technique and the filament neutralization of fusion-evaporation products was recently implemented in the JetRIS setup [212, 213]. This setup was tailored for the application to the heaviest actinide elements at SHIP. Thanks to the improved resolution provided by this technique, the extraction of nuclear moments of odd-even fermium isotopes such as the investigated ones ^{245,249}Fm becomes possible. In the JetRIS setup, both, decay-based detection as well as single-ion detection are available options. The short extraction time of few hundred milliseconds additionally gives prospects for the study of shorter-lived isotopes and isomers. Current efforts are directed towards coupling of this apparatus with a Multi-Reflection Time-Of-Flight Mass Spectrograph (MRTOF-MS), allowing for an unambiguous and sensitive detection of isotopes regardless of their decay mode and (longer) half-life. With future development work aimed at improving the efficiency to the level of RADRIS, the study of ^{252}Fm with JetRIS may become possible.

The recent demonstrations of high-resolution laser spectroscopy studies in the actinide elements einsteinium and californium at RISIKO, using samples from reactor breeding down to $5 \cdot 10^7$ atoms [179, 29], opened pathways for similar studies in ^{255,257}Fm. The implementation of the PI-LIST [180] at RISIKO enabled an arrangement of the laser and atom beams in perpendicular geometry and therefore a significant reduction in Doppler broadening. With this technique, spectral linewidths on the order of a few hundred MHz have been achieved allowing to extract nuclear structure information from the broad hyperfine structures found in actinide atomic structures. Until recently, additional off-line studies on ^{255}Fm, involving sample sizes of up to 10^9 atoms, have been conducted at RISIKO using PI-LIST. First preliminary results revealed several hyperfine structure components of two examined atomic transitions. This ongoing experimental effort will possibly allow to extract nuclear moments. In addition, the first ionization potential in fermium could in future be determined to a high precision of sub meV via Rydberg series.

The available experimental information on nuclear charge radii and moments in neighboring isotopic chains to fermium is currently limited. Nonetheless, extending the prior studies in nobelium with two protons more [28] and in californium with two protons less [29] could shed light on the localization of the shell gap and its impact on nuclear moments. In addition, unknown nuclear spins could be unambiguously determined and the trend in isotones investigated. In a recent experiment, the isotope ^{255}No was investigated with RADRIS by applying an indirect production scheme using the $<30\,\%$ electron capture branch [214, 215] of directly produced ^{255}Lr. With the measurement of the isotope shift, information on the mean-square charge radius evolution across the $N = 152$ shell gap following ^{254}No became available. This data is under final analysis and will soon be published in connection with the fermium data [171]. In the proof-of-principle study on ^{251}No presented here, the advanced capabilities of the

RADRIS method were showcased allowing to access this short-lived isotope. In future experiments, higher-resolution measurements with reduced laser power will eventually enable the identification of the isotope shift for both, the ground state and the isomeric state, hence extending the chain of investigated isotopes beyond $^{252-254}$No [28]. With the ongoing development of the JetRIS apparatus, a study of the hyperfine structure of both could come in reach. Furthermore, new high-resolution measurements of ^{253}No are foreseen in the upcoming beamtime campaign at GSI to re-evaluate the nuclear moments with a better precision compared to the previous assessment.

The available data from offline measurements on reactor-breeding samples of $^{249-253}$Cf [29] can be extended in upcoming experiments at SHIP addressing the neutron-deficient isotopes $^{241-244}$Cf. These isotopes can be produced on-line via the reaction ^{196,198}Pt(^{48}Ca,2-3n)$^{241-244}$Cf, which feature cross sections in the order 40 to 400 nb [216, 217]. Even more neuron-deficient isotopes can additionally be accessed via the reaction ^{206,207}Pb(^{36}Sn,2-3n)^{239,240}Cf and with cross sections as high as 100 nb [218]. The former isotope would be particularly interesting to determine the yet unknown nuclear spin. The indirect production scheme outlined in this work for ^{250}Fm could potentially be used to access also the ^{246}Cf granddaughter for further studies with RADRIS. The recent and anticipated future work on measuring isotope shifts in californium is expected to trigger additional atomic theory efforts towards predictions of the atomic field shift parameter F_{FS}. Although no information on this property is available to date, it would be of highest interest to get insight into changes in mean-square charge radii from the experimental data.

Finally, ongoing experimental efforts on the search for atomic levels in the heaviest actinide element lawrencium are planned to be continued in upcoming beamtime campaigns at GSI. The initial experimental identification of an atomic structure level would open the possibility for nuclear structure investigations applying laser spectroscopy. In addition to further exploring the nuclear charge size evolution across the discussed deformed shell gap, these studies could involve the assessment of nuclear moments, including the electric quadrupole moment in the isomeric state of ^{255}Lr.

Bibliography

[1] C.F. von Weizsäcker. "Zur Theorie der Kernmassen". In: *Zeitschrift für Physik* 96.7-8 (1935), pp. 431–458.

[2] S. Hofmann and G. Münzenberg. "The discovery of the heaviest elements". In: *Review of Modern Physics* 72.3 (2000), pp. 733–767. DOI: 10.1103/RevModPhys.72.733.

[3] M. Goeppert Mayer. "On closed shells in nuclei. II". In: *Physical Review* 75.12 (1949), pp. 1969–1970. DOI: 10.1103/PhysRev.75.1969.

[4] M. Bender, P.-H. Heenen, and P.-G. Reinhard. "Self-consistent mean-field models for nuclear structure". In: *Reviews of Modern Physics* 75.1 (2003), pp. 121–180. DOI: 10.1103/RevModPhys.75.121.

[5] S.A. Giuliani et al. "Colloquium: Superheavy elements: Oganesson and beyond". In: *Reviews of Modern Physics* 91.1 (2019), p. 011001. DOI: 10.1103/RevModPhys.91.011001.

[6] S.G. Nilsson. "Binding states of individual nucleons in strongly deformed nuclei". In: *Kgl. Danske Videnskab. Selskab., Mat.-fys Medd.* 29.16 (1955), pp. 1–69.

[7] R. Broda et al. "$N = 40$ neutron subshell closure in the ^{68}Ni nucleus". In: *Physical Review Letters* 74.6 (1995), pp. 868–871. DOI: 10.1103/PhysRevLett.74.868.

[8] O. Sorlin et al. "$^{68}_{28}Ni_{40}$: Magicity versus superfluidity". In: *Physical Review Letters* 88.9 (2002), p. 092501. DOI: 10.1103/PhysRevLett.88.092501.

[9] M.L. Bissell et al. "Cu charge radii reveal a weak sub-shell effect at $N = 40$". In: *Physical Review C* 93.6 (2016), p. 064318. DOI: 10.1103/PhysRevC.93.064318.

[10] D.J. Hartley et al. "Masses and β-decay spectroscopy of neutron-rich odd-odd ^{160,162}Eu nuclei: Evidence for a subshell gap with large deformation at $N = 98$". In: *Physical Review Letters* 120.18 (2018), p. 182502. DOI: 10.1103/PhysRevLett.120.182502.

[11] D.J. Hartley et al. "Possible quenching of static neutron pairing near the $N = 98$ deformed shell gap: Rotational structures in ^{160,161}Gd". In: *Physical Review C* 103.3 (2021), p. 034322. DOI: 10.1103/PhysRevC.103.034322.

[12] D.J. Hartley et al. "$\nu i_{13/2}$ structures in ^{155}Sm and ^{159}Gd: Supporting evidence of a $Z = 60$ deformed subshell gap". In: *Physical Review C* 105.1 (2022), p. 014301. DOI: 10.1103/PhysRevC.105.014301.

[13] E. Minaya Ramirez et al. "Direct mapping of nuclear shell effects in the heaviest elements". In: *Science* 337.6099 (2012), pp. 1207–1210. DOI: 10.1126/science.1225636.

[14] S. Ćwiok, P.-H. Heenen, and W. Nazarewicz. "Shape coexistence and triaxiality in the superheavy nuclei". In: *Nature* 433.7027 (2005), pp. 705–709. DOI: 10.1038/nature03336.

[15] Ch. Theisen et al. "In-beam spectroscopy of heavy elements". In: *Nuclear Physics A* 944 (2015), pp. 333–375. DOI: 10.1016/j.nuclphysa.2015.07.014.

[16] A. Ghiorso et al. "Evidence for subshell at $N = 152$". In: *Physical Review* 95.1 (1954), pp. 293–295. DOI: 10.1103/physrev.95.293.

[17] P. Campbell, I.D. Moore, and M.R. Pearson. "Laser spectroscopy for nuclear structure physics". In: *Progress in Particle and Nuclear Physics* 86 (2016), pp. 127–180. DOI: 10.1016/j.ppnp.2015.09.003.

[18] W. Nörtershäuser and I.D. Moore. "Nuclear charge radii". In: *Handbook of Nuclear Physics*. Springer Nature Singapore, 2020, pp. 1–70. DOI: 10.1007/978-981-15-8818-1_41-1.

[19] X.F. Yang et al. "Laser spectroscopy for the study of exotic nuclei". In: *Progress in Particle and Nuclear Physics* 129 (2022), p. 104005. DOI: 10.1016/j.ppnp.2022.104005.

[20] M. Block, M. Laatiaoui, and S. Raeder. "Recent progress in laser spectroscopy of the actinides". In: *Progress in Particle and Nuclear Physics* 116 (2021), p. 103834. DOI: 10.1016/j.ppnp.2020.103834.

[21] K. Kreim et al. "Nuclear charge radii of potassium isotopes beyond $N = 28$". In: *Physics Letters B* 731 (2014), pp. 97–102. ISSN: 0370-2693. DOI: 10.1016/j.physletb.2014.02.012.

[22] C. Gorges et al. "Laser Spectroscopy of Neutron-Rich Tin Isotopes: A Discontinuity in Charge Radii across the $N = 82$ Shell Closure". In: *Physics Review Letters* 122.19 (2019), p. 192502. DOI: 10.1103/PhysRevLett.122.192502.

[23] M. Reponen et al. "Evidence of a sudden increase in the nuclear size of proton-rich silver-96". In: *Nature Communications* 12.1 (2021), p. 4596. DOI: 10.1038/s41467-021-24888-x.

[24] T. Day Goodacre et al. "Charge radii, moments, and masses of mercury isotopes across the $N = 126$ shell closure". In: *Physical Review C* 104.5 (2021), p. 054322. DOI: 10.1103/PhysRevC.104.054322.

[25] G. Neyens. "Nuclear magnetic and quadrupole moments for nuclear structure research on exotic nuclei". In: *Reports on Progress in Physics* 66.4 (2003), p. 633. DOI: 10.1088/0034-4885/66/4/205.

[26] R.P. de Groote and G. Neyens. "Spins and electromagnetic moments of nuclei". In: *Handbook of Nuclear Physics*. Springer Nature Singapore, 2020, pp. 1–36. DOI: 10.1007/978-981-15-8818-1_42-1.

[27] M. Laatiaoui et al. "Atom-at-a-time laser resonance ionization spectroscopy of nobelium". In: *Nature* 538.7626 (2016), pp. 495–498. DOI: https://doi.org/10.1038/nature19345.

[28] S. Raeder et al. "Probing Sizes and Shapes of Nobelium Isotopes by Laser Spectroscopy". In: *Physics Review Letters* 120.23 (2018), p. 232503. DOI: 10.1103/PhysRevLett.120.232503.

[29] F. Weber et al. “Nuclear moments and isotope shifts of the actinide isotopes $^{249–253}$Cf probed by laser spectroscopy”. In: *Physical Review C* 107.3 (2023), p. 034313. DOI: 10.1103/PhysRevC.107.034313.

[30] G. Gamow. “Mass defect curve and nuclear constitution”. In: *Proceedings of the Royal Society of London. Series A, Containing Papers of a Mathematical and Physical Character* 126.803 (1930), pp. 632–644. DOI: 10.1098/rspa.1930.0032.

[31] W.D. Myers and K.-H. Schmidt. “An update on droplet-model charge distributions”. In: *Nuclear Physics A* 410.1 (1983), pp. 61–73. DOI: 10.1016/0375-9474(83)90401-3.

[32] O. Haxel, J. Hans D. Jensen, and H.E. Suess. “On the "magic numbers" in nuclear structure”. In: *Physics Review* 75.11 (1949), pp. 1766–1766. DOI: 10.1103/PhysRev.75.1766.2.

[33] K.S. Krane. *Introductory nuclear physics*. John Wiley & Sons, 1991.

[34] R.D. Woods and D.S. Saxon. “Diffuse surface optical model for nucleon-nuclei scattering”. In: *Physics Review* 95 (2 1954), pp. 577–578. DOI: 10.1103/PhysRev.95.577.

[35] Th. Mayer-Kuckuk. *Kernphysik: Eine Einführung*. Springer-Verlag, 2013.

[36] B. Povh et al. *Particles and nuclei. An introduction into the physical concepts*. Springer Berlin, Heidelberg, 2014.

[37] M. Goeppert Mayer. “The shell model”. In: *Science* 145.3636 (1964), pp. 999–1006. DOI: 10.1126/science.145.3636.999.

[38] R.F. Casten. *Nuclear structure from a simple perspective*. Oxford University Press, 2001. DOI: 10.1093/acprof:oso/9780198507246.001.0001.

[39] R.B. Firestone. *Table of Isotopes*. New York: Wiley, 1999. ISBN: 978-0-471-35633-2.

[40] M. Asai et al. “Neutron one-quasiparticle states in ^{251}Fm$_{151}$ populated via the α decay of ^{255}No”. In: *Physical Review C* 83.1 (2011), p. 014315. DOI: 10.1103/PhysRevC.83.014315.

[41] P. Möller et al. “Nuclear ground-state masses and deformations: FRDM (2012)”. In: *Atomic Data and Nuclear Data Tables* 109 (2016), pp. 1–204. DOI: 10.1016/j.adt.2015.10.002.

[42] O. Dumitrescu and C. Cioaca. “Fine structure in the cluster decays of the translead nuclei”. In: *Physical Review C* 51.6 (1995), pp. 3264–3282. DOI: 10.1103/PhysRevC.51.3264.

[43] F. Asaro, S. Bjørnholm, and I. Perlman. “Decay scheme of Fm^{255}”. In: *Physics Review* 133.2B (1964), B291–B300. DOI: 10.1103/PhysRev.133.B291.

[44] F.P. Heßberger et al. “Alpha-gamma decay studies of 251, 253 No and their daughter products 247, 249 Fm”. In: *The European Physical Journal A-Hadrons and Nuclei* 22 (2004), pp. 417–427. DOI: 10.1140/epja/i2003-10238-4.

[45] S.K. Bogner, R.J. Furnstahl, and A. Schwenk. “From low-momentum interactions to nuclear structure”. In: *Progress in Particle and Nuclear Physics* 65.1 (2010), pp. 94–147. DOI: 10.1016/j.ppnp.2010.03.001.

[46] H. Hergert. "A guided tour of ab initio nuclear many-body theory". In: *Frontiers in Physics* 8 (2020), p. 379. DOI: 10.3389/fphy.2020.00379.

[47] J. Dobaczewski. "Current developments in nuclear density functional methods". In: *Journal of Physics: Conference Series*. Vol. 312. 9. IOP Publishing. 2011, p. 092002. DOI: 10.1088/1742-6596/312/9/092002.

[48] R. Machleidt and F. Sammarruca. "Can chiral EFT give us satisfaction?" In: *The European Physical Journal A* 56 (2020), pp. 1–24. DOI: 10.1140/epja/s10050-020-00101-3.

[49] P. Navrátil and S. Quaglioni. "Ab initio nuclear reaction theory with applications to astrophysics". In: *Handbook of Nuclear Physics*. Springer Nature Singapore, 2020, pp. 1–46. DOI: 10.1007/978-981-15-8818-1_7-1.

[50] B. Hu et al. "Ab initio predictions link the neutron skin of 208Pb to nuclear forces". In: *Nature Physics* 18.10 (2022), pp. 1196–1200. DOI: 10.1038/s41567-022-01715-8.

[51] N. Schunck, ed. *Energy Density Functional Methods for Atomic Nuclei*. 2053-2563. IOP Publishing, 2019. DOI: 10.1088/2053-2563/aae0ed.

[52] W.D. Myers and W.J. Swiatecki. "Nuclear masses and deformations". In: *Nuclear Physics* 81.1 (1966), pp. 1–60. DOI: 10.1016/0029-5582(66)90639-0.

[53] V.M. Strutinsky. "Shell effects in nuclear masses and deformation energies". In: *Nuclear Physics A* 95.2 (1967), pp. 420–442. DOI: 10.1016/0375-9474(67)90510-6.

[54] V.M. Strutinsky. ""Shells" in deformed nuclei". In: *Nuclear Physics A* 122.1 (1968), pp. 1–33. DOI: 10.1016/0375-9474(68)90699-4.

[55] W.D. Myers. "Droplet model nuclear density distributions and single-particle potential wells". In: *Nuclear Physics A* 145.2 (1970), pp. 387–400. DOI: 10.1016/0375-9474(70)90432-X.

[56] W.D Myers and W.J Swiatecki. "The nuclear droplet model for arbitrary shapes". In: *Annals of Physics* 84.1 (1974), pp. 186–210. DOI: https://doi.org/10.1016/0003-4916(74)90299-1.

[57] W.D. Myers. *Droplet model of atomic nuclei*. Plenum Publishing Corporation, 1977.

[58] D. Berdichevsky and F. Tondeur. "Nuclear core densities, isotope shifts, and the parametrization of the droplet model". In: *Zeitschrift für Physik A Atoms and Nuclei* 322 (1985), pp. 141–147. DOI: 10.1007/BF01412027.

[59] R. Bengtsson et al. "Nuclear shapes and shape transitions". In: *Physica Scripta* 29.5 (1984), p. 402. DOI: 10.1088/0031-8949/29/5/002.

[60] P. Möller et al. "Nuclear mass formula with a finite-range droplet model and a folded-Yukawa single-particle potential". In: vol. 39. 2. 1988, pp. 225–233. DOI: 10.1016/0092-640X(88)90023-X.

[61] P. Möller et al. "Nuclear mass formula with a finite-range droplet model and a folded-Yukawa single-particle potential". In: *Atomic Data and Nuclear Data Tables* 39.2 (1988), pp. 225–233. DOI: https://doi.org/10.1016/0092-640X(88)90023-X.

[62] G.F. Bertsch, D.J. Dean, and W. Nazarewicz. "Computing atomic nuclei: The universal nuclear energy density functional". In: *SciDAC Review* 6 (2007).
[63] W. Ryssens et al. "Solution of the Skyrme–HF+ BCS equation on a 3D mesh, II: A new version of the Ev8 code". In: *Computer Physics Communications* 187 (2015), pp. 175–194. DOI: 0.1016/j.cpc.2014.10.001.
[64] T.H.R. Skyrme. "The effective nuclear potential". In: *Nuclear Physics* 9.4 (1958), pp. 615–634. DOI: 10.1016/0029-5582(58)90345-6.
[65] P. Klüpfel et al. "Variations on a theme by Skyrme: A systematic study of adjustments of model parameters". In: *Physics Review C* 79 (3 2009), p. 034310. DOI: 10.1103/PhysRevC.79.034310.
[66] W. Ryssens et al. "Skyrme–Hartree–Fock–Bogoliubov mass models on a 3D mesh: II. Time-reversal symmetry breaking". In: *The European Physical Journal A* 58.12 (2022), p. 246. DOI: 10.1140/epja/s10050-022-00894-5.
[67] J. Sadoudi et al. "Skyrme functional from a three-body pseudopotential of second order in gradients: Formalism for central terms". In: *Physical Review C* 88.6 (2013), p. 064326. DOI: 10.1103/PhysRevC.88.064326.
[68] N. Pillet and S. Hilaire. "Towards an extended Gogny force: History, state of the art and perspectives". In: *The European Physical Journal A* 53.10 (2017), p. 193. DOI: 10.1140/epja/i2017-12369-3.
[69] P. Ring and P. Schuck. *The nuclear many-body problem*. Springer Science & Business Media, 2004.
[70] J.F. Berger, M. Girod, and D. Gogny. "Microscopic analysis of collective dynamics in low energy fission". In: *Nuclear Physics A* 428 (1984), pp. 23–36. DOI: 10.1016/0375-9474(84)90240-9.
[71] S. Goriely et al. "First Gogny-Hartree-Fock-Bogoliubov nuclear mass model". In: *Physics Review Letters* 102.24 (2009), p. 242501. DOI: 10.1103/PhysRevLett.102.242501.
[72] S.A. Fayans. "Towards a universal nuclear density functional". In: *Journal of Experimental and Theoretical Physics Letters* 68 (1998), pp. 169–174. DOI: 10.1134/1.567841.
[73] S.A. Fayans et al. "Nuclear isotope shifts within the local energy-density functional approach". In: *Nuclear Physics A* 676.1-4 (2000), pp. 49–119. DOI: 10.1016/S0375-9474(00)00192-5.
[74] P.-G. Reinhard and W. Nazarewicz. "Toward a global description of nuclear charge radii: Exploring the Fayans energy density functional". In: *Physics Review C* 95.6 (2017), p. 064328. DOI: 10.1103/PhysRevC.95.064328.
[75] A.J. Miller et al. "Proton superfluidity and charge radii in proton-rich calcium isotopes". In: *Nature Physics* 15.5 (2019), pp. 432–436. DOI: 10.1038/s41567-019-0416-9.
[76] T. Nikšić, D. Vretenar, and P. Ring. "Relativistic nuclear energy density functionals: Mean-field and beyond". In: *Progress in Particle and Nuclear Physics* 66.3 (2011), pp. 519–548. DOI: 10.1016/j.ppnp.2011.01.055.

[77] F. Wauters and A. Knecht on behalf of the muX collaboration. "The muX project". In: *SciPost Physics Proceedings* 5 (2021), p. 022. DOI: 10.21468/SciPostPhysProc.5.022.

[78] M. Block, S. Raeder, and R.-D. Herzberg. "Heaviest elements: Decay and laser spectroscopy". In: *Handbook of Nuclear Physics*. Springer Nature Singapore, 2020, pp. 1–43. DOI: 10.1007/978-981-15-8818-1_45-1.

[79] B. Cheal et al. "The shape transition in the neutron-rich yttrium isotopes and isomers". In: *Physics Letters B* 645.2 (2007), pp. 133–137. DOI: 10.1016/j.physletb.2006.12.053.

[80] B.A. Marsh et al. "Characterization of the shape-staggering effect in mercury nuclei". In: *Nature Physics* 14.12 (2018), pp. 1163–1167. DOI: 10.1038/s41567-018-0292-8.

[81] W. Demtroeder. *Experimentalphysik 3: Atome, Molekuele, Festkoerper*. Springer, 2010. ISBN: 978-3-642-03910-2.

[82] W. Demtroeder. *Laserspektroskopie 1 Grundlagen*. Springer, 2011. ISBN: 978-3-642-21305-2.

[83] F. Schneider et al. "Resonance ionization of holmium for ion implantation in microcalorimeters". In: *Nuclear Instruments and Methods in Physics Research Section B: Beam Interactions with Materials and Atoms* 376 (2016), pp. 388–392. DOI: 10.1016/j.nimb.2015.12.012.

[84] N. Allard and J. Kielkopf. "The effect of neutral nonresonant collisions on atomic spectral lines". In: *Reviews of Modern Physics* 54.4 (1982), pp. 1103–1182. DOI: 10.1103/RevModPhys.54.1103.

[85] Yu. Kudryavtsev et al. "The in-gas-jet laser ion source: Resonance ionization spectroscopy of radioactive atoms in supersonic gas jets". In: *Nuclear Instruments and Methods in Physics Research Section B: Beam Interactions with Materials and Atoms* 297 (2013), pp. 7–22. DOI: 10.1016/j.nimb.2012.12.008.

[86] C. Granados et al. "In-gas laser ionization and spectroscopy of actinium isotopes near the $N = 126$ closed shell". In: *Physical Review C* 96.5 (2017), p. 054331. DOI: 10.1103/PhysRevC.96.054331.

[87] A. Ajayakumar et al. "In-gas-jet laser spectroscopy with S3-LEB". In: *Nuclear Instruments and Methods in Physics Research Section B: Beam Interactions with Materials and Atoms* 539 (2023), pp. 102–107. DOI: https://doi.org/10.1016/j.nimb.2023.03.020.

[88] K.D.A. Wendt et al. "Laser Based Techniques for Ultra Trace Isotope Production, Spectroscopy and Detection". In: *Laser 2004*. Ed. by Z. Błaszczak, B. Markov, and K. Marinova. Berlin, Heidelberg: Springer Berlin Heidelberg, 2006, pp. 147–157. DOI: 10.1007/3-540-30926-8_18.

[89] R.V. Ambartzumian and V.S. Letokhov. "Selective two-step (STS) photoionization of atoms and photodissociation of molecules by laser radiation". In: *Applied Optics* 11.2 (1972), pp. 354–358. DOI: 10.1364/AO.11.000354.

[90] V. Fedosseev et al. "Ion beam production and study of radioactive isotopes with the laser ion source at ISOLDE". In: *Journal of Physics G: Nuclear and Particle Physics* 44.8 (2017), p. 084006. DOI: 10.1088/1361-6471/aa78e0.

[91] M. Franzmann et al. "A new resonant laser-SNMS system for environmental ultra-trace analysis: installation and optimization". In: *International Journal of Mass Spectrometry* 423 (2017), pp. 27–32. DOI: 10.1016/j.ijms.2017.10.003.

[92] K. Blaum, J. Dilling, and W. Nörtershäuser. "Precision atomic physics techniques for nuclear physics with radioactive beams". In: *Physica Scripta* 2013.T152 (2013), p. 014017. DOI: 10.1088/0031-8949/2013/T152/014017.

[93] E.C. Seltzer. "K X-Ray Isotope Shifts". In: *Physics Review* 188 (4 1969), pp. 1916–1919. DOI: 10.1103/PhysRev.188.1916.

[94] W. Ryssens. *Private communication.*

[95] A. Papoulia, B. G. Carlsson, and J. Ekman. "Effect of realistic nuclear charge distributions on isotope shifts and progress towards the extraction of higher-order nuclear radial moments". In: *Physical Review A* 94.4 (2016), p. 042502. DOI: 10.1103/PhysRevA.94.042502.

[96] B. Cheal, T.E. Cocolios, and S. Fritzsche. "Laser spectroscopy of radioactive isotopes: Role and limitations of accurate isotope-shift calculations". In: *Physical Review A* 86 (4 2012), p. 042501. DOI: 10.1103/PhysRevA.86.042501.

[97] W.H. King. *Isotope shifts in atomic spectra.* Springer Science & Business Media, 2013. ISBN: 978-1-4899-1788-1.

[98] J.C. Berengut et al. "Probing new long-range interactions by isotope shift Ssectroscopy". In: *Physics Review Letters* 120.9 (Feb. 2018), p. 091801. DOI: 10.1103/PhysRevLett.120.091801.

[99] S.O. Allehabi et al. "Theoretical study of electronic structure of erbium and fermium". In: *Journal of Quantitative Spectroscopy and Radiative Transfer* 253 (2020), p. 107137. DOI: 10.1016/j.jqsrt.2020.107137.

[100] S. Fritzsche. "Level structure and properties of open f-shell elements". In: *Atoms* 10.1 (2022), p. 7. DOI: 10.3390/atoms10010007.

[101] Ch. Froese Fischer et al. "Advanced multiconfiguration methods for complex atoms: I. Energies and wave functions". In: *Journal of Physics B: Atomic, Molecular and Optical Physics* 49.18 (2016), p. 182004. DOI: 10.1088/0953-4075/49/18/182004.

[102] V.A. Dzuba, M.S. Safronova, and U.I. Safronova. "Atomic properties of superheavy elements No, Lr, and Rf". In: *Physical Review A* 90 (1 2014), p. 012504. DOI: 10.1103/PhysRevA.90.012504.

[103] M.S. Safronova et al. "Development of a configuration-interaction plus all-order method for atomic calculations". In: *Physical Review A* 80.1 (2009), p. 012516. DOI: 10.1103/PhysRevA.80.012516.

[104] V.A. Dzuba et al. "Combining configuration interaction with perturbation theory for atoms with a large number of valence electrons". In: *Physical Review A* 95.1 (2017), p. 012503. DOI: 10.1103/PhysRevA.95.012503.

[105] P. Indelicato et al. "QED and relativistic corrections in superheavy elements". In: *The European Physical Journal D* 45 (2007), pp. 155–170. DOI: 10.1140/epjd/e2007-00229-y.

[106] A. Ghiorso et al. "New Elements Einsteinium and Fermium, Atomic Numbers 99 and 100". In: *Physical Review* 99.3 (1955), pp. 1048–1049. DOI: 10.1103/PhysRev.99.1048.

[107] H. Backe et al. "Laser spectroscopic investigation of the element fermium (Z= 100)". In: *Laser 2004: Proceedings of the 6th International Workshop on Application of Lasers in Atomic Nuclei Research (LASER 2004) held in Poznań, Poland, 24–27 May 2004*. Springer. 2006, pp. 3–14. DOI: 10.1007/3-540-30926-8_1.

[108] M. Wang et al. "The AME 2020 atomic mass evaluation (II). Tables, graphs and references". In: *Chinese Physics C* 45.3 (2021), p. 030003. DOI: 10.1088/1674-1137/abddaf.

[109] A. Osa et al. *JAEA-Tokai tandem annual report 2013. April 1, 2013-March 31, 2014*. Tech. rep. Japan Atomic Energy Agency, 2016. DOI: 10.11484/jaea-review-2016-025.

[110] R.-D. Herzberg and P.T. Greenlees. "In-beam and decay spectroscopy of transfermium nuclei". In: *Progress in Particle and Nuclear Physics* 61.2 (2008), pp. 674–720. DOI: 10.1016/j.ppnp.2008.05.003.

[111] J. Piot et al. "Investigation of 246Fm : in-beam spectroscopy at the limits". In: *AIP Conference Proceedings* 1377.1 (2011), pp. 301–305. DOI: 10.1063/1.3628397.

[112] S. Ketelhut. "Rotational structures and high-K isomerism in ^{248,250}Fm". Dissertation. Research report/Department of Physics, University of Jyväskylä, 2010. URL: https://jyx.jyu.fi/bitstream/handle/123456789/25753/Steffen-Ketelhut-2010.pdf.

[113] J.E. Bastin et al. "In-beam gamma ray and conversion electron study of ^{250}Fm". In: *Physical Review C* 73.2 (), p. 024308. DOI: 10.1103/PhysRevC.73.024308.

[114] A. Ghiorso et al. "Isomeric States in ^{250}Fm and ^{254}No". In: *Physical Review C* 7.5 (1973), pp. 2032–2036. DOI: 10.1103/PhysRevC.7.2032.

[115] F.P. Heßberger et al. "Alpha-gamma decay studies of ^{255}Rf, ^{251}No and ^{247}Fm". In: *The European Physical Journal A-Hadrons and Nuclei* 30 (2006), pp. 561–569. DOI: 10.1140/epja/i2006-10137-2.

[116] R.-D. Herzberg and D.M. Cox. "Spectroscopy of actinide and transactinide nuclei". In: *Radiochimica Acta* 99.7-8 (2011), pp. 441–457.

[117] S. Antalic et al. "Isomeric states in 253 No and 253 Fm". In: *The European Physical Journal A* 47 (2011), pp. 1–12. DOI: 10.1140/epja/i2011-11062-y.

[118] L.S. Goodman et al. "g_J value for the atomic ground state of fermium". In: *Physical Review A* 4 (2 1971), pp. 473–475. DOI: 10.1103/PhysRevA.4.473.

[119] H. Backe et al. "A compact apparatus for mass selective resonance ionization spectroscopy in a buffer gas cell". In: *Nuclear Instruments and Methods in Physics Research Section B: Beam Interactions with Materials and Atoms* 126.1-4 (1997), pp. 406–410. DOI: 10.1016/S0168-583X(96)01035-X.

[120] M. Sewtz et al. "First observation of atomic levels for the element fermium ($Z = 100$)". In: *Physical Review Letters* 90.16 (2003), p. 163002. DOI: 10.1103/PhysRevLett.90.163002.

[121] J. Sugar. "Revised ionization energies of the neutral actinides". In: *The Journal of Chemical Physics* 60.10 (1974), pp. 4103–4103. DOI: 10.1063/1.1680874.

[122] Á. Koszorús et al. "Charge radii of exotic potassium isotopes challenge nuclear theory and the magic character of $N = 32$". In: *Nature Physics* 17.4 (2021), pp. 439–443. DOI: 10.1038/s41567-020-01136-5.

[123] R.P. de Groote et al. "Measurement and microscopic description of odd–even staggering of charge radii of exotic copper isotopes". In: *Nature Physics* 16.6 (2020), pp. 620–624. DOI: 10.1038/s41567-020-0868-y.

[124] M.J.G. Borge and K. Blaum. "Focus on exotic beams at ISOLDE: A laboratory portrait". In: *Journal of Physics G: Nuclear and Particle Physics* 45.1 (Nov. 2017), p. 010301. DOI: 10.1088/1361-6471/aa990f.

[125] J. Dilling, R. Krücken, and L. Merminga. *ISAC and ARIEL: the TRIUMF radioactive beam facilities and the scientific program*. Springer, 2014. DOI: 10.1007/978-94-007-7963-1.

[126] G. Prete et al. "The SPES project: a second generation ISOL facility". In: *Physics Procedia* 26 (2012), pp. 274–283. DOI: 10.1016/j.phpro.2012.03.035.

[127] B.H. Kang et al. "ISOL facility for rare isotope beams at RAON". In: *Journal of the Korean Physical Society* 63 (2013), pp. 1473–1476. DOI: 10.3938/jkps.63.1473.

[128] J.B. Roberto et al. "Actinide targets for the synthesis of super-heavy elements". In: *Nuclear Physics A* 944 (Dec. 2015), pp. 99–116. DOI: 10.1016/j.nuclphysa.2015.06.009.

[129] S.M. Robinson et al. "Production of Cf-252 and other transplutonium isotopes at Oak Ridge National Laboratory". In: *Radiochimica Acta* 108.9 (2020), pp. 737–746. DOI: 10.1515/ract-2020-0008.

[130] B.B. Back et al. "Recent developments in heavy-ion fusion reactions". In: *Reviews of Modern Physics* 86.1 (2014), pp. 317–360. DOI: 10.1103/RevModPhys.86.317.

[131] L. Corradi et al. "Multinucleon transfer reactions: Present status and perspectives". In: *Nuclear Instruments and Methods in Physics Research Section B: Beam Interactions with Materials and Atoms* 317 (2013), pp. 743–751. DOI: 10.1016/j.nimb.2013.04.093.

[132] W. Reisdorf. "Analysis of fissionability data at high excitation energies: I. The level density problem". In: *Zeitschrift für Physik A Atoms and Nuclei* 300.2-3 (1981), pp. 227–238. DOI: 10.1007/BF01412298.

[133] F. Lautenschläger et al. "Developments for resonance ionization laser spectroscopy of the heaviest elements at SHIP". In: *Nuclear Instruments and Methods in Physics Research Section B: Beam Interactions with Materials and Atoms* 383 (2016), pp. 115–122. DOI: 10.1016/j.nimb.2016.06.001.

[134] G. Münzenberg et al. "The new isotopes ^{247}Md, ^{243}Fm, ^{239}Cf, and investigation of the evaporation residues from fusion of ^{206}Pb, ^{208}Pb, and ^{209}Bi with ^{40}Ar". In: *Zeitschrift für Physik A Atoms and Nuclei* 302 (1981), pp. 7–14. DOI: 10.1007/BF01425097.

[135] Yu.Ts. Oganessian et al. "Measurements of cross sections for the fusion-evaporation reactions ^{204,206,207,208}Pb+^{48}Ca and ^{207}Pb+^{34}S : Decay properties of the even-even nuclides ^{238}Cf and ^{250}No". In: *Physical Review C* 64.5 (2001), p. 054606. DOI: 10.1103/PhysRevC.64.054606.

[136] M. Dworschak et al. "Penning trap mass measurements on nobelium isotopes". In: *Physical Review C* 81.6 (2010), p. 064312. DOI: 10.1103/PhysRevC.81.064312.

[137] H.W. Gäggeler et al. "Cold fusion reactions with ^{48}Ca". In: *Nuclear Physics A* 502 (1989), pp. 561–570. DOI: 10.1016/0375-9474(89)90689-1.

[138] F.P. Heßberger. *Private communication.*

[139] P.T. Greenlees et al. "High-K structure in ^{250}Fm and the deformed shell gaps at $N = 152$ and $Z = 100$". In: *Physical Review C* 78.2 (2008), p. 021303. DOI: 10.1103/PhysRevC.78.021303.

[140] J. Khuyagbaatar et al. "Spontaneous fission of neutron-deficient fermium isotopes and the new nucleus ^{241}Fm". In: *The European Physical Journal A* 37 (2008), pp. 177–183. DOI: 10.1140/epja/i2008-10608-4.

[141] J. Khuyagbaatar et al. "α decay of ^{243}Fm$_{143}$ and ^{245}Fm$_{145}$, and of their daughter nuclei". In: *Physical Review C* 102.4 (2020), p. 044312. DOI: 10.1103/PhysRevC.102.044312.

[142] G.N. Flerov et al. "Synthesis of isotopes of fermium with mass numbers 247 and 246". In: *Soviet Atomic Energy* 22.5 (1967), pp. 434–437. DOI: 10.1007/BF01175203.

[143] A. Türler et al. "Actinide production from the interactions of ^{40}Ca and ^{44}Ca with ^{248}Cm and a comparison with the ^{48}Ca+^{248}Cm system". In: *Physical Review C* 46.4 (1992), pp. 1364–1382. DOI: 10.1103/PhysRevC.46.1364.

[144] G. Münzenberg et al. "The velocity filter SHIP, a separator of unslowed heavy ion fusion products". In: *Nuclear Instruments and Methods* 161.1 (1979), pp. 65–82. DOI: 10.1016/0029-554X(79)90362-8.

[145] H. Backe et al. "Prospects for laser spectroscopy, ion chemistry and mobility measurements of superheavy elements in buffer-gas traps". In: *Nuclear Physics A* 944 (2015), pp. 492–517. DOI: 10.1016/j.nuclphysa.2015.07.002.

[146] S. Raeder. *Private communication.*

[147] J. Äystö. "Development and applications of the IGISOL technique". In: *Nuclear Physics A* 693.1-2 (2001), pp. 477–494. DOI: 10.1016/S0375-9474(01)00923-X.

[148] J. Ärje and K. Valli. "Helium-jet ion guide for an on-line isotope separator". In: *Nuclear Instruments and Methods* 179.3 (1981), pp. 533–539. DOI: 10.1016/0029-554X(81)90179-8.

[149] M. Wada et al. "Slow RI-beams from projectile fragment separators". In: *Nuclear Instruments and Methods in Physics Research Section B: Beam Interactions with Materials and Atoms* 204 (2003), pp. 570–581. DOI: 10.1016/S0168-583X(02)02151-1.

[150] W.R. Plaß et al. "The FRS Ion Catcher–A facility for high-precision experiments with stopped projectile and fission fragments". In: *Nuclear Instruments and*

Methods in Physics Research Section B: Beam Interactions with Materials and Atoms 317 (2013), pp. 457–462. DOI: 10.1016/j.nimb.2013.07.063.

[151] G. Savard, A.F. Levand, and B.J. Zabransky. "The CARIBU gas catcher". In: *Nuclear Instruments and Methods in Physics Research Section B: Beam Interactions with Materials and Atoms* 376 (2016), pp. 246–250. DOI: 10.1016/j.nimb.2016.02.050.

[152] C. Droese et al. "The cryogenic gas stopping cell of SHIPTRAP". In: *Nuclear Instruments and Methods in Physics Research Section B: Beam Interactions with Materials and Atoms* 338 (2014), pp. 126–138. DOI: 10.1016/j.nimb.2014.08.004.

[153] H. Backe et al. "Towards optical spectroscopy of the element nobelium ($Z = 102$) in a buffer gas cell: First on-line experiments on ^{155}Yb at the velocity filter SHIP with a novel ion collection and atom re-evaporation method of high efficiency". In: *The European Physical Journal D* 45 (2007), pp. 99–106. DOI: 10.1140/epjd/e2007-00198-1.

[154] H. Backe et al. "Isotope Shift Measurements for Superdeformed Fission Isomeric States". In: *Physical Review Letters* 80.5 (1998), pp. 920–923. DOI: 10.1103/PhysRevLett.80.920.

[155] P. Chhetri et al. "Precision measurement of the first ionization potential of nobelium". In: *Physical Review Letters* 120 (26 2018), p. 263003. DOI: 10.1103/PhysRevLett.120.263003.

[156] F. Lautenschläger. "Laserspektroskopie an Nobelium (Z=102) in einer Puffergaszelle". Dissertation. Technischen Universität Darmstadt, 2016.

[157] P. Chhetri. "Laser spectroscopy of nobelium isotopes". Dissertation. Technischen Universität Darmstadt, 2018. URL: https://tuprints.ulb.tu-darmstadt.de/8204/8/PremadityaChhetri_Thesis.pdf.

[158] M.J. Dresser. "The Saha-Langmuir equation and its application". In: *Journal of Applied Physics* 39.1 (1968), pp. 338–339. DOI: 10.1063/1.1655755.

[159] M. Laatiaoui et al. "Perspectives for laser spectroscopy of the element nobelium". In: *Hyperfine Interactions* 227 (2014), pp. 69–75. DOI: 10.1007/s10751-013-0971-x.

[160] H.B. Michaelson. "The work function of the elements and its periodicity". In: *Journal of Applied Physics* 48.11 (1977), pp. 4729–4733. DOI: 10.1063/1.323539.

[161] V. Pershina. "Relativistic effects on the properties of Lr: a periodic DFT study of the adsorption of Lr on surfaces of Ta in comparison with Lu and Tl". In: *Inorganic Chemistry* 59.8 (2020), pp. 5490–5496. DOI: 10.1021/acs.inorgchem.0c00120.

[162] T.K. Sato et al. "First ionization potentials of Fm, Md, No, and Lr: Verification of filling-up of 5f electrons and confirmation of the actinide series". In: *Journal of the American Chemical Society* 140.44 (2018), pp. 14609–14613. DOI: 10.1021/jacs.8b09068.

[163] T. Murböck et al. "Filament studies for laser spectroscopy on lawrencium". In: *Hyperfine Interactions* 241.35 (2020), pp. 1–9. DOI: 10.1007/s10751-019-1689-1.

[164] J. Warbinek et al. "Advancing radiation-detected resonance ionization towards heavier elements and more exotic nuclides". In: *Atoms* 10.2 (2022), p. 41. DOI: 10.3390/atoms10020041.

[165] S. Raeder et al. "Opportunities and limitations of in-gas-cell laser spectroscopy of the heaviest elements with RADRIS". In: *Nuclear Instruments and Methods in Physics Research Section B: Beam Interactions with Materials and Atoms* 541 (2023), pp. 370–374. DOI: 10.1016/j.nimb.2023.04.044.

[166] E. Rickert. "Laser spectroscopy of fermium isotopes and development of an actinide ion mobility spectrometer". Dissertation. Johannes Gutenberg-Universität Mainz, 2023.

[167] A. Chatillon et al. "Spectroscopy and single-particle structure of the odd-Z heavy elements ^{255}Lr, ^{251}Md and ^{247}Es". In: *The European Physical Journal A-Hadrons and Nuclei* 30 (2006), pp. 397–411. DOI: 10.1140/epja/i2006-10134-5.

[168] D.A. Dahl. "SIMION for the personal computer in reflection". In: *International Journal of Mass Spectrometry* 200.1-3 (2000), pp. 3–25. DOI: 10.1016/S1387-3806(00)00305-5.

[169] E. Rickert et al. *Publication on the level search and desorption measurements in lawrencium, to be submitted.*

[170] S. Nothhelfer. "Advances in laser spectroscopy of superheavy elements: Resonance ionization spectroscopy on 253,254,255 Es and a new gas-jet based high-resolution spectroscopy setup". Dissertation. Johannes Gutenberg-Universität Mainz, 2022. URL: https://openscience.ub.uni-mainz.de/handle/20.500.12030/6970.

[171] J. Warbinek et al. *Publication on the results of laser spectroscopy of fermium presented in this work in comparison to nuclear model calculations. To be submitted.*

[172] K. Zimmer. "Konzeption, Aufbau und Test der Ionenoptik des RISIKO-Massenseparators". Diploma thesis. Johannes Gutenberg-Universität Mainz, 1990.

[173] T. Kieck et al. "Highly efficient isotope separation and ion implantation of 163Ho for the ECHo project". In: *Nuclear Instruments and Methods in Physics Research Section A: Accelerators, Spectrometers, Detectors and Associated Equipment* 945 (2019), p. 162602. DOI: 10.1016/j.nima.2019.162602.

[174] D. Studer et al. "Laser spectroscopy of the 1001-nm ground-state transition in dysprosium". In: *Physical Review A* 98.4 (2018), p. 042504. DOI: 10.1103/PhysRevA.98.042504.

[175] D. Studer et al. "Atomic transitions and the first ionization potential of promethium determined by laser spectroscopy". In: *Physical Review A* 99.6 (2019), p. 062513. DOI: 10.1103/PhysRevA.99.062513.

[176] T. Kron et al. "Hyperfine structure study of ^{97,98,99}Tc in a new laser ion source for high-resolution laser spectroscopy". In: *Physical Review C* 102.3 (2020), p. 034307. DOI: 10.1103/PhysRevC.102.034307.

[177] D. Studer. "Probing atomic and nuclear structure properties of promethium by laser spectroscopy". Dissertation. Johannes Gutenberg-Universität Mainz, 2020. URL: https://openscience.ub.uni-mainz.de/handle/20.500.12030/4865.

[178] F. Weber. "Towards $Z = 100$ laser spectroscopy on atomic and nuclear structure in californium and einsteinium". Dissertation. Johannes Gutenberg-Universität Mainz, 2022.

[179] S. Nothhelfer et al. "Nuclear structure investigations of $^{253-255}$Es by laser spectroscopy". In: *Phys. Rev. C* 105.2 (2022), p. L021302. DOI: 10.1103/PhysRevC.105.L021302.

[180] R. Heinke et al. "High-resolution in-source laser spectroscopy in perpendicular geometry: Development and application of the PI-LIST". In: *Hyperfine Interactions* 238.6 (2017), pp. 1–9. DOI: 10.1007/s10751-016-1386-2.

[181] R. Horn. "Aufbau eines Systems gepulster, abstimmbarer Festkörperlaser zum Einsatz in der Resonanzsionisations-Massenspektrometrie". Dissertation. Johannes Gutenberg-Universität Mainz, 2003.

[182] V. Sonnenschein et al. "Characterization of a dual-etalon Ti: sapphire laser via resonance ionization spectroscopy of stable copper isotopes". In: *Hyperfine Interactions* 227 (2014), pp. 113–123. DOI: 10.1007/s10751-013-1000-9.

[183] V. Sonnenschein et al. "Characterization of a pulsed injection-locked Ti: sapphire laser and its application to high resolution resonance ionization spectroscopy of copper". In: *Laser Physics* 27.8 (2017), p. 085701. DOI: 10.1088/1555-6611/aa7834.

[184] V. Sonnenschein et al. "A direct diode pumped continuous-wave Ti: sapphire laser as seed of a pulsed amplifier for high-resolution resonance ionization spectroscopy". In: *Nuclear Instruments and Methods in Physics Research Section B: Beam Interactions with Materials and Atoms* 463 (2020), pp. 512–514. DOI: 10.1016/j.nimb.2019.03.017.

[185] M. Verlinde et al. "On the performance of wavelength meters: Part 1—consequences for medium-to-high-resolution laser spectroscopy". In: *Applied Physics B* 126.85 (2020), pp. 1–14. DOI: 10.1007/s00340-020-07425-4.

[186] W. Gins et al. "Analysis of counting data: Development of the SATLAS Python package". In: *Computer Physics Communications* 222 (2018), pp. 286–294. DOI: 10.1016/j.cpc.2017.09.012.

[187] A. Claessens. *Private communication.*

[188] A. Lopez-Martens et al. "Detailed spectroscopy of ^{249}Fm". In: *Phys. Rev. C* 74.4 (2006), p. 044303. DOI: 10.1103/PhysRevC.74.044303.

[189] T.M. Shneidman et al. "Possible alternative parity bands in the heaviest nuclei". In: *Physical Review C* 74.3 (2006), p. 034316. DOI: 10.1103/PhysRevC.74.034316.

[190] Z.-H. Zhang et al. "Systematic investigation of the rotational bands in nuclei with $Z \approx 100$ using a particle-number conserving method based on a cranked

shell model". In: *Physical Review C* 85.1 (2012), p. 014324. DOI: 10.1103/PhysRevC.85.014324.

[191] B. Cheal and K.T. Flanagan. "Progress in laser spectroscopy at radioactive ion beam facilities". In: *Journal of Physics G: Nuclear and Particle Physics* 37.11 (2010), p. 113101. DOI: 10.1088/0954-3899/37/11/113101.

[192] S. Ćwiok, S. Hofmann, and W. Nazarewicz. "Shell structure of the heaviest elements". In: *Nuclear Physics A* 573.3 (1994), pp. 356–394. DOI: 10.1016/0375-9474(94)90349-2.

[193] P.-G. Reinhard and W. Nazarewicz. *In preparation.*

[194] B. Bally and Michael Bender. "Projection on particle number and angular momentum: Example of triaxial Bogoliubov quasiparticle states". In: *Physical Review C* 103.2 (2021), p. 024315. DOI: 10.1103/PhysRevC.103.024315.

[195] P.T. Greenlees et al. "Shell-structure and pairing interaction in superheavy nuclei: Rotational properties of the Z=104 nucleus ^{256}Rf". In: *Physical Review Letters* 109.1 (2012), p. 012501. DOI: 10.1103/PhysRevLett.109.012501.

[196] M. Bender, W. Nazarewicz, and P.-G. Reinhard. "Shell stabilization of super- and hyperheavy nuclei without magic gaps". In: *Physics Letters B* 515.1-2 (2001), pp. 42–48. DOI: 10.1016/S0370-2693(01)00863-2.

[197] M.W. Johnson et al. "^{241}Am and ^{243}Am charge distributions from muonic x-ray spectroscopy and the quadrupole moment of the ^{240}Am fission isomer". In: *Physics Letters B* 161.1-3 (1985), pp. 75–78. DOI: 10.1016/0370-2693(85)90612-4.

[198] R. Ferrer et al. "Towards high-resolution laser ionization spectroscopy of the heaviest elements in supersonic gas jet expansion". In: *Nature Communications* 8.1 (2017), p. 14520. DOI: 10.1038/ncomms14520.

[199] E. Verstraelen et al. "Search for octupole-deformed actinium isotopes using resonance ionization spectroscopy". In: *Physical Review C* 100.4 (2019), p. 044321. DOI: 10.1103/PhysRevC.100.044321.

[200] A. Voss et al. "High-resolution laser spectroscopy of long-lived plutonium isotopes". In: *Physical Review A* 95.3 (2017), p. 032506. DOI: 10.1103/PhysRevA.95.032506.

[201] I. Angeli and K.P. Marinova. "Table of experimental nuclear ground state charge radii: An update". In: *Atomic Data and Nuclear Data Tables* 99.1 (2013), pp. 69–95. DOI: https://doi.org/10.1016/j.adt.2011.12.006.

[202] N.J. Stone. "Table of nuclear electric quadrupole moments". In: *Atomic Data and Nuclear Data Tables* 111-112 (2016), pp. 1–28. DOI: 10.1016/j.adt.2015.12.002.

[203] S. Rahaman et al. "Masses of neutron-rich Ni and Cu isotopes and the shell closure at Z= 28, N= 40". In: *The European Physical Journal A* 34 (2007), pp. 5–9. DOI: 10.1140/epja/i2007-10489-y.

[204] C. Guénaut et al. "High-precision mass measurements of nickel, copper, and gallium isotopes and the purported shell closure at $N = 40$". In: *Physical Review C* 75.4 (2007), p. 044303. DOI: 10.1103/PhysRevC.75.044303.

[205] Z. Patel et al. "Isomer decay spectroscopy of ^{164}Sm and ^{166}Gd: Midshell collectivity around $N = 100$". In: *Physical Review Letters* 113.26 (2014), p. 262502. DOI: 10.1103/PhysRevLett.113.262502.

[206] Y.-X. Liu et al. "Changes of deformed shell gaps at N 100 in light rare-earth, neutron-rich nuclei". In: *Journal of Physics G: Nuclear and Particle Physics* 47.5 (2020), p. 055108. DOI: 10.1088/1361-6471/ab752d.

[207] J. Wu et al. "94 β-Decay Half-Lives of Neutron-Rich $_{55}$Cs to $_{67}$Ho: Experimental Feedback and Evaluation of the r-Process Rare-Earth Peak Formation". In: *Physical Review Letters* 118 (7 2017), p. 072701. DOI: 10.1103/PhysRevLett.118.072701.

[208] M. Vilen et al. "Exploring the mass surface near the rare-earth abundance peak via precision mass measurements at JYFLTRAP". In: *Physical Review C* 101.3 (2020), p. 034312. DOI: 10.1103/PhysRevC.101.034312.

[209] D.C. Hoffman et al. "Spontaneous fission properties of 2.9-s ^{256}No". In: *Physical Review C* 41 (2 1990), pp. 631–639. DOI: 10.1103/PhysRevC.41.631.

[210] E.D. Donets, V.A. Shchegolets, and V.A. Ermakov. "Synthesis of the element 102 of mass number 256". In: *Soviet Atomic Energy* 16.3 (1964), pp. 233–245. DOI: 10.1007/BF01122965.

[211] I. Ahmad and J.L. Lerner. "Alpha-decay properties of ^{247}Cf, ^{248}Cf, ^{252}Fm and ^{254}Fm". In: *Nuclear Physics A* 413.3 (1984), pp. 423–431. DOI: 10.1016/0375-9474(84)90419-6.

[212] S. Raeder et al. "A gas-jet apparatus for high-resolution laser spectroscopy on the heaviest elements at SHIP". In: *Nuclear Instruments and Methods in Physics Research Section B: Beam Interactions with Materials and Atoms* 463 (2020), pp. 272–276. DOI: 10.1016/j.nimb.2019.05.016.

[213] D. Münzberg et al. "Resolution characterizations of JetRIS in Mainz using ^{164}Dy". In: *Atoms* 10.2 (2022), p. 57. DOI: 10.3390/atoms10020057.

[214] K. Eskola et al. "Studies of lawrencium isotopes with mass numbers 255 through 260". In: *Physical Review C* 4.2 (1971), pp. 632–642. DOI: 10.1103/PhysRevC.4.632.

[215] S. Antalic et al. "Decay studies of neutron-deficient lawrencium isotopes". In: *The European Physical Journal A* 38.2 (2008), pp. 219–226. DOI: 10.1140/epja/i2008-10665-7.

[216] J. Konki et al. "In-beam spectroscopic study of ^{244}Cf". In: *Physical Review C* 97.2 (2018), p. 024306. DOI: 10.1103/PhysRevC.97.024306.

[217] W. Reisdorf and M. Schädel. "How well do we understand the synthesis of heavy elements by heavy-ion induced fusion?" In: *Zeitschrift für Physik A Hadrons and Nuclei* 343.1 (1992), pp. 47–57. DOI: 10.1007/BF01291597.

[218] J. Khuyagbaatar et al. "The new isotope ^{236}Cm and new data on ^{233}Cm and ^{237,238,240}Cf". In: *The European Physical Journal A* 46.1 (2010), pp. 59–67. DOI: 10.1140/epja/i2010-11026-9.

[219] L. Xie et al. "Nuclear charge radii of $^{62-80}$Zn and their dependence on cross-shell proton excitations". In: *Physics Letters B* 797 (2019), p. 134805. DOI: 10.1016/j.physletb.2019.134805.

[220] S. Malbrunot-Ettenauer et al. "Nuclear charge radii of the nickel isotopes $^{58-68,70}$Ni". In: *Physical Review Letters* 128.2 (2022), p. 022502. DOI: 10.1103/PhysRevLett.128.022502.

[221] B. Cheal et al. "Collinear laser spectroscopy of neutron-rich cerium isotopes near the $N = 88$ shape transition". In: *Journal of Physics G: Nuclear and Particle Physics* 29.11 (2003), p. 2479. DOI: 10.1088/0954-3899/29/11/003.

Acknowledgements

Personal data

A. Appendix

A.1. Comparison of different applied silicon detectors

For the on-line experiments discussed in this work, different PIPS detectors featuring different performances, especially in terms of resolution, were used. The main details and specifications of the detector types are summarized in Tab. A.1.

Detector/ setup	Beamtime campaign	Active area [mm^2]	Al coating (Si equivalent) [µm]	Resolution on-line [keV]	Resolution off-line [keV]
Main detector	until 2020	600	0.25	61	247 with foil
(Rotatable) detector	2021	450	2.0	99	279
(Rotatable) detector	2021	450	none	43	/
Custom detector	since 2022	600	0.125	46	158

Table A.1.: Summary of PIPS detectors applied in the RADRIS setup in beamtime campaigns described in this work.

The different PIPS detector types were characterized in a separate vacuum chamber using an enclosed triple-alpha source. This type of source contained alpha lines of the nuclides ^{239}Pu, ^{241}Pu, and ^{244}Cm. Alpha-energy spectra were recorded under similar experimental conditions for every detector test in a vacuum environment of about 10^{-2} mbar and a distance of the source from the detector of few tens of cm. In Fig. A.1, the spectra of the various detector types are shown with the respective achieved resolution for alpha events at energies of about 5.2 MeV.

For a characterization in on-line conditions in the RADRIS setup, alpha-energy spectra, after a direct transport of ^{254}No mother nuclei along with their subsequent daughter nulides ^{250}Fm and ^{246}Cf, were recorded in the beamtime campaigns in 2020, 2021 and 2022, as shown in the spectra in Fig. A.2. It is worth noting, that the resolution is affected not only by the detector type itself, but the overall management of the detector noise, which is more challenging under on-line conditions. In the comparison of the three experimental campaigns, the best achievable resolution was seen with the newly developed movable double-detector setup equipped with the custom-coated PIPS detectors.

The tested detector types can be separated by the beamtime campaign and the RADRIS setup they were used in. A larger PIPS detector was previously applied in the original setup, as shown in Fig. 4.8. In this status of the setup, the detector

was utilized along with an additional collection foil in front, as described in Sec. 4.3.1, which negatively influences the resolution for detected alpha particles. This detector was used for the measurements on ^{248,250}Fm in this work. For the measurements on ^{249}Fm during the beamtime campaign in 2021, a smaller and light-insensitive PIPS detector was applied. A coating of 2 µm equivalent silicon made the collection foil obsolete, however at the expense of a worse resolution of about 279 keV for alpha particles emitted on the detector surface. In the rotatable-detector setup in Sec. 5.3, the light-insensitive detectors were replaced by similar but uncoated detectors without the thick aluminum layer, otherwise featuring similar specifications. This type of detector was used for measurements on the long-lived ^{254}Fm. However, data on a direct transport of ^{254}No was not available for a comparison under on-line conditions. In the movable-detector setup, as used in the campaign in 2022, a custom-made PIPS detector with 125 nm aluminum coating and a larger active surface area of 600 mm^2 was employed, yielding close to the best achievable resolution in on-line application among the tested detectors with 158 keV.

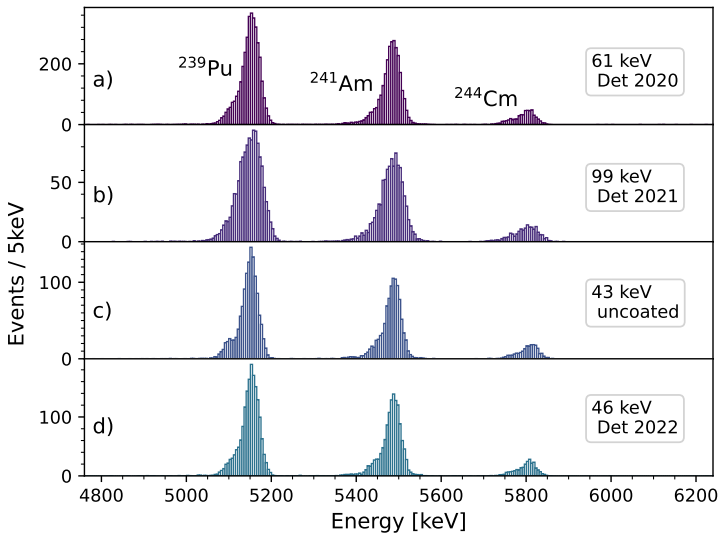

Figure A.1.: Comparison of different PIPS detectors using a (closed) triple-alpha source at distance from the detectors. a) The spectrum of the previous 600 mm^2 detector with thin coating. b) Resolution of a 450 mm^2 PIPS detector with thick coating for light-insensitivity, c) spectrum of a similar but uncoated 450 mm^2 PIPS detector. d) Performance of a custom-made 600 mm^2 detector with thin aluminum coating.

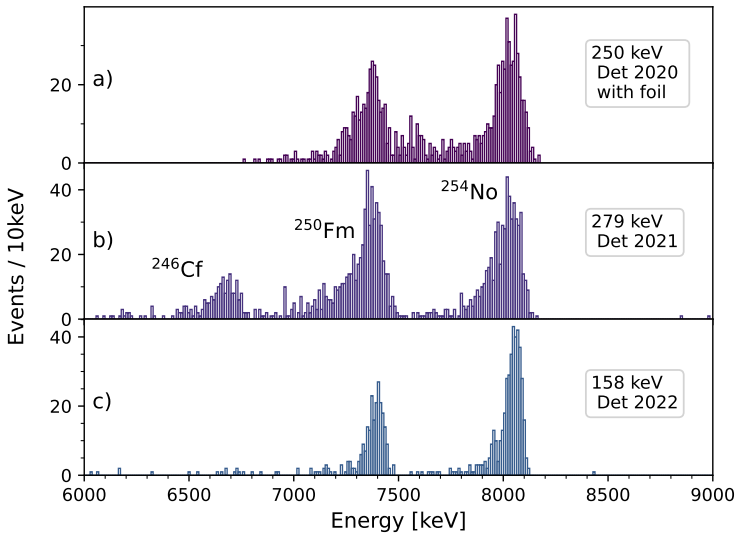

Figure A.2.: Comparison of different applied PIPS detectors in on-line conditions for detection of alpha-signals after direct transport of ^{254}No. a) Spectrum of the 600 mm^2 detector with thin coating in connection with the collection foil in front as applied previous to recent RADRIS developments. b) Resolution of a 450 mm^2 detector with thick coating for light-insensitivity and c) the spectrum of a custom 600 mm^2 detector with thin aluminum coating.

A.2. Optimization of the new RADRIS transport electrode structure

Ion trajectories for ions from resonance ionization produced in the vicinity of the filament were simulated for the new RADRIS setup with the upgraded transport electrode structure developed in this work (see Sec. 5.1). In the simulation framework with SIMION 8.1 [168], singly charged positive ions of mass 254 with thermal velocities were assumed to move at room temperature in an argon buffer-gas environment at 90 mbar. The trajectories of respective ions were modeled, taking into account the buffer gas collisions and the effect of the guiding electric fields of the transport electrodes. As a starting point, regarding a rather extreme scenario, a sphere of 2 cm radius centered around the filament was considered, with the created ions uniformly distributed within it. The program simulated flight paths of 100 ions at a time for various potential settings, the endpoints of the trajectories among other parameters were recorded. Different settings for the first and last electrode of both, the transport electrodes (E1 and E6), as well as the funnel electrodes (funnel entrance/exit) were tested to simulate the effect of different linear voltage gradients in the respective structures for the ion transport. An example of a simulation result is shown in Fig. A.3 for varying funnel gradients and fixed potential settings for the other transport electrodes, filament, lower electrode and cross piece. The number of ions reaching the detector in dependence of

the applied funnel potentials setting is visualized through the color-coding.

Since these simulations were solely conducted to infer a reference point for potential settings, only a limited number of 100 ion trajectories was simulated per setting to keep the required simulation time short. However, the results, as in the example shown in Fig. A.3, indicate a wide range of potential gradients for which more than 90 % of the ions are simulated to reach the detector. This basic simulation framework provided an initial understanding of the effect of various potential gradients on the transport efficiency. The results served as a starting point for further off-line commissioning tests to identify an optimal potential arrangement.

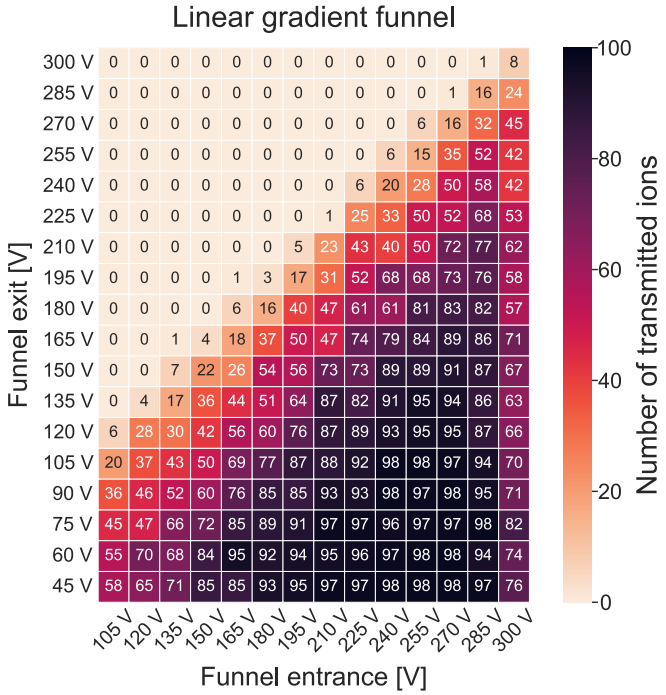

Figure A.3.: Results on the ion-trajectory simulations on the transmission through the DC-funnel structure for different voltage settings. The transport electrodes E1 - E6 were kept at a constant potential and the funnel entrance and exit electrodes varied (hence the voltage gradient changed). The number of ions reaching the detector is shown via a color coding and transmission numbers in the field belonging to a specific setting.

The setup with the re-designed electrode structure was tested for the transport of ions created near the filament to the detector. The applied potential gradients were optimized off-line, utilizing a ^{225}Ac recoil source mounted on top of the entrance window flange, facing the filament. RADRIS cycles were simulated by applying an attractive potential to the filament, as done during the on-line collection mode, for thermalized recoil nuclei originating from the source. After accumulation for 100 s, the main collection detector was moved to the on-axis position to receive ions. The filament potential was switched to a high, repellent potential for transport mode before a heat pulse of

about 1450 °C was applied. This temperature was sufficient to generate surface ions of the first decay daughter in the chain, ^{221}Fr, with a half life of 4.9 min. The created ions were transported to the detector where the rate of alpha events from decay daughters and granddaughters were recorded. After 2 s, the filament potential was reset for recoil nuclei collection and the cycle was repeated. To ensure sufficient statistics, a total of 9 cycles were repeated, lasting about 1050 s in total, followed by a 1200 s decay time before testing the next potential setting.

In the optimization procedure, different electrode combinations were varied to investigate their respective influence on the ion transport. During all tests, the cross piece was kept at a constant potential of 1025 V. In the measurement routine, potentials were varied for the filament and the lower electrode, the six transport electrodes from E1 to E6, and the seven funnel electrodes with the entrance and exit funnel electrode. For both, the transport electrodes and the funnel electrodes, respectively, a linear gradient is applied. Usually, only the two outermost electrode potentials in the structures defining the gradient are named in the following.

In a first step, the potential difference between the filament and the lower electrode was optimized. Various potential combinations were applied, close to the optimum simulation results, and the rate of arriving ions at the detector in terms of their alpha-decay rate was recorded. The other electrodes were maintained at a constant gradient towards ground potential at the detector. In a next step, the filament and lower electrode were adjusted to the optimal settings found, and the gradient towards the first transport electrode E1 and subsequent electrodes varied. Finally, different funnel gradients were tested for a varying potential at the last transport electrode E6 and a fixed potential for E1, therefore a varying transport gradient. In Fig. A.4, exemplary results from the off-line tests are displayed, showing the number of registered recoil ions in dependence of the funnel potentials for two different E6 potentials. The results in the left figure show, that negative gradient between E6 and the funnel entrance entirely prevents the ions from reaching the detector. Similarly, a more shallow gradient between them, and likewise a flatter gradient in the funnel structure itself, is less favorable for the transmission.

During the on-line commissioning of the upgraded RADRIS setup, four different settings close to the found off-line optimization results were tested. The rate of detected ^{155}Yb ions from laser resonance ionization generated in the applied on-line RADRIS cycle was recorded for a number of cycles. The tested settings and detected count rates normalized to the beam charge integral are given in Tab. A.2. Within the uncertainties of the short test measurements and therefore low counting statistics, none of the settings stood out but a similar transport efficiency was shown for all. As setting 1 showed an about 20 % increased detection rate to the other tested settings, it was determined as the optimal setting and applied for the successive on-line measurements during the beamtime campaign in 2022. This includes the measurements on ^{245,246}Fm and the proof-of-principle measurements on ^{251}No discussed in this work.

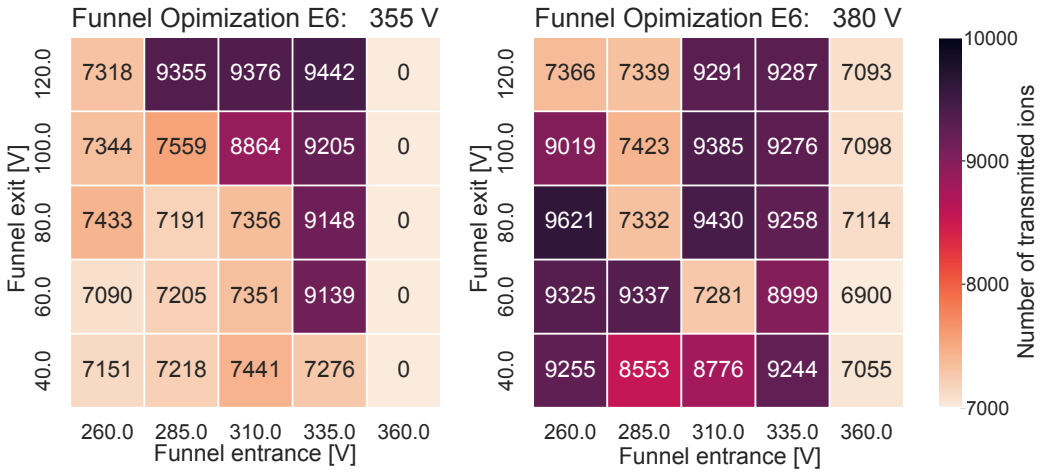

Figure A.4.: Results from off-line funnel optimization measurements with an ^{225}Ac-recoil source in dependence of the applied funnel potentials. The filament, lower electrode, cross piece and first transport electrode E1 were kept at a fixed potential. The left matrix shows the number of detected ions for a potential of 355 V on the last transport electrode E6 and hence, a steeper transport electrode gradient than in the right matrix for a potential of 380 V. More details in the text.

Electrode	Setting 1 [V]	Setting 2 [V]	Setting 3 [V]	Setting 4 [V]
Filament	1050	1050	900	1050
Cross Piece	1025	1025	1025	1025
Lower electrode	1015	1015	1015	1015
Electrode 1	925	925	900	950
Electrode 2	818	823	803	833
Electrode 3	711	721	706	716
Electrode 4	604	619	609	599
Electrode 5	497	517	512	482
Electrode 6	390	415	415	365
Funnel entrance	365	345	345	345
Funnel exit	130	105	105	130
Norm. counts / mC	1774(158)	1450(143)	1532(148)	1433(143)

Table A.2.: Potentials tested on-line in the upgraded RADRIS setup for transport of ^{155}Yb ions. Several RADRIS cycles were performed and the resonantly ionized ions guided to the detector applying the various settings. The rates of detected ions normalized to the beam charge integral are included for an evaluation of the optimal transport setting.

A.3. Absolute centroid wavenumbers of observed transition resonances in fermium

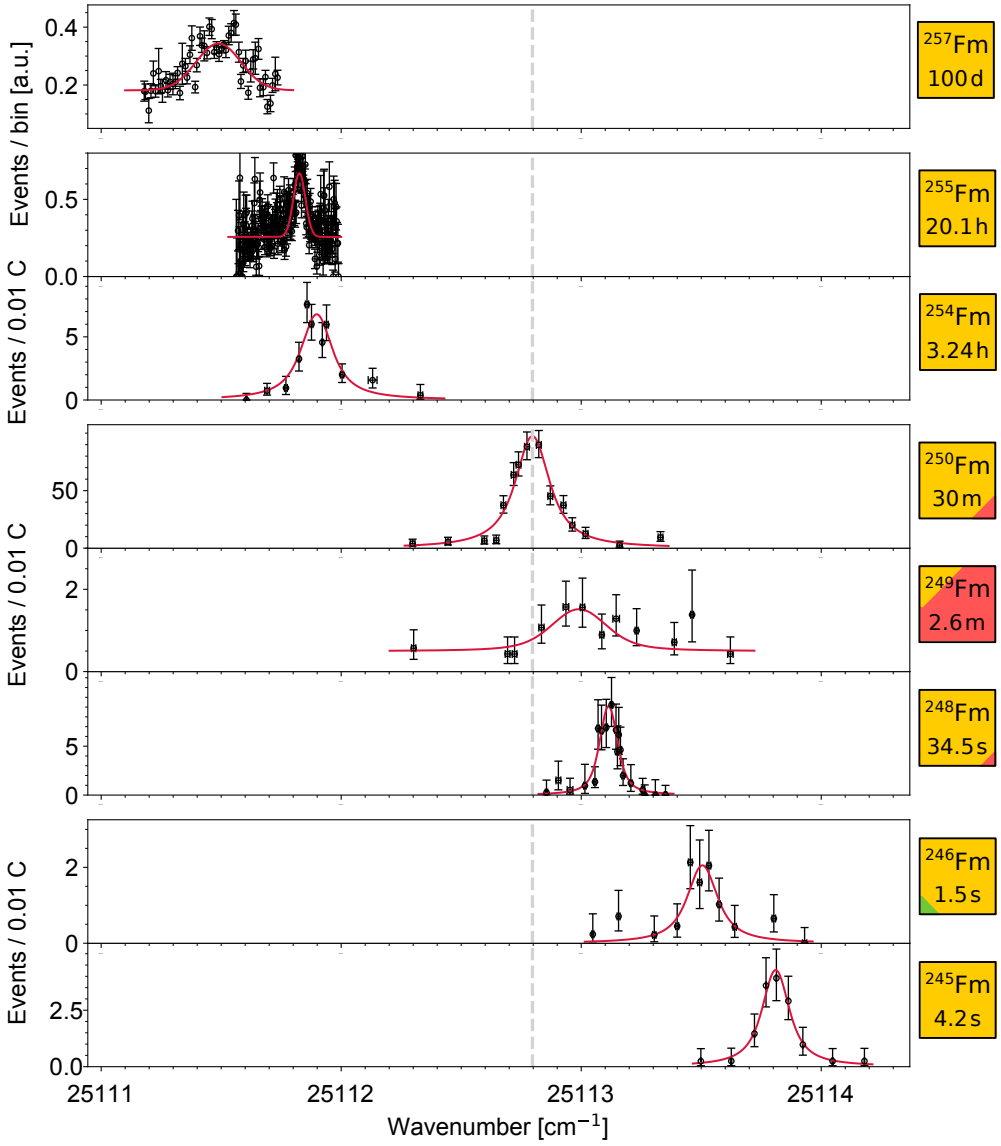

Figure A.5.: Overview over observed RIS resonances in eight fermium isotopes with absolute transition wavenumbers. From the extracted centroid wavenumbers of the resonances isotope shifts relative to reference isotope ^{250}Fm were determined. Results from off-line and on-line laser spectroscopy experiments were combined to see the full overview of the measurements in fermium. The respective best-fits to the data are added to the experimental data.

A.4. Spherical droplet model

The semi-empirical Droplet Model (DM) was introduced in Sec. 2.1.4 as an extension of the heuristic Liquid Drop Model (LDM) which holds a macroscopic description for the prediction of several nuclear properties, such as the nuclear mass, binding energy and charge radius. The quantity $R = R_0 \cdot A^{1/3}(1 + \bar{\epsilon})$ as described in chapter 2, Sec. 2.1.4 considers the radius given by the LDM with a correction term. In all contributions, deformation is neglected (see Ref. [31], all orders of $\alpha_i = 0$).

The absolute radius of the DM with the correction term for a spherical nucleus depends on the constants given with the expressions

$$\bar{\epsilon} = \frac{1}{K}(-2a_s A^{-1/3} + L\bar{\delta}^2 + \frac{3e^2}{5R_0}Z^2A^{-4/3}), \tag{A.1}$$

$$\bar{\delta} = \frac{I + \frac{3}{16}(c_1/Q)ZA^{-2/3}}{1 + \frac{9}{4}(J/Q)A^{-1/3}}, \tag{A.2}$$

$$I = \frac{N - Z}{A}. \tag{A.3}$$

Surface energy a_s	Density symmetry L	Surface stiffness Q	Symmetry energy J	Compressibility K	Nuclear radius constant R_0
23 MeV	−35 MeV	45 MeV	29.5 eV	240 MeV	1.18 fm

Table A.3.: Parameter set used for droplet model calculations compared to experimental data in this work. These values were taken from the second set developed in Ref. [58].

The mean-square charge radius within this model can be calculated with

$$\langle r^2 \rangle = \langle r^2 \rangle_u + \langle r^2 \rangle_r + \langle r^2 \rangle_d, \tag{A.4}$$

where the individual contributions are defined as $\langle r^2 \rangle_u = \frac{3}{5}R^2$ for the uniform distribution, $\langle r^2 \rangle_r = \frac{12}{175}R^2C'$ for the redistribution of nucleons with $C' \approx 0.0156ZA^{-1/3}$ and $\langle r^2 \rangle_d = 3b^2$ for the diffuseness of the distribution. The latter is independent of the shape and considered constant with $b = 1.02$ fm [58].

A.5. Mean-square charge radius evolution at lighter deformed shell gaps

In Sec. 8.3, the influence of known deformed shell gaps in other regions of the nuclear chart were discussed, such as at $N = 40$ and $N = 98$. Previous laser spectroscopy studies in the former region revealed a local minimum in the residual mean-square charge radius evolution relative to predictions from a spherical droplet model. This effect of the deformed shell gap is shown in Fig. A.6. To better identify the impact of the shell gap on the nuclear size evolution, the isotopes with even and odd neutron numbers are visually separated in respective chains by connection via either solid or dashed lines and different data markers. In this way, an effect of the shell gap becomes more apparent as it is less evident under the present odd-even staggering.

The local minimum in the nickel chain at magic ^{68}Ni reveals the impact of the shell gap on its charge size, while a similar effect observed in the copper chain at ^{69}Cu is already weakened. With one proton more in the zinc chain, the shell effect in the mean-square charge radii disappears, showcasing the localization of this effect on a small region around ^{68}Ni [19].

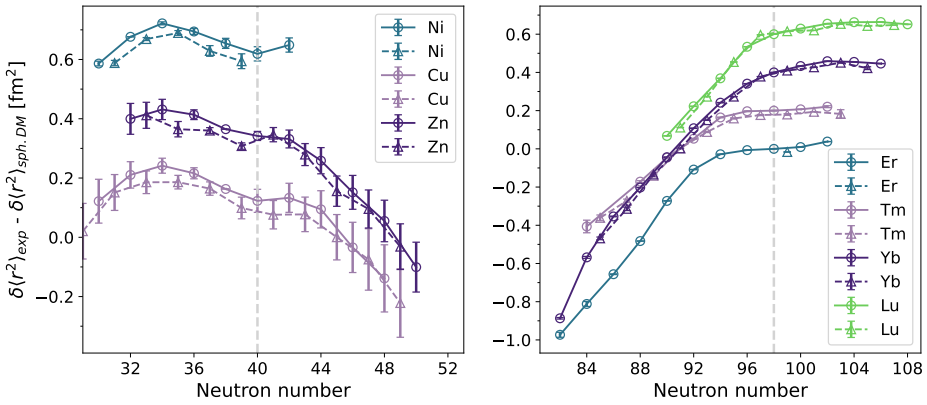

Figure A.6.: Residual changes in mean-square charge radii relative to the trend in spherical droplet model predictions of isotopic chains of lighter deformed elements crossing shell gaps at a) $N = 40$ and b) $N = 98$. As a reference, predictions from a spherical DM were subtracted from respective changes in mean-square charge radii. Data points of isotopes with even neutron numbers are marked with circles and connected by solid lines, triangles with dashed lines indicate data for odd neutron number isotopes. The data is taken from literature in Refs. [9, 123, 201, 219, 220].

In the data available for the rare-earth elements around $N = 98$, no such effect was found but instead a constant increase close to the trend of droplet model predictions. The trend of increasingly smaller mean-square charge radii relative to the model as neutron numbers decrease can be explained by a nearby shape transition occurring at $N = 88$ [221]. It is therefore not related to an effect of the deformed shell gap itself.